

## Copyright Warning & Restrictions

The copyright law of the United States (Title 17, United States Code) governs the making of photocopies or other reproductions of copyrighted material.

Under certain conditions specified in the law, libraries and archives are authorized to furnish a photocopy or other reproduction. One of these specified conditions is that the photocopy or reproduction is not to be “used for any purpose other than private study, scholarship, or research.” If a user makes a request for, or later uses, a photocopy or reproduction for purposes in excess of “fair use” that user may be liable for copyright infringement,

This institution reserves the right to refuse to accept a copying order if, in its judgment, fulfillment of the order would involve violation of copyright law.

**Please Note: The author retains the copyright while the New Jersey Institute of Technology reserves the right to distribute this thesis or dissertation**

Printing note: If you do not wish to print this page, then select “Pages from: first page # to: last page #” on the print dialog screen



The Van Houten library has removed some of the personal information and all signatures from the approval page and biographical sketches of theses and dissertations in order to protect the identity of NJIT graduates and faculty.

## ABSTRACT

# THE CONTROL OF FREQUENCY OF A CONDITIONAL OSCILLATOR SIMULTANEOUSLY SUBJECTED TO MULTIPLE OSCILLATORY INPUTS

by

Christina L. Ambrosio

A conditional oscillator is one that requires input to oscillate. An example of such is the gastric mill network of the stomatogastric ganglion of the crab *Cancer borealis* which requires modulatory input from outside the stomatogastric ganglion and fast input from the pyloric network of the animal in order to become active. This dissertation studies how the frequency of the gastric mill network is determined when it is simultaneously subjected to two different rhythmic inputs whose timing may be mismatched. We derive a mathematical model of the gastric mill network and deduce that the difference in timing between the pyloric and modulatory inputs is crucial in determining what effect it will have on the frequency of the gastric mill network. Over a certain range of the time mismatch, the pyloric input plays no role in determining the network frequency, while in another range of the time mismatch, both inputs work together to determine the frequency. The existence and stability of periodic solutions to the modeling set of equations are obtained analytically using geometric singular perturbation theory and an analytic approximation of the frequency is obtained. The results are validated through numerical simulations of the model and are shown to extend to a detailed Hodgkin-Huxley type compartmental model of the gastric mill network. Comparisons to experiments are also presented.

**THE CONTROL OF FREQUENCY OF A CONDITIONAL  
OSCILLATOR SIMULTANEOUSLY SUBJECTED TO MULTIPLE  
OSCILLATORY INPUTS**

by  
**Christina L. Ambrosio**

**A Dissertation  
Submitted to the Faculty of  
New Jersey Institute of Technology and  
Rutgers, The State University of New Jersey – Newark  
in Partial Fulfillment of the Requirements for the Degree of  
Doctor of Philosophy in Mathematical Sciences**

**Department of Mathematical Sciences, NJIT  
Department of Mathematics and Computer Science, Rutgers-Newark**

**May 2005**

Copyright © 2005 by Christina L. Ambrosio

ALL RIGHTS RESERVED

**APPROVAL PAGE**

**THE CONTROL OF FREQUENCY OF A CONDITIONAL  
OSCILLATOR SIMULTANEOUSLY SUBJECTED TO MULTIPLE  
OSCILLATORY INPUTS**

**Christina L. Ambrosio**

Amitabha Bose, Dissertation Advisor  
Associate Professor, Department of Mathematical Sciences, NJIT  
Date

~~Farzan Nadim~~, Committee Member  
Associate Professor, Department of Mathematical Sciences, NJIT and  
Department of Biological Sciences, Rutgers-Newark  
Date

Robert Miura, Committee Member  
Professor, Department of Mathematical Sciences, NJIT  
Date

David Stickler, Committee Member  
Associate Professor, Department of Mathematical Sciences, NJIT  
Date

~~G. Mill Jonakait~~, Committee Member  
Distinguished Professor, Division of Biological Sciences, NJIT  
Date

## BIOGRAPHICAL SKETCH

**Author:** Christina L. Ambrosio  
**Degree:** Doctor of Philosophy  
**Date:** May 2005

### Undergraduate and Graduate Education:

- Doctor of Philosophy in Mathematical Sciences,  
New Jersey Institute of Technology, Newark, NJ, 2005
- Master of Science in Applied Mathematics,  
New Jersey Institute of Technology, Newark, NJ, 2001
- Bachelor of Arts in Mathematics,  
The College of New Jersey, Trenton, NJ, 1999

**Major:** Mathematical Sciences

### Presentations and Publications:

- C. Ambrosio, A. Bose, and F. Nadim, “The effect of modulatory neuronal input on gastric mill frequency,” *Neurocomputing*, in press.
- C. Ambrosio, F. Nadim, and A. Bose, “The effects of varying the timing of inputs on a conditional oscillator,” *submitted to SIAM Journal on Applied Dynamical Systems*.
- C. Ambrosio, “The effect of modulatory neuronal input on gastric mill frequency,” *Mathematical Biology Seminar*, Department of Mathematical Sciences, NJIT, April 27, 2004.
- C. Ambrosio, F. Nadim, and A. Bose “Distinct synaptic pathways control the frequency of a rhythmic network,” *SIAM Conference on Applications of Dynamical Systems*, Snowbird, UT, May 27-31, 2002.
- C. Ambrosio, A. Bose, F. Nadim “The effect of modulatory neuronal input on gastric mill frequency,” *Thirteenth Annual Computational Neuroscience Meeting*, Baltimore, MD, July 18-22, 2004.

Some people succeed because they are destined to but  
most people succeed because they are determined to.

-Author unknown

## ACKNOWLEDGMENT

I would like to take this opportunity to thank all of the many people who have been so helpful throughout my career at NJIT. First and foremost, I would like to thank my advisor, Dr. Amitabha Bose for his guidance, patience, and encouragement throughout this process. I truly could not have asked for a better advisor. I would also like to thank Dr. Farzan Nadim for helping me to find such an interesting research topic and for explaining much of the biology to me. Many thanks to Dr. David Stickler, Dr. Robert Miura, Dr. Mill Jonakait, and Dr. Jorge Golowasch for taking the time to read and discuss my thesis with me and for their support. I would also like to thank Bob LoMauro for letting me watch him do experiments on the STG.

Many other members of the Department of Mathematical Sciences at NJIT have been of great help to me along the way. In particular, I would like to thank Dr. Daljit Ahluwalia for his encouragement and for his dedication to the graduate students of the Mathematics department. Thanks to Mrs. Padma Gulati for being so excited for me throughout all of my accomplishments and thanks to the staff of the mathematics department for all of their help.

I would like to thank all of the graduate students in the Department of Mathematical Sciences whom I have gotten to know over the last few years. In particular, I would like to say an extra thank you to Arnaud Goulet for taking the time to have many discussions with me on dynamical systems, for teaching me xfig, and for helping me format my thesis. I would also like to acknowledge Muhammad Hameed, Nick Kintos, Tsezar Seman, Yuriy Mileyko, and Jyoti Champanerkar whom have helped me in some way or another.

Finally, I would like to thank my family without whom this dissertation would not have been possible. I would like to thank my parents Lorraine and Mario Ambrosio for working so hard so that I could continue to go to school. I also want to thank my

mom for always telling me that I could be whatever I want to be and for pushing me to do my best. I would like to thank my brother Tom Ambrosio for his encouragement. A special thank you and I love you goes to my little angel Joey for making me laugh everyday for the past 16 years and for always being there when I needed a study break. I would like to thank my soon-to-be husband Matthew Mouser for his never ending faith in me and interest in my research. Thank you for always being so proud of me. Last but not least, I would like to thank God for all of the many blessings in my life and for giving me the opportunity and ability to achieve my dreams.

## TABLE OF CONTENTS

Chapter	Page
1 INTRODUCTION . . . . .	1
2 OVERVIEW . . . . .	18
3 MODELING THE STOMATOGASTRIC GANGLION . . . . .	21
3.1 Modeling Action Potentials . . . . .	21
3.2 Modeling Synapses . . . . .	26
3.3 The Gastric Mill Rhythm and The Full Model . . . . .	29
3.4 The Expanded Reduced Model . . . . .	33
3.5 Geometric Singular Perturbation Theory and Phase Plane Analysis . . . . .	40
4 EXISTENCE AND STABILITY OF PERIODIC SOLUTIONS AND THE CALCULATION OF FREQUENCY . . . . .	52
4.1 Case 1: Tonic <i>MCN1</i> Excitation without <i>AB</i> input to <i>Int1</i> . . . . .	53
4.2 Case 2: Tonic <i>MCN1</i> Excitation with <i>AB</i> Input to <i>Int1</i> . . . . .	56
4.2.1 Possible Solution Trajectories for Case 2 . . . . .	57
4.2.2 Construction of Periodic Solution for Case 2 . . . . .	60
4.3 Case 3: Rhythmic <i>MCN1</i> Excitation with <i>AB</i> Input to <i>Int1</i> Absent . . . . .	67
4.3.1 Possible Solution Trajectories for Case 3 . . . . .	67
4.3.2 Construction of Periodic Solution for Case 3 . . . . .	69
4.4 Case 4: Rhythmic <i>MCN1</i> Excitation with <i>AB</i> Input to <i>Int1</i> Present . . . . .	74
4.4.1 Possible Solution Trajectories for Case 4 . . . . .	74
4.4.2 Construction of Periodic Solution for Case 4 . . . . .	75
4.5 Determining the Frequency of Solutions . . . . .	77
4.6 Comparison Between Simulations of The Expanded, Reduced Model and Experimental Results . . . . .	81
5 A MORE BIOLOGICALLY ACCURATE REPRESENTATION OF THE REDUCED MODEL AND THE FULL MODEL . . . . .	90
5.1 Voltage Dependent <i>MCN1</i> to <i>LG</i> Synapse in The Expanded, Reduced Model . . . . .	90

**TABLE OF CONTENTS**  
(Continued)

Chapter	Page
5.2 Electrical Coupling Added to the Expanded, Reduced Model . . . . .	93
5.3 Simulations of the Expanded, Full Model Using Network . . . . .	99
5.3.1 Rhythmic <i>MCN1</i> Excitation in the Expanded, Full Model . .	99
5.3.2 Electrical Coupling in the Expanded, Full Model . . . . .	102
5.3.3 Comparison Between Simulations of the Expanded, Full Model and Experimental Results . . . . .	104
6 CONCLUSION . . . . .	107
6.1 Summary of Results and Discussion . . . . .	107
6.2 Future Work . . . . .	113
APPENDIX A PARAMETERS OF FULL MODEL . . . . .	116
APPENDIX B NON-DIMENSIONALIZATION OF THE SYSTEM OF EQUATIONS . . . . .	118
APPENDIX C CALCULATION OF THE STABILITY OF FIXED POINTS	122
APPENDIX D CALCULATION OF $S_L^{ON}$ , $S_L^{OFF}$ , $S_R^{ON}$ , AND $S_R^{OFF}$ . . . . .	125
REFERENCES . . . . .	129

## LIST OF TABLES

<b>Table</b>	<b>Page</b>
4.1 Parameters of The Expanded, Reduced Model . . . . .	80
4.2 Comparison of The Frequency Calculated Through XPP Simulations and The Analytic Formula . . . . .	80
A.1 Parameters of The Ionic Currents for The Expanded Full Model . . . . .	116
A.2 Parameters of The Synaptic Currents for The Expanded Full Model . . . . .	117

## LIST OF FIGURES

Figure	Page
1.1 A spinal motor neuron with a soma, axon, and dendrites [36]. . . . .	3
1.2 Electrical signals in the nervous system are created by the movement of ions through channels in the cell membrane. . . . .	4
1.3 Action potentials. . . . .	5
1.4 Structure of chemical and electrical synapses. . . . .	6
1.5 Schematic diagram of the four ganglion of the stomatogastric nervous system and the nerves that connect them. . . . .	8
1.6 Diagram of the stomach of crustaceans . . . . .	8
1.7 Schematic diagram of the neurons contained in the gastric mill (blue) and the pylorus (red) along with their synaptic connections. The neurons <i>LPG</i> , <i>MG</i> , and <i>Int1</i> lie in the gastric mill but are active in pyloric time when there is no gastric mill rhythm. <i>LG</i> , <i>GM</i> , <i>DG</i> , and <i>AM</i> are gastric mill neurons and <i>AB</i> , <i>PD</i> , <i>LP</i> , <i>IC</i> , <i>PY</i> , and <i>VD</i> are pyloric neurons. . . . .	10
1.8 Voltage traces of three neurons lying in the STG. . . . .	12
1.9 Circuitry for Cases 1-4. . . . .	15
3.1 Schematic diagram of the full model of the <i>AB</i> and <i>MCN1</i> elicited gastric mill rhythm. . . . .	30
3.2 Voltage traces of <i>LG</i> (lower trace) and <i>Int1</i> (upper trace) computed from simulation of the full model when the <i>AB</i> inputs to <i>MCN1</i> and to <i>Int1</i> are not present. . . . .	33
3.3 Schematic representation of the expanded, reduced model of the <i>MCN1</i> and <i>AB</i> elicited gastric mill circuit. . . . .	35
3.4 The synaptic variables $s_{AB \rightarrow I}(t)$ and $s_{AB \rightarrow M}(t)$ . Note that $s_{AB \rightarrow M}(t)$ decays with time constant $\tau_{AB}$ . . . . .	35
3.5 Voltage traces of <i>LG</i> and <i>Int1</i> computed from simulation of the expanded, reduced model when the <i>AB</i> inputs to <i>MCN1</i> and <i>LG</i> are not present. . . . .	40
3.6 The $V_L$ and $V_I$ nullclines plotted in phase space for different values of $s(t)$ and $s_{AB \rightarrow I}$ . . . . .	44
3.7 The change in the position of the $V_I$ nullcline due to $s_{AB \rightarrow I}$ . . . . .	44

**LIST OF FIGURES**  
(Continued)

Figure	Page
3.8 The location of the fixed point in phase space for different values of $s(t)$ .	46
3.9 Position of the $V_L$ and $V_I$ nullclines for $(s, s_{AB \rightarrow I}) = (s_R^{on}, 1), (s_R^{off}, 0), (s_L^{on}, 1),$ and $(s_L^{off}, 0)$ .	47
3.10 $s(t)$ versus $t$ for tonic and rhythmic excitation.	48
3.11 The solution trajectory when $s_{AB \rightarrow I}(t) = 0$ .	49
3.12 Possible ways fixed points can be lost for <i>MCN1</i> rhythmic.	51
4.1 The nullclines, solution trajectory, and voltage traces in Case 1.	55
4.2 The location of the stable fixed point on the left branches of the nullclines as $s(t)$ increases in Case 2.	56
4.3 For <i>MCN1</i> tonic and the <i>AB</i> input to <i>Int1</i> present, fixed points can be lost in multiple ways.	59
4.4 In Case 2, a periodic orbit obeying property A.	61
4.5 The interval $I$ used to define the Poincare map in Case 2.	63
4.6 Case 3 solution trajectory and nullclines obeying Property B.	70
4.7 The interval $I$ used to define the Poincare map in Case 3.	71
4.8 Experimental findings of the gastric mill rhythm cycle frequency for Cases 1-4.	82
4.9 The period of the gastric mill cycle is plotted for different delays, $m$ , in Case 4.	84
4.10 Calculations of the gastric mill rhythm cycle frequency for Cases 1-4 using the expanded, reduced model.	85
4.11 Comparisons between the duty cycle of <i>LG</i> from experimental work and from the expanded, reduced model.	86
4.12 Comparisons between the frequency of the gastric mill rhythm when <i>MCN1</i> activity is pyloric timed and when it is free-running with respect to <i>AB</i> activity.	87
4.13 Comparisons between the <i>LG</i> duty cycle when <i>MCN1</i> activity is pyloric timed and when it is free-running with respect to <i>AB</i> activity.	87
4.14 Latency calculation from experiments when <i>MCN1</i> activity is free-running and when it is pyloric timed.	88

**LIST OF FIGURES**  
(Continued)

<b>Figure</b>	<b>Page</b>
4.15 Voltage trace of <i>LG</i> when the rhythmic <i>MCN1</i> activity is free-running in the expanded, reduced model. . . . .	89
5.1 The $V_L$ and $V_I$ nullclines are plotted in the absence and presence of electrical coupling between <i>MCN1</i> and <i>LG</i> for $V_M = V_M^*$ and $V_M = E_{leak,M}$ . . . . .	95
5.2 The $V_L$ and $V_I$ nullclines are plotted in the absence of electrical coupling and presence of electrical coupling in Case 3. . . . .	97
5.3 The period of the gastric mill cycle calculated from the expanded, full model is plotted for different delays, $m$ , in Case 4 . . . . .	101
5.4 Voltage traces of <i>LG</i> and <i>Int1</i> in Cases 3 (left) and 4 (right) for $m = 180$ . For this delay, the period of the gastric mill rhythm is equal in Cases 3 and 4. . . . .	101
5.5 The <i>LG</i> duty cycle is shown for Cases 1-4 when the conductance of the electrical coupling in the expanded, full model is constant and when the conductance is voltage dependent. . . . .	103
5.6 Voltage traces of <i>LG</i> for two different strengths of $\bar{g}_c$ obtained through simulations of Network. . . . .	104
5.7 The gastric mill rhythm cycle frequency for Cases 1-4 determined through simulations of the expanded, full model. . . . .	105
5.8 The <i>LG</i> neuron duty cycle for Cases 1-4 determined through experiments and through simulations of the expanded, full model. . . . .	106
5.9 Voltage trace of <i>LG</i> when the rhythmic <i>MCN1</i> activity is free-running in the expanded, full model. . . . .	106

## CHAPTER 1

### INTRODUCTION

As conscious animals, the desire to understand the means by which all of our behaviors are controlled is an increasing area of interest. The central nervous system of humans which consists of the brain and spinal cord is responsible for regulating the most fundamental behaviors such as the beating of the heart, processing of visual information, and coordination of the movement of muscles involved in such things as chewing and walking. The central nervous system is also responsible for more abstract processes such as learning and the expression of emotions.

Much work done since the start of the 19th century by numerous scientists has opened the doorway to our understanding of the many functions of the human brain. Camillo Golgi and Ramon y Cajal led the way in developing new techniques to view single neurons of the brain. Cajal and Karl Wernicke [36, 52] were among the group of experimentalists who discovered that different regions of the brain are responsible for different functions. Scientists such as Emil DuBois-Reymond and Hermann von Helmholtz [36, 52] revealed one of the most fundamental and significant properties of neurons: the means by which neurons convey information from one cell to another is through electrical signaling. In the early 1950's, Alan Lloyd Hodgkin and Andrew Fielding Huxley [29, 30, 31, 32] reached another milestone in the understanding of the function of the brain when they observed experimentally and mathematically modeled the activity of electrical signals of the squid giant axon. The properties of the equations in the Hodgkin-Huxley model have been shown to be an excellent means of modeling electrical activity of neurons in a large number of animals and is still used today. The Hodgkin-Huxley model has also revealed the significance of mathematics in understanding biological processes of the brain.

The interest in the processes and function of the central nervous system has continued and flourished since the 19th and 20th centuries. Today, we have an even better awareness of signaling and connectivity of neurons in different regions of the brain. This has given us greater insight into so many things such as how we walk, think, breathe, and see. Furthermore, we have a better understanding of diseases and disorders of the brain such as Alzheimers, Parkinsons and multiple sclerosis. Although a considerable amount of progress has been made in our understanding of the central nervous system, the specific mechanisms by which particular cells and collections of cells in the brain produce complex behaviors remains to be fully understood.

Before attempting to understand such mechanisms from a mathematical point of view, it is first necessary to review some basic concepts and terminology of neurobiology. The brain is spatially divided into four lobes (temporal, parietal, occipital, and frontal) according to function. Each of these lobes consists of a network of interconnected cells that together produce behavior. The cells of the brain are of two types: glial cells and neurons. Neurons produce electrical signals, called action potentials, in the brain. Glial cells do not fire action potentials, but have other purposes such as providing structural support, buffering ions found in the extracellular fluid, removing debris caused by injured or dying cells, and providing nutrients and growth factors to neurons. Without glial cells, neurons cannot grow and function properly [52].

There are three classifications of neurons. Sensory neurons convey information to the nervous system for motor coordination and conscious perception. Motoneurons are responsible for sending commands to the muscles and glands. Interneurons make up the last and largest collection of neurons and are involved in all processes that are not sensory or motor related. A typical neuron contains a soma or cell body. The soma contain the nucleus and other organelles necessary for the production of energy and synthesis of proteins. Extending from the cell body are several dendrites and an axon; see Figure 1.1. Axons typically project and make a connection, called a

synapse, to the dendrite of other neurons to receive input. Through this means, the axon serves as the provider of information from the pre-synaptic neuron to connected post-synaptic neurons [36, 52].

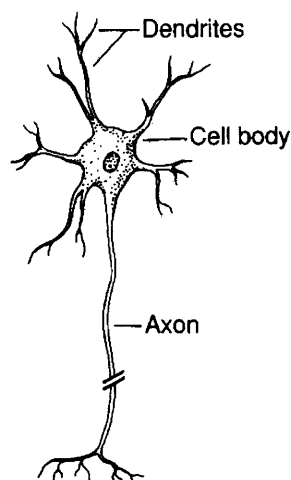


**Figure 1.1** A spinal motor neuron with a soma, axon, and dendrites [36].

The cell body of neurons is surrounded by a membrane of lipid molecules which acts to separate charged particles, called ions, that are contained on the cytoplasmic side of the cell from ions contained on the extracellular side. The membrane, therefore, causes a difference in concentration of particular types of ions from the inside of the cell to the outside of the cell. The separation of charges leads to a voltage difference across the cell membrane. The lipid bilayer, although impermeable to ions, contains membrane spanning channels made up of protein molecules that allow particular ions to flow through when the channel pore is open; see Figure 1.2. The flow of ions through these ion channels causes a change in voltage. If this change in voltage is large enough to push the voltage of the neuron above a particular threshold, then an action potential will occur. Action potentials are characterized by a fast increase in

voltage (above threshold) followed by a fast decrease in voltage back to the resting or equilibrium potential; see Figure 1.3.

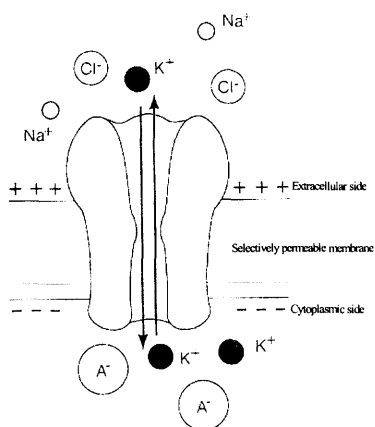


**Figure 1.2** Electrical signals in the nervous system are created by the movement of ions through channels in the cell membrane.

Action potentials are generated at the axon hillock which is close to the soma and then propagate down the cell's axon. As stated earlier, neurons communicate with one another through connections called synapses. There are two types of synapses, chemical and electrical; see Figure 1.4. Chemical synapses are the more common of the two types of synapses. For chemical synapses, the arrival of an action potential at the axon terminal of the pre-synaptic cell causes a release of chemical substances called neurotransmitters. Once the neurotransmitters are released, they diffuse across the synaptic cleft which is the small space between the axon terminal of the pre-synaptic cell and the dendrite of the post-synaptic cell. Neurotransmitters then bind to receptors of the post-synaptic dendrite. Ionotropic receptors are channels that directly open when the proper transmitter molecules bind to them. The binding of

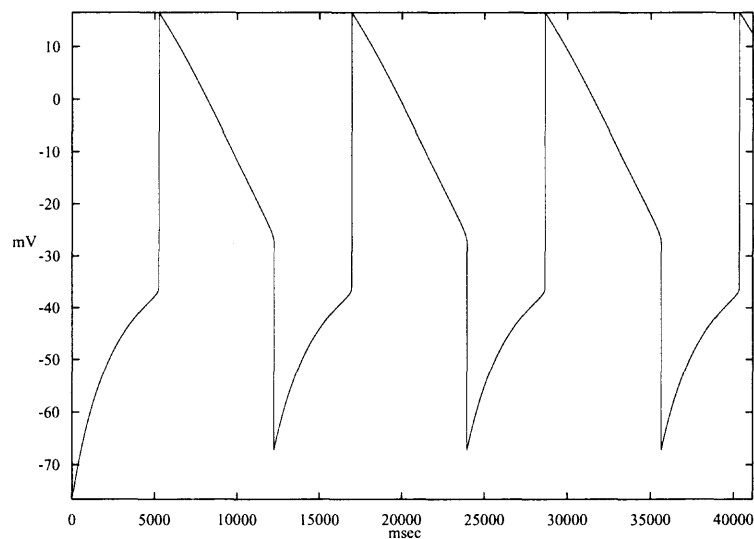


**Figure 1.3** Computer-simulated action potentials are shown. Action potentials are characterized by a fast increase in voltage (above threshold) followed by a fast decrease in voltage back to the resting or equilibrium potential.

neurotransmitters to metabotropic receptors, on the other hand, initiates a series of steps that result in the opening of ion channels. This allows ions that are specific to the channel to flow through.

Different types of neurons contain different neurotransmitters and channels responsive to different neurotransmitters. If the synapse is excitatory, the release and binding of transmitter will increase the post-synaptic cells ability to fire action potentials. If the synapse is inhibitory, the transmitter will make it more difficult for the post-synaptic cell to fire action potentials. Neurons can also communicate with one another through electrical synapses or gap junctions. Gap junctions are channels that allow ions to freely diffuse between neighboring cells and do not require the binding of neurotransmitters to open [36, 52].

Neuronal circuits involved in the generation of rhythmic behaviors such as breathing, walking, and chewing have been an area of great interest for many years [15, 25, 27]. Such networks often involve central pattern generators (CPGs) that are

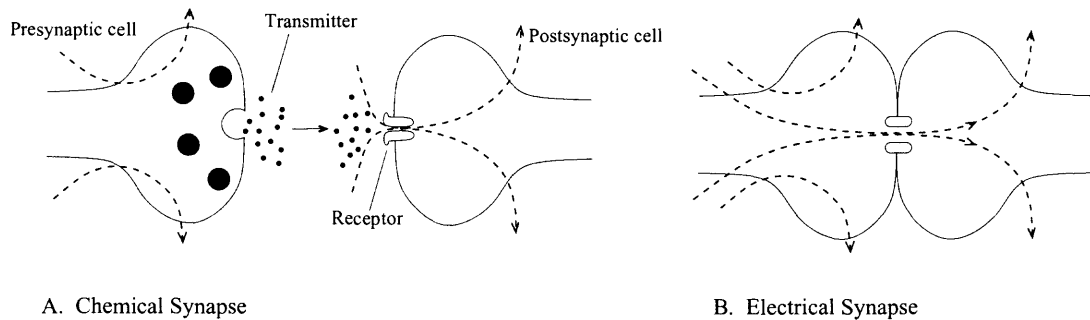


**Figure 1.4** Synaptic connections between neurons can be chemical or electrical. A.) At a chemical synapse, the pre-synaptic cell releases neurotransmitters into the synaptic cleft which can then bind to receptors of the post-synaptic cell. B.) At an electrical synapse, current can freely diffuse between neighboring cells.

composed of sets of reciprocally inhibitory neurons that rely on external stimuli to trigger oscillations or to set the appropriate frequency of the rhythm [1, 12, 60]. CPGs are neural networks that specify the rhythmicity of specific motor output for particular behaviors [33]. McFarland et al. [44], for example, showed that the respiratory rate of the rabbit slows during mastication due to inputs from the CPG involved with swallowing. Furthermore, it has been noted in many cases that multiple inputs act together to generate and set the frequency of the network [33].

A limitation on the study of such networks in the mammalian central nervous system is the complexity of these structures due to the abundance of neurons and synapses. The human brain contains approximately  $10^{11}$  neurons and  $10^{14}$  synapses [36]. A useful tool, therefore, has been to study rhythmic behavior in invertebrates which contain significantly less neurons and yet maintain many of the functional properties of the mammalian central nervous system [55, 43, 41].

The stomatogastric nervous system (STNS) of the crab *Cancer borealis* provides a good example of a system containing a conditional oscillator, made up of an asymmetric half-center oscillator, that receives multiple rhythmic synaptic inputs in order to oscillate. This dissertation uses the STNS of the crab *Cancer borealis* (of which many features hold true for other species of crustaceans) to address the issue

of how a conditional oscillator integrates rhythmic inputs to determine the frequency of its oscillations. More specifically, this work is done with the aim of mathematically explaining the experimental results of Wood et al. [73] discussed below.

Within the STNS are subnetworks whose neuronal oscillations display a broad range of frequencies that are responsible for generating various behaviors involved with digestion. The STNS contains four distinct collections of nerve cell bodies called ganglia. These are the paired commissural ganglia (CoG), oesophageal ganglia (OG), and stomatogastric ganglia (STG) which are all interconnected by nerves; see Figure 1.5<sup>1</sup>. The paired inferior (ion) and superior (son) nerves connect the CoG to the OG. The stomatogastric nerve (stn) connects the STG to both the CoG and the OG. Thus, while the cell bodies are contained in their respective ganglia, the axons of these cells are able to extend through the nerves to interact with other cells [62][67].

The stomach of the crab contains an anterior chamber called the cardiac sac and a posterior chamber called the pylorus; see Figure 1.6. During feeding, food first enters the esophagus and then gets moved into the cardiac sac. In the rear of the cardiac sac lies the gastric mill which contains 3 teeth. These teeth chew the food before it gets passed to the pylorus through the cardio-pyloric valve. Once in the pylorus, the food gets further filtered through the coordinated contraction of muscles in this region. The rhythmic protraction and retraction of the teeth in the gastric mill is generated by a subnetwork of neurons lying in the STG that innervate the muscles of the gastric mill. Thus, the gastric mill circuit elicits the gastric mill rhythm. The neurons of the pyloric subnetwork also lie in the STG and generate the pyloric rhythm [62, 67].

The frequency of the pyloric rhythm is pacemaker driven and is on the order of 1 Hz. The frequency of the gastric mill rhythm, however, lies between .05 and .2 Hz and requires multiple oscillatory inputs to become active or to oscillate at the relevant

---

<sup>1</sup>Figure is courtesy of Farzan Nadim

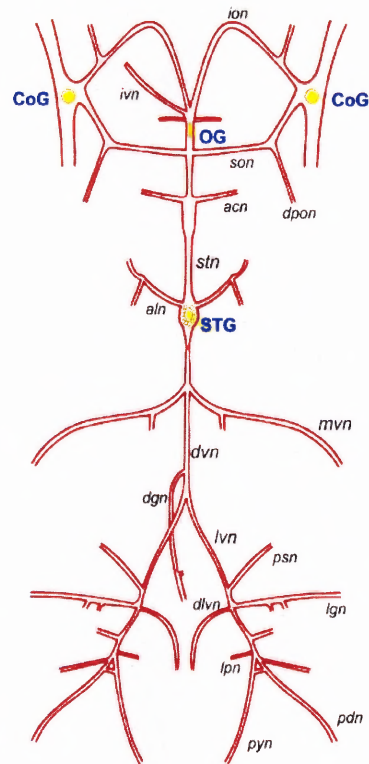


**Figure 1.5** Schematic diagram of the four ganglia of the stomatogastric nervous system and the nerves that connect them.

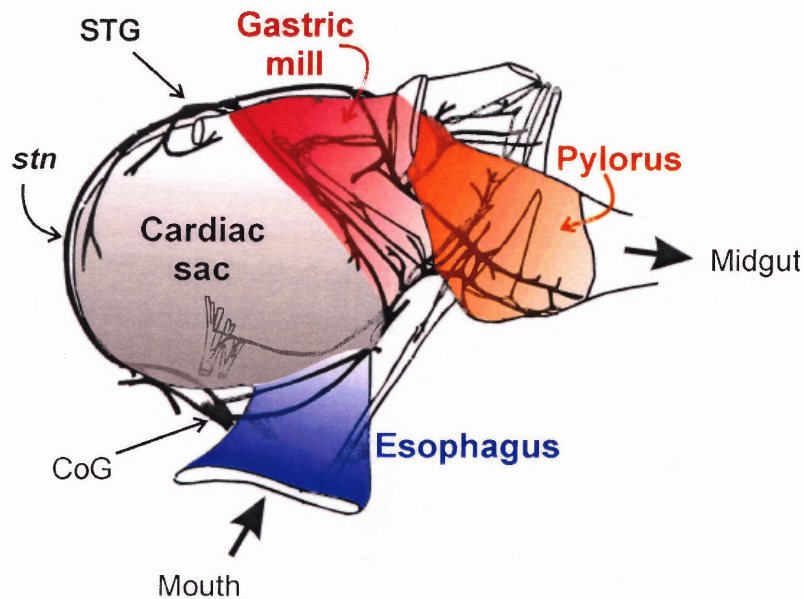


**Figure 1.6** Diagram of the stomach of crustaceans. Food first enters into the esophagus and then gets chewed by teeth in the cardiac sac. Further filtering occurs in the pylorus before the food is passed on to the midgut.

frequency. In order for digestion of food to occur in an efficient manner, the neurons of the gastric mill and pylorus must communicate with one another to ensure that the food is chewed and passed from one chamber to another properly [13, 63, 72]. Therefore, the STG is an example of a system producing rhythmic behavior through the interaction of subnetworks whose oscillations are of different frequencies. It has been observed that the firing of neurons of the gastric mill can be timed to the pyloric rhythm and vice versa [55, 70]. The study of the interaction of these two subnetworks of the STG along with input they receive from the commissural ganglia is the primary undertaking of this work.

The STG contains approximately 30 neurons which along with their synaptic connections have all been identified; see Figure 1.7<sup>2</sup>. The somata of the neurons of the STG are large in diameter (25-120  $\mu m$ ), and the STG can be removed from the intact animal and remain functional for long periods of time. This makes the network ideal for doing experimental recordings. Consequently, many of the membrane properties of the neurons, the neurotransmitters used by the neurons, and the synaptic connections have been established. These factors make the STG an extremely useful system to study and model [43, 55, 67, 72]. Furthermore, studies have shown that many of the motor patterns found *in vitro* are also seen in the intact animal [28].

There has been a considerable amount of experimental work done on the STG in an effort to determine which neurons play key roles in the generation and modulation of the gastric mill rhythm. A common feature amongst CPGs is the prevalence of inhibitory synaptic coupling and the ability to alter rhythmic output through the presence of neuromodulatory substances. The gastric mill and pylorus are not an exception to this. All of the synapses between neurons of the pyloric circuit and gastric mill circuit are inhibitory and more than 15 neuromodulatory substances have been shown to influence the STG [43, 55, 67].

---

<sup>2</sup>Figure is courtesy of Farzan Nadim

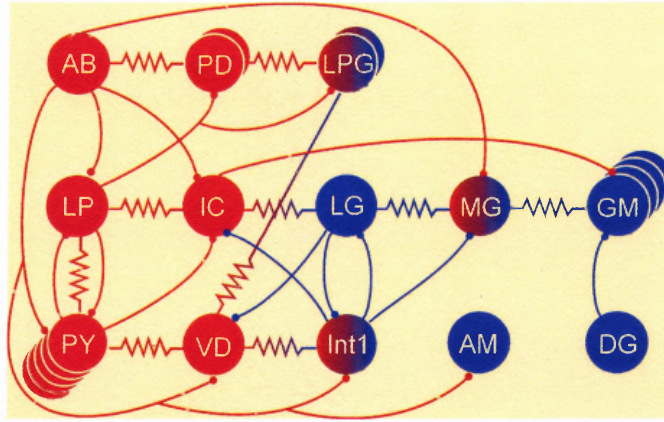


**Figure 1.7** Schematic diagram of the neurons contained in the gastric mill (blue) and the pylorus (red) along with their synaptic connections. The neurons *LPG*, *MG*, and *Int1* lie in the gastric mill but are active in pyloric time when there is no gastric mill rhythm. *LG*, *GM*, *DG*, and *AM* are gastric mill neurons and *AB*, *PD*, *LP*, *IC*, *PY*, and *VD* are pyloric neurons.

A pair of neurons, lateral gastric (*LG*) (a motoneuron) and interneuron 1 (*Int1*), with asymmetric, reciprocal inhibition between them, make up the heart of the gastric mill CPG. The reciprocal inhibition between *LG* and *Int1* allows *LG* and *Int1* to burst in antiphase with one another, thus, forming an asymmetric half center oscillator. The gastric mill rhythm is characterized by the alternating bursts of this pair of neurons [16, 40]. Bursts in *LG* constitute the protraction of the lateral gastric teeth and bursts in *Int1* constitute the retraction of the teeth [28]. However, in an isolated system of just *LG* and *Int1*, these alternating bursts do not occur. Instead, *Int1* is spontaneously active while *LG* remains at a hyperpolarized resting potential. Consequently, with no outside input, the inhibition from *Int1* further suppresses *LG* and keeps it at a low voltage below the threshold for action potential generation. As a result of the voltage of *LG* being below threshold, the synaptic inhibition from *LG* to *Int1* is not activated. This allows for repetitive or tonic firing of *Int1* [16, 40].

Activation of the gastric mill rhythm is reliant upon stimulation from projection neurons lying in the CoG's and OG. Distinct projection neurons can elicit a particular gastric mill rhythm as a consequence of transmitting different neuromodulatory sub-

stances [5, 53]. Nusbaum et al. [56] identified a projection neuron, modulatory commissural neuron 1 (*MCN1*) that excites the gastric mill rhythm. There is one *MCN1* in each of the CoG's with their axons projecting through the *ion* and into the *stn* to the STG. *MCN1* releases the modulatory substances Proctolin, GABA, and Cancer borealis tachykinin-related peptide (CabTRP) onto the STG [55, 67]. *MCN1* modulates the activity of the *LG* neuron through the release of CabTRP which has a slow onset and offset. Therefore, the effect of *MCN1* on *LG* is slow. The *Int1* neuron, on the other hand, is affected by the release of GABA which has a fast onset and offset [54, 74]. Intracellular recordings show that in the absence of *MCN1* stimulation, there is an ongoing pyloric rhythm but not a gastric mill rhythm. However, when *MCN1* is depolarized, there is an active gastric mill rhythm [56].

Recent work has also indicated the importance of voltage dependent electrical coupling between *MCN1* and *LG* in obtaining the appropriate frequency of the gastric mill rhythm. This electrical coupling acts in coordination with the chemical excitation from *MCN1* to *LG* to maintain *LG*'s active phase [16, 17, 55, 56]. The presence of the electrical synapse also makes this network interesting to study because recent work has indicated the presence of both chemical and electrical synapses in many mammalian systems [24, 26, 59]. Thus, an important issue that has emerged is to explore how these two types of synapses work in coordination with one another.

The interneuron, anterior burster (*AB*) of the pyloric network also sends synaptic input to the gastric mill network. *AB* is a pacemaker neuron that is spontaneously active with a firing frequency of 1 Hz (pyloric timing) [43, 55]. The spontaneous activity of pacemaker neurons is due to intrinsic, cyclic conductance changes of the cell membrane that slowly depolarize the cell membrane and then repolarize the cell membrane back to the resting state [64]. *AB* inhibits *Int1* through the release of the neurotransmitter glutamate and, therefore, also plays a role in determining the rhythmic behavior of the gastric mill network [49, 65]. Motivated by the findings

of Nadim et al. [49] (discussed in the following paragraph), Bartos et al. [5] used the dynamic-clamp technique to artificially replicate the *AB* current to *Int1* [66]. They showed that this synaptic input from the pyloric subnetwork to the gastric mill subnetwork is necessary in order to generate the appropriate gastric mill rhythm when *MCN1* is tonically stimulated; see Figure 1.8<sup>3</sup>. Tonic stimulation of *MCN1* is accomplished by stimulating the *ions* at a fixed frequency between 10-20 Hz.

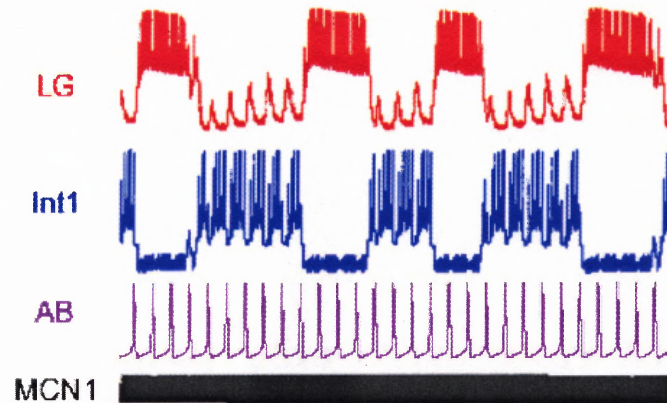


**Figure 1.8** Voltage traces of three neurons lying in the STG are shown in the presence of modulatory input from the CoG. Alternating bursts in *LG* and *Int1* make up the gastric mill rhythm and the fast oscillations of *AB* drive the pyloric rhythm. *MCN1* is a neuron lying in the CoG whose axon projects through the stn to excite the gastric mill network.

Nadim et al. [49] constructed a Hodgkin-Huxley type compartmental model of *LG* and *Int1* with synaptic input from *MCN1* and *AB*. This model demonstrated that the gastric mill rhythm is significantly slower in the absence of the inhibitory *AB* input to *Int1* and that the timing of the *LG* burst onset is strongly coordinated with *AB* activity. Manor et al. [40] later reduced this model to make mathematical analysis more plausible. Such reductions of biologically complex models have proven to be a useful means of identifying which network properties are responsible for generating particular qualitative behaviors that would otherwise be hidden by the complexity of the network. An example of such a model is the FitzHugh-Nagumo model which

<sup>3</sup>Figure is courtesy of Farzan Nadim.

reduces the set of equations describing the voltage activity of the squid giant axon in the Hodgkin-Huxley model to two coupled first order ordinary differential equations [23, 51, 61].

The reduced model of Manor et al. [40] simplifies *Int1* and *LG* into single compartment neurons with passive properties and will be discussed in more detail in Chapter 3. The reduced model also neglects electrical coupling that is present between *MCN1* and *LG* and fast excitation from *MCN1* to *Int1*. Furthermore, Manor et al. make the simplifying assumption that the voltage of *MCN1* is always above threshold. In this case, we say that the excitation from *MCN1* to *LG* is a tonic excitation. The work of Manor et al. [40] uses phase-plane analysis to show how the gastric mill rhythm is elicited and how frequency is regulated by slow excitation from *MCN1* to *LG*. They then show how the addition of the fast *AB* inhibition to *Int1* alters the frequency of the gastric mill rhythm [40].

Additional experiments to determine the effect of *MCN1* and *AB* inputs on the gastric mill rhythm were done by Wood et al. [73]. In these experiments, *MCN1* activity is rhythmic due to the presence of an inhibitory synapse from *AB* to *MCN1*. The *AB* axon projects to *MCN1* through the *stn* and *sons*. Rhythmic stimulation of *MCN1* is achieved by stimulation of the *ions* (with a fixed frequency lying within 10-25 Hz) between successive bursts of the paired pyloric dilator neurons which are electrically coupled to *AB*. Thus, *AB* provides a fast, periodic input to both *Int1* and *MCN1* [34, 73].

The goal of the work of Wood et al. was to determine if the rhythmic activity of the projection neuron *MCN1* could establish the intercircuit coordination between the gastric mill rhythm and pyloric rhythm as the *AB* input to *Int1* does when *MCN1* is tonic. Wood et al. show that in the absence of the *AB* input to *Int1*, the rhythmicity of *MCN1* is sufficient to create a gastric mill rhythm with a frequency comparable to that of the rhythm frequency when *MCN1* is tonic and *AB* periodically

inhibits *Int1*. Wood et al. then show that when the *AB* input to *Int1* is present and *MCN1* activity is rhythmic, the gastric mill rhythm frequency is the same as when the *AB* input to *Int1* is absent. This is not consistent with the case when *MCN1* is tonic in which the presence of the *AB* input to *Int1* speeds up the gastric mill rhythm. Thus, it seems that the rhythmic *MCN1* input to *LG* serves as a second pathway by which the pyloric circuit can regulate the rhythm of the gastric mill circuit.

These experiments, however, also reveal that although the pyloric input to either *Int1* or to *MCN1* allows for pyloric regulation of the gastric mill frequency, both inputs are needed for the naturally occurring rhythm to be present. This result is shown through comparisons of the duty cycle of *LG* when *MCN1* is tonic for *AB* input to *Int1* absent and present and when *MCN1* is rhythmic and *AB* input to *Int1* is absent and present. All four of these situations result in different duty cycles, thus, showing that the *AB* input to *MCN1* alone does not produce the appropriate activity pattern of *LG*. Wood et al. also showed that when *MCN1* is rhythmic, the latency locking between the activity of *MCN1* and the activity of *AB* is necessary to obtain the appropriate coordination between the gastric mill and pyloric rhythms. To show this, Wood et al. considered the effect of letting *MCN1* be rhythmic but free-running with respect to *AB* activity. In this case, the gastric mill cycle frequency and *LG* duty cycle were unaffected but the phase relationship between the onset of *LG* activity and the onset of *MCN1* and *AB* activity were affected [73].

This work leads to the consideration of four distinct cases. The first case is tonic *MCN1* activity without *AB* input to *Int1*. The second is tonic *MCN1* activity with *AB* input to *Int1*. The third case is rhythmic *MCN1* activity without *AB* input to *Int1*. The fourth case is rhythmic *MCN1* activity with *AB* input to *Int1*; see Figure 1.9.

This dissertation will revisit and expand upon the works of Nadim et al. [49], Manor et al. [40], and Wood et al. [73] to mathematically determine the means

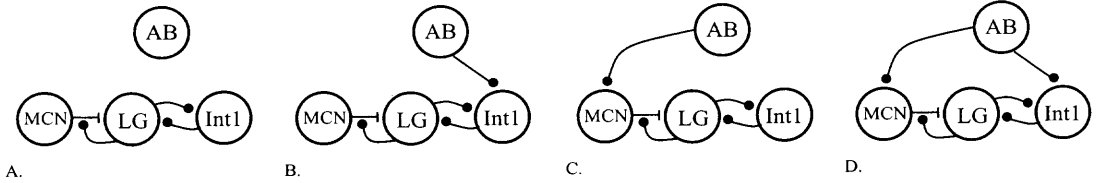


**Figure 1.9** Circuitry for Cases 1-4. (A.) The  $AB$  input to  $MCN1$  and to  $Int1$  is absent. (B.) The  $AB$  input to  $Int1$  is present but the  $AB$  input to  $MCN1$  is absent. (C.) The  $AB$  input to  $MCN1$  is present but the  $AB$  input to  $Int1$  is absent. (D.) The  $AB$  input to  $Int1$  and to  $MCN1$  is present.

by which the observed behaviors of the gastric mill rhythm are achieved. That is, when  $MCN1$  is rhythmic, what mechanism prevents the direct  $AB$  input to  $Int1$  from further increasing the gastric mill frequency as it does when  $MCN1$  is tonic? Furthermore, what is the role of the  $AB$  input to  $Int1$  in the case when the  $MCN1$  activity is rhythmic? To understand these questions, we incorporate the rhythmicity of  $MCN1$  into the model of Manor et al. [40] and then prove the existence and stability of periodic solutions using The Contraction Mapping Principle [4, 58] for the four cases described above. We then derive an analytic expression for the period of the gastric mill rhythm found in Manor et al. [40] and for the two additional cases;  $MCN1$  rhythmic with  $AB$  input to  $Int1$  absent and  $MCN1$  rhythmic with  $AB$  input to  $Int1$  present.

In an effort to make our reduced model more realistic and representative of the actual circuitry of the STG, we next consider the  $MCN1$  to  $LG$  synapse to have voltage dependent properties as opposed to simple, passive properties. Furthermore, the effect of electrical coupling between  $MCN1$  and  $LG$  on the gastric mill cycle frequency is considered. This adds an additional dimension to the reduced model because both chemical and electrical properties are now present.

Analysis of the reduced model employs the use of geometric singular perturbation theory and phase plane analysis [11, 37, 47]. The set of governing differential equations in the reduced model contains a small parameter,  $\epsilon$ , in some but not all of the

differential equations. This causes the system to act in a similar manner to a relaxation oscillator with different regimes of fast and slow dynamics. Geometric singular perturbation theory is useful, therefore, because it exploits the presence of this small parameter to reduce the system to a study on lower dimensional slow manifolds and the fast transitions between them. Considering this system in the limit as  $\epsilon$  approaches 0, the membrane potentials of *LG* and *Int1* can be tracked through the dynamics of a 1-dimensional slow variable in a 2-dimensional phase space. The direction field and solution trajectories of the set of differential equations plotted in phase space provides a useful geometric means of interpreting the behavior of the system and clarifies what conditions on the parameters are necessary for the existence of stable periodic solutions and to ensure the correct frequency of the periodic orbits. Although this analysis is done for  $\epsilon = 0$ , the results can be shown to remain valid for  $\epsilon$  sufficiently small by applying the techniques of Mishchenko and Rozov [47].

Using these mathematical tools, existence and stability of periodic solutions are proved for *MCN1* tonic and for *MCN1* rhythmic and it is deduced that the timing of the pyloric input is crucial in determining what effect it will have on the frequency of the gastric network. Over one set of timings, the modulatory input and the pyloric input work together to determine the frequency and over another set of timings, the effect of the pyloric input is diminished by the modulatory input.

We also validate these findings through numerical simulations in which we can change parameters and numerically calculate the period of the gastric mill rhythm. XPPAUT [22] is used to numerically integrate the ordinary differential equations of the reduced model and plot solution trajectories in phase space. This ordinary differential equation solving package can also be used to determine the stability of fixed points and to construct bifurcation diagrams. A comparison of these results with the experimental findings of Wood et al. [73] is then made. The results from the reduced model with rhythmic *MCN1* excitation match the experimental results

only when there is either a short delay or no delay in the timing of the *MCN1* and *AB* inputs to the gastric mill. This analysis, therefore, gives a possible biological explanation for the findings of the experimental work.

Finally, using the results of the reduced model for *MCN1* bursting, we return to the full, compartmental model of Nadim et al. [49] to test if the timing of the pyloric inputs to *Int1* and to *MCN1* have the same effect on the gastric mill cycle period. We also run simulations to determine the *LG* duty cycle in the four cases considered and the importance of the latency locking between *MCN1* and *AB* activity in the full model to make comparisons with the results found by Wood et al. [73]. This is done to further confirm the validity of the reduced model and full model and to illustrate their ability to make experimentally testable predictions about the gastric mill's interaction with the fast pyloric input and slow modulatory input. Also, analyzed in both the reduced and full models is the effect of voltage dependent electrical coupling between *MCN1* and *LG*. Numerical simulations of the compartmental model are implemented in a software package called Network developed by Farzan Nadim. Network uses a fourth order Runge Kutta integration method. This work has been published (or submitted for publication) in part in [2] and [3].

## CHAPTER 2

### OVERVIEW

This dissertation investigates the control of network frequency through the interaction of a complex set of neurons. To make this task more manageable and understandable, this work is broken down into three subsequent chapters followed by conclusions and further discussions. Chapter 3 introduces the method by which action potentials are modeled. A full, biophysical model in which this theory is applied is then presented. This full model describes the network oscillations that generate the gastric mill rhythm due to both modulatory and pyloric inputs. A reduction of this full model is then given in order to make mathematical analysis possible. This is necessary because the full model contains a large number of coupled, non-linear differential equations. This makes it difficult to determine how each component influences the frequency of the gastric mill rhythm. The simplification, on the other hand, reduces the model to a simpler set of equations. Geometric singular perturbation theory and phase plane analysis are implemented to show how modulatory input from *MCN1* and pyloric input from *AB* affect the frequency of the gastric mill network through their synaptic inputs to the neurons *LG* and *Int1*.

In Chapter 4, the frequency of the gastric mill rhythm is considered in four different cases. In the first case, only tonic excitation from *MCN1* to the gastric mill network is present. In the second case, the pyloric input along with the tonic excitation is considered. Through phase plane analysis, we show how the frequency changes from the first case to the second case. In the third case, only rhythmic excitation from *MCN1* to the gastric mill network is present. Again, the phase plane analysis is used to show how the frequency changes from the first case to the third case. Finally, in the fourth case, the pyloric input along with the rhythmic excitation

is considered. In this case, it is demonstrated how the timing between the two inputs to the gastric mill network is essential in determining if both or only one of the inputs contributes to setting the frequency of the system. In each of these cases, we describe possible solution trajectories and then construct stable periodic solutions by placing restrictions on certain parameters. Once these restrictions are placed, a formula for the frequency of the gastric mill is derived and the frequency is calculated in all four of the cases. A direct comparison between the frequency measured through in vitro experiments on the STG and calculated from the reduced model is then made. The results of the mathematical analysis of the reduced model are used to explain the experimental observations.

The reduced model is a simplification of the actual network dynamics. Therefore, in Chapter 5, the conductance of the synapse from *MCN1* to *LG* is allowed to be voltage dependent and an electrical synapse between these two neurons is put into the model. The effects of the voltage dependency of the *MCN1* to *LG* synapse and the electrical coupling between *MCN1* and *LG* on the gastric mill rhythm frequency are then investigated. Next, the *AB* inhibition of *MCN1* is incorporated into the full model. Simulations of the full model yield the same results on the control of frequency for rhythmic *MCN1* as determined by the reduced model. This verifies that the reduced model accurately describes the behavior of the gastric mill rhythm in response to rhythmic *MCN1* input.

Comparisons between the experimental results found by Wood et al. [73] and the simulation results of the full and reduced models are also made. These comparisons show that both the full model and the reduced model accurately describe the activity of the gastric mill as seen experimentally. The electrical coupling in the full model is also altered to have a voltage dependent conductance. This is done to determine if and how the voltage dependency changes the network dynamics. This work demonstrates the usefulness of making mathematical and biological reductions in

uncovering the mysteries of complicated networks. Finally, in Chapter 6, we conclude with a summary of the major findings of this work and discuss future directions that may be considered.

## CHAPTER 3

### MODELING THE STOMATOGASTRIC GANGLION

Neurons send information to one another through electrical signals called action potentials. These electrical signals can be modeled by differential equations that express the change in voltage of the neuron in response to different stimuli. The activity of the neurons *LG* and *Int1* of the gastric mill network, *AB* of the pyloric network, and *MCN1* of the CoG can be accurately described by a Hodgkin-Huxley type model. This type of model provides a detailed biophysical description of the changes in voltage of each neuron. However, this kind of model is typically difficult to analyze mathematically due to the number of equations involved and the non-linearity of the equations. Thus, one can also consider a reduced model that simplifies the equations yet still captures the qualitative behavior of the system.

#### 3.1 Modeling Action Potentials

The cell membranes of neurons cause a voltage or a difference in electrical charge from inside the cell to outside the cell. This occurs because the extracellular and intracellular media contain different concentrations of various ions that cannot pass freely through the membrane to reach an equilibrium at which the flux due to the concentration gradient and the flux due to the electric potential difference are balanced. Note that the membrane potential is always measured as voltage on the inside of the cell minus the voltage on the outside of the cell. In order for a particular type of ion to pass from inside the cell to the outside or vice versa, channels for that particular ion must be open. The flow of ions through the channels results in a change in the voltage, thus, producing an electrical signal. If negative ions move out of the cell or positive ions move into the cell, the membrane voltage increases. Similarly, if positive ions move out of the cell or negative ions move into the cell, the

voltage decreases. If the flow of ions causes the voltage to increase above a particular threshold, the electrical signal is called an action potential.

When an ion channel is open, two forces act upon the corresponding ions to determine if the ion will pass through the membrane. The first force is diffusion which is a result of the unequal concentrations of the ion inside the cell and outside the cell. Ions want to flow from areas of high concentration to areas of low concentration until a balance is reached. The second force acting on ions is due to the electrical potential difference. That is, ions want to flow through the membrane in a manner that creates an equal number of positively and negatively charged ions on the extracellular and cytoplasmic sides of the cell membrane. At equilibrium, these two forces must balance so that there is no net movement of charge through the membrane.

The Nernst equation can be used to calculate the value of the voltage at which the diffusive and drift forces acting on specific ions are at equilibrium. This value of the voltage is called the Nernst potential of the ion. The Nernst equation simply uses the fact that at rest, the sum of the forces acting on the ions must be equal to 0. In other words, the sum of the diffusive and drift fluxes must sum to 0:

$$J_{diff} + J_{drift} = 0. \quad (3.1)$$

Fick's law of diffusion states that

$$J_{diff} = -D \frac{d[C]}{dx} \quad (3.2)$$

where  $D$  is the diffusion coefficient,  $[C]$  is the concentration of the ion, and  $x$  is a spatial variable. Ohm's law for drift states that

$$J_{drift} = -uz[C]\frac{dV}{dx} \quad (3.3)$$

where  $u$  is the mobility of the ions,  $z$  is the valence of the ions, and  $V$  is the voltage. Plugging (3.2) and (3.3) into (3.1), using Einstein's relation,  $D = \frac{RT}{F}u$ , where  $R$  is the universal gas constant,  $F$  is Faraday's constant, and  $T$  is the absolute temperature in degrees Kelvin, and integrating, one obtains the equation for the Nernst potential:

$$E_{ion} = \frac{RT}{zF} \ln \frac{[C]_{out}}{[C]_{in}}. \quad (3.4)$$

where  $[C]_{out}$  and  $[C]_{in}$  are the concentrations of the specific ion on the outside and on the inside, respectively.

A crucial observation about the cell membrane is that it separates charges and, therefore, acts as a capacitor. The capacitive current is  $I_C = \frac{dQ}{dt} = C\frac{dV}{dt}$  where  $Q$  is charge and  $C$  is the capacitance. Furthermore, each type of ion channel allows only selective ions to pass through when the channels are open and, therefore, act as conductors. From Ohm's law,  $I_{ion} = g_{ion}(V - E_{ion})$  where  $I_{ion}$  is the ionic current and  $g_{ion}$  is the conductance of the channel to that ion. Kirchoff's Law states that all of the currents flowing into and out of a node in an electrical circuit must be equal to 0. This tells us that the capacitive current,  $I_C$ , and the resistive currents due to the different ion channels,  $I_{ion}$ , must sum to 0. This gives us an equation for the change in voltage:

$$C\frac{dV}{dt} = -\sum I_{ion} + I_{app}, \quad I_{ion} = g_{ion}(V - E_{ion}) \quad (3.5)$$

where  $I_{app}$  is an applied current. In many cases  $g_{ion}$  is a function of voltage and time so that as the voltage of the cell increases or decreases, the conductance of the channel

increases or decreases. In other words, as the voltage changes, the proportion of that type of ion channel that are open changes. In this case, we say that the ion channels are voltage-gated. These types of channels are responsible for the firing of action potentials because they drive the voltage away from the resting potential and then back down to the resting potential. In other cases, however,  $g_{ion}$  may be a constant in which case we say that the channel has passive properties. Passive channels contribute to the value of the resting potential but not to the generation of action potentials. In other words, a membrane containing only passive or leak channels cannot fire action potentials. A neuron that is capable of firing action potentials is said to be excitable [36, 37].

Electrical signals are described by the change in voltage that they produce as well as the rates of rise and decay of the change in voltage. These properties are dependent upon the ions that are present in the intracellular and extracellular spaces and the conductance of the ion channels. A well accepted means of describing these electrical signals is based upon a set of differential equations derived by Hodgkin and Huxley [29, 30, 31, 32]. Hodgkin and Huxley conducted a series of voltage clamp experiments on the squid giant axon that allowed them to measure the ionic currents through the axonal membrane at fixed levels of voltage. From these experiments, Hodgkin and Huxley determined that  $Na^+$  channels and delayed-rectifier  $K^+$  channels contributed to these currents. Delayed-rectifier  $K^+$  channels activate after the  $Na^+$  channels activate and bring the voltage of the cell back to rest. Hodgkin and Huxley then determined the ionic conductances of these channels using Ohm's law. Hodgkin and Huxley repeated this experiment for various voltages to get current versus voltage plots and then derived mathematical expressions for the ionic conductances to fit the data. A key element of these derivations was that Hodgkin and Huxley modeled the ionic conductances as a maximal conductance times one or more gating functions which take values between 0 and 1. The gating functions measure the proportion of

voltage-dependent ion channels that are in the open state. Furthermore, Hodgkin and Huxley found that the gating functions could be modeled as exponential functions raised to a particular power. For example, the conductance of the voltage-gated  $K^+$  channels was modeled as:

$$g_{K^+}(V, t) = \bar{g}_K n^4 \quad (3.6)$$

where  $\bar{g}_K$  is the maximal conductance which is a constant value and  $n$  measures the proportion of  $K^+$  channels that are in the open state. Therefore, if we let  $\alpha_n(V)$  be the rate at which the channels open (activate) and  $\beta_n(V)$  be the rate at which the channels close (deactivate) then,

$$\frac{dn}{dt} = \alpha_n(V)(1 - n) - \beta_n(V)n. \quad (3.7)$$

Using some basic algebra, (3.7) can be rewritten as:

$$\frac{dn}{dt} = \frac{n_\infty(V) - n}{\tau_n(V)}, \quad n_\infty(V) = \frac{\alpha_n(V)}{\alpha_n(V) + \beta_n(V)}, \quad \tau_n(V) = \frac{1}{\alpha_n(V) + \beta_n(V)}. \quad (3.8)$$

On the other hand, Hodgkin and Huxley found that the conductance of the voltage-gated  $Na^+$  channel had to involve the product of two gating functions,  $m$  and  $h$ , where as in (3.7),  $m$  is an activation function and the additional variable  $h$  is an inactivation function which also lies between 0 and 1. The inactivation function of the  $Na^+$  channels arises because while the  $Na^+$  channels of the squid giant axon are open, a change in the structure of the channels occurs that blocks  $Na^+$  ions from flowing through the channels. This does not occur for the  $K^+$  channels.

From their experiments, Hodgkin and Huxley concluded that the  $Na^+$  channels are responsible for the rising phase of the action potentials generated by the squid

giant axon and the delayed-rectifier  $K^+$  channels are responsible for the fall of the membrane potential back towards the resting potential. This is because the  $Na^+$  channels begin to open before the  $K^+$  channels open and  $E_{Na}$  is positive which drives the voltage upward. Once the voltage becomes large, however, the  $Na^+$  channels inactivate, thus, preventing  $Na^+$  ions from further flowing through the channel pore. Simultaneously, the  $K^+$  channels begin to open and the negative value of  $E_K$  drives the voltage slightly below the resting potential. The membrane potential then returns to the resting potential as the  $K^+$  and  $Na^+$  channels close.

Although the work of Hodgkin and Huxley is specific to the squid giant axon, equations of the type (3.5) can be used to describe changes in voltage of neurons in general. However, (3.5) assumes that the action potentials generated by the specific neuron modeled are nonpropagating. In other words, the cell membrane is excited uniformly. Using cable theory, the study of partial differential equations that describe the change in the electrical potential in thin, elongated processes, models for propagating action potentials can also be derived. However, this thesis will not involve such models [35]. Instead, the full model of Nadim et al. [49] which is expanded upon in the foregoing work compartmentalizes each neuron and describes the electrical activity of each compartment by equations of the type (3.5). A reduction of the full model will then involve equations of the same type but with passive properties, i.e. constant conductances.

### 3.2 Modeling Synapses

Neurons transmit electrical signal along their axons and communicate to other neurons through connections called synapses. Synapses can be of two major classifications: chemical synapses and electrical synapses. At chemical synapses, action potentials arriving at the axon terminal in the pre-synaptic cell cause the release of neurotransmitters that then diffuse across the synaptic cleft to the post-synaptic cell. The binding

of neurotransmitters to receptors on the membrane of the post-synaptic cell either directly or indirectly causes channels on the membrane of the post-synaptic cell to open. Once these channels open, specific ions can pass through the channel pore, thus, resulting in a change in voltage of the post-synaptic cell. Therefore, in the presence of a chemical synapse, a synaptic current term must be added to the Equation (3.5) of the post-synaptic cell. The synaptic current must also obey Ohm's law and, therefore, has the form:

$$I_{syn} = g_{syn}(V - E_{syn}) \quad (3.9)$$

where  $g_{syn}$  is the synaptic conductance and  $E_{syn}$  is the synaptic reversal potential. Consequently, letting  $V_{post}$  be the voltage of the post-synaptic cell, we obtain an equation of the form:

$$C \frac{dV_{post}}{dt} = - \sum g_{ion}(V_{post} - E_{ion}) - g_{syn}(V_{post} - E_{syn}) + I_{app}. \quad (3.10)$$

If  $E_{syn}$  is greater than the threshold for action potential generation, the synapse is excitatory because the synaptic current increases the likelihood for the firing of action potentials in the post-synaptic cell. If  $E_{syn}$  is less than the threshold for action potential generation, the synapse is termed inhibitory because it decreases or inhibits the chances for the firing of action potentials.

Similar to the conductance terms of the ionic currents in the Hodgkin-Huxley model,  $g_{syn}$  can also be expressed as a maximal conductance,  $\bar{g}_{syn}$  times a gating function,  $s$ , which varies continuously between 0 and 1 and whose value is dependent upon the voltage of the pre-synaptic cell. The gating function is dependent upon the voltage of the pre-synaptic cell because the conductance of the synapse is an increasing function of the amount of neurotransmitter being released by the pre-synaptic cell

and binding to receptors located in the post-synaptic cell membrane. The release of neurotransmitter by the pre-synaptic cell occurs only when the pre-synaptic cell is sufficiently depolarized. One common model of the synaptic input is to let  $s$  satisfy the following differential equation:

$$\frac{ds}{dt} = \begin{cases} (1-s)/\tau_r & V_{pre} \leq V_{Th} \\ -s/\tau_f & V_{pre} > V_{Th} \end{cases} \quad (3.11)$$

where  $V_{pre}$  is the voltage of the pre-synaptic cell and  $V_{Th}$  the threshold for action potential generation of the pre-synaptic cell. This equation says that if the pre-synaptic cell fires an action potential, (i.e, it's voltage goes above threshold) the channels on the post-synaptic cell's membrane should open, driving  $s$  towards 1 with rate  $1/\tau_r$ . As  $s$  increases to 1, the synaptic term,  $I_{syn}$ , turns on allowing the post-synaptic cell to receive the synaptic current. When the voltage of the pre-synaptic cell is below threshold,  $s$  decreases back to 0 with rate  $1/\tau_f$  and the synaptic input from the pre-synaptic to the post-synaptic cell is removed.

Electrical synapses differ from chemical synapses in that they allow ionic current to freely diffuse from one neuron to another through gap junction channels that directly connect neighboring cells. Electrical synapses can be unidirectional meaning that the current passes only in only direction or bidirectional meaning that the ionic current can pass in either direction between the two electrically coupled cells. In the presence of an electrical synapse between neuron 1 with voltage  $V_1$  and neuron 2 with voltage  $V_2$ , the equation to describe the change in voltage of neuron 1, given by (3.5), will receive a synaptic current term of the form:

$$I_{elec} = g_{elec}(V_1 - V_2). \quad (3.12)$$

Thus, equation (3.5) will become

$$C \frac{dV_1}{dt} = - \sum g_{ion}(V_1 - E_{ion}) - g_{elec}(V_1 - V_2) + I_{app}. \quad (3.13)$$

Again,  $g_{elec}$  is the conductance of the electrical synapse and can be constant or voltage dependent. The electrical coupling term drives  $V_1$  towards  $V_2$ . The neurons of the stomatogastric ganglion which are studied in this thesis, have both chemical and electrical synapses.

### 3.3 The Gastric Mill Rhythm and The Full Model

As stated in the introduction, the stomatogastric nervous system of the crab *Cancer borealis* contains four ganglia which together regulate the digestion of food. Within the STG lies the pyloric subnetwork which generates the fast, pyloric rhythm and the gastric mill subnetwork which generates the slower gastric mill rhythm. The pyloric rhythm is intrinsically driven by the pacemaker neuron *AB* that oscillates with a period of approximately 1sec. The gastric mill rhythm, however, requires external input to oscillate. One particular source of input that we look at is excitatory input from *MCN1* whose soma lies in the CoG and whose axon projects to the STG. In addition, pyloric input to the gastric mill can affect the frequency of the gastric mill rhythm. The neuron *AB*, for instance, inhibits the neuron *Int1* which lies in the gastric mill and inhibits *MCN1* which modulates the gastric mill rhythm.

Although the STG contains approximately 25 coupled neurons (shown in Figure 1.7), the gastric mill rhythm is generated by the antiphase oscillations of just two neurons, *LG* and *Int1*. One can, therefore, determine how modulatory input from *MCN1* and pyloric input from *AB* affect the gastric mill rhythm by considering their effect on the neurons *LG* and *Int1*. To this end, we consider a simplified network of just *Int1*, *LG*, *MCN1*, and *AB* with asymmetric, reciprocal inhibition between *LG*

and *Int1*, a fast excitatory synapse from *MCN1* to *Int1*, a slow excitatory synapse from *MCN1* to *LG*, a fast inhibitory synapse from *LG* to the *MCN1* axon terminal, voltage-dependent electrical coupling between *MCN1* and *LG*, and fast inhibitory synapses from *AB* to *Int1* and to *MCN1*.

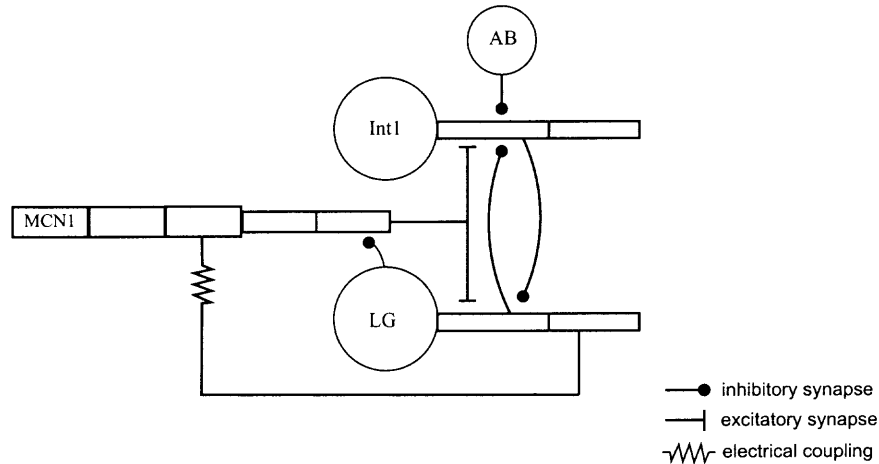


**Figure 3.1** Schematic diagram of the full model of the *AB* and *MCN1* elicited gastric mill rhythm constructed by Nadim et al. [49].

Nadim et al. [49] constructed a detailed, biophysically based model of the neurons *LG* and *Int1* that lie in the gastric mill and whose antiphase oscillations make up the gastric mill rhythm. Also included in this detailed model is *MCN1* whose excitatory input to the gastric mill network elicits the gastric mill rhythm and the pacemaker neuron *AB* that periodically inhibits both *MCN1* and *Int1*. In their model, however, Nadim et al. only consider the inhibition from *AB* to *Int1* and not from *AB* to *MCN1*. *LG* and *Int1* are modeled as having three compartments and *MCN1* is modeled as having five compartments with the change in voltage of each compartment described by a Hodgkin-Huxley type equation. Consecutive compartments of each of these neurons are symmetrically coupled; see Figure 3.1. The change in the membrane potential of each compartment is described by

$$-C \frac{dV}{dt} = I_{total}, \quad I_{total} = I_{leak} + \sum I_{ion} + \sum I_{syn} + \sum I_{axial} - I_{app} \quad (3.14)$$

$$I_{ion} = \bar{g}_{ion} m^p h^q (V - E_{ion}), \quad \tau_x(V) \frac{dx}{dt} = x_\infty(V) - x, \quad x = m, h \quad (3.15)$$

$$x_\infty(V) = 1/(1 + \exp(k(V - V_k))), \quad \tau_x(V) = \tau_1 + \tau_2/(1 + \exp(l(V - V_l))) \quad (3.16)$$

where  $V_k$  is the half-activation voltage of the channel and  $k$  determines the slope at this point.  $\tau_1$ ,  $\tau_2$ ,  $l$ , and  $V_l$  are constants that specify the rate at which the channels open and close. The current flowing into and out of each compartment in the axial direction is denoted by  $I_{axial}$ . Chemical synapses between *MCN1*, *LG*, and *Int1* are of the form

$$I_{syn} = \bar{g}_{syn} s (V - E_{syn}) \quad (3.17)$$

$$\tau_s(V_{pre}) \frac{ds}{dt} = s_\infty(V_{pre}) - s, \quad \tau_s(V_{pre}) = \tau_3 + \tau_4/(1 + \exp(\lambda(V_{pre} - V_\lambda))) \quad (3.18)$$

$$s_\infty(V_{pre}) = 1/(1 + \exp(\kappa(V_{pre} - V_\kappa))) \quad (3.19)$$

where  $V_\kappa$  is the half-activation voltage of the synaptic current and  $\kappa$  determines the slope at this point.  $\tau_3$ ,  $\tau_4$ ,  $\lambda$ , and  $V_\lambda$  are constants that specify the rate at which the synaptic currents turn on and off. The electrical synapse between *MCN1* and *LG* is of the form

$$I_{elec} = g_{elec}(V - V_{neighbor}). \quad (3.20)$$

where  $V_{neighbor}$  is the voltage of the coupled neuron.

The three compartments of *LG* and *Int1* represent the soma, neurite, and axon. Here and throughout this work, the neurite refers solely to the dendritic processes of the neuron. In Figure 3.1, the soma is represented by a circle, the neurite is the compartment next to the soma, and the axon is the compartment next to the neurite. This type of unipolar structure is often seen in invertebrate neurons [62]. The soma and neurite of both of these cells are modeled as having passive properties. The axons of *LG* and *Int1* are the compartments responsible for spike-generation and, therefore, contain a fast  $Na^+$  current, delayed-rectifier  $K^+$  current, and leak or passive current. The axon of *Int1* also contains a hyperpolarization-activated inward current to help it escape from the inhibition of *LG* [49].

The five compartments of *MCN1* represent the axon and axonal terminal. The axon of *MCN1* is the location of electrical coupling between *MCN1* and *LG*. The axon terminal is the site of the excitatory synapses from *MCN1* to *Int1* and to *LG* and the site of pre-synaptic inhibition from *LG* to *MCN1*. The axon terminal is passive and similar to *LG* and *Int1*, the axon has fast  $Na^+$ , delayed-rectifier  $K^+$ , and leak currents.

*AB* is modeled by one compartment with a leak current and  $Ca^{2+}$  current so that the frequency of *AB* activity has a fixed period of 1 sec. The synaptic current from *AB* to *Int1* is modeled as:

$$I_{AB}(t) = \frac{g_{max}t}{\tau} \exp\left(-\frac{t}{\tau}\right) (V_{Int1} - E_{AB \rightarrow Int1}). \quad (3.21)$$

In the present work, we add the inhibitory current from  $AB$  to  $MCN1$  in the full model by turning  $MCN1$  off with a fixed delay after each time  $AB$  fires an action potential. The parameters for the ionic and synaptic currents can be found in Appendix A. The voltage traces of  $Int1$  and  $LG$  when the  $AB$  inputs to  $MCN1$  and to  $LG$  are not present are shown in Figure 3.2

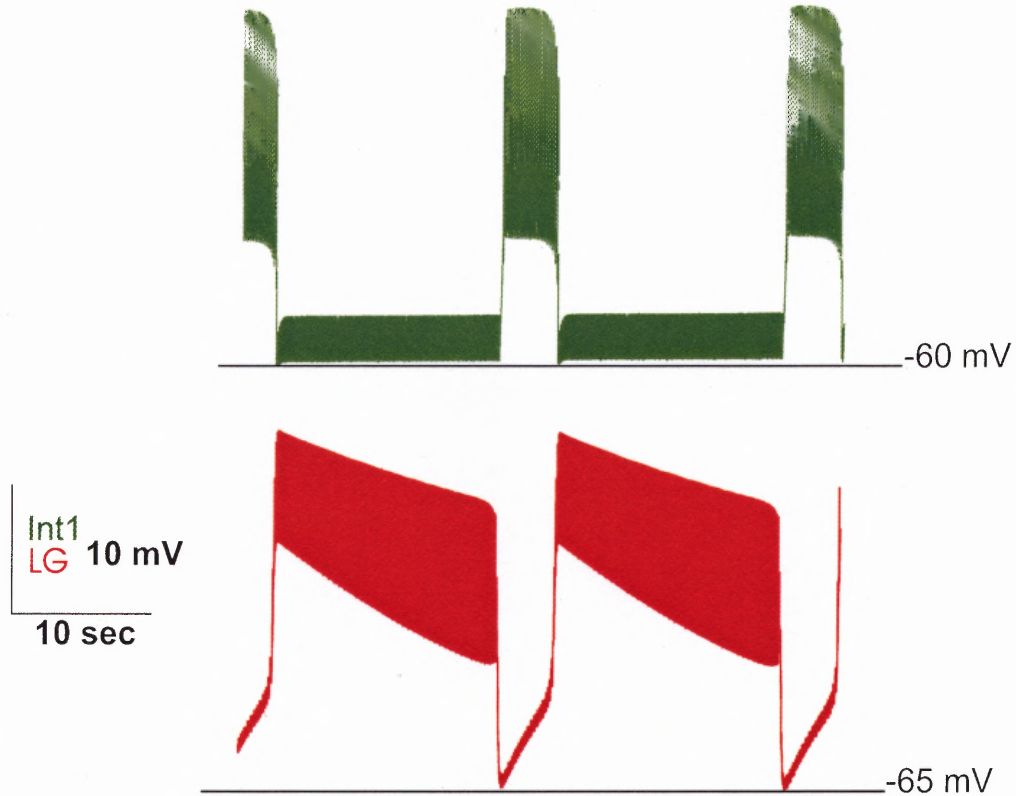


**Figure 3.2** Voltage traces of  $LG$  (lower trace) and  $Int1$  (upper trace) computed from simulation of the full model when the  $AB$  inputs to  $MCN1$  and to  $Int1$  are not present.

### 3.4 The Expanded Reduced Model

The detailed compartmental model of Nadim et al. [49] is an excellent model for showing the behavior of the gastric mill rhythm and the significance of the pyloric and modulatory inputs on the gastric mill rhythm. Due to the complexity and large number of differential equations in the model, however, it is difficult to analyze and understand the dynamics of the membrane potential of each neuron from a

mathematical perspective. Therefore, it is useful to consider a reduced model of the gastric mill network that neglects the intricate details but maintains the essential features of the electrical activity and interactions of the neurons.

A reduction of the full model of Nadim et al. [49] was done by Manor et al. [40]. This reduced network models the slow envelopes of the *LG* and *Int1* oscillations and ignores the fast spiking activity of the cells. In this model, *LG*, and *Int1* are passive neurons with one compartment. *LG* is modeled as having a subthreshold resting potential and *Int1* has a suprathreshold resting potential. *MCN1* is not explicitly modeled but is assumed to have a suprathreshold resting potential so that the excitatory synapse to *LG* is always turned on. Thus, when *MCN1* does not receive input from the pyloric network, the voltage of *MCN1* is assumed to be constant. As stated earlier, we refer to *MCN1* as tonic and the excitation from *MCN1* to *LG* as a tonic excitation in this case. The reduced model includes the reciprocally inhibitory synapses between *LG* and *Int1*, the slow excitatory synapse from *MCN1* to *LG*, the fast pre-synaptic inhibition of *MCN1* by *LG*, and the fast, inhibitory synapse from *AB* to *Int1*.

In this work, we expand upon the model of Manor et al. [40] to include the fast, inhibitory synapse from *AB* to *MCN1*. In this case, we say that *MCN1* is rhythmic because *MCN1* becomes hyperpolarized each time *AB* is in its active state. This synapse is added to the network so that we can determine the effect of rhythmic *MCN1* activity on the gastric mill rhythm frequency. To incorporate the effect of this synapse on the gastric mill rhythm, we explicitly model *MCN1* as a single compartment passive neuron with a suprathreshold resting potential. Furthermore, we consider the effect of making the conductance of the excitatory synapse from *MCN1* to *LG* voltage dependent and we add voltage dependent electrical coupling between *MCN1* and *LG*. We refer to this new model as the expanded, reduced model; see Figure 3.3.

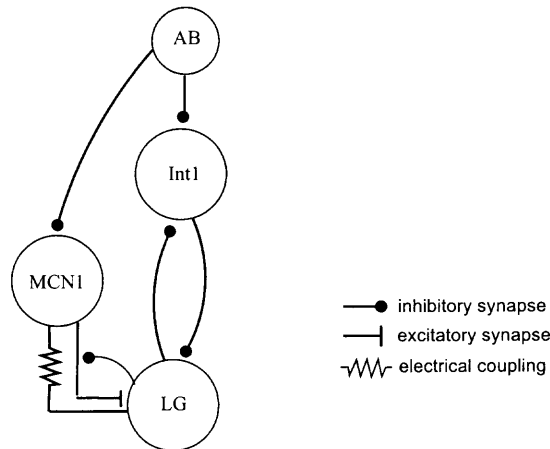


**Figure 3.3** Schematic representation of the expanded, reduced model of the *MCN1* and *AB* elicited gastric mill circuit.

We do not explicitly model the pacemaker neuron *AB*, but instead incorporate its effect on *Int1* and *MCN1* through the synaptic variables  $s_{AB \rightarrow I}(t)$  and  $s_{AB \rightarrow M}(t)$ .  $s_{AB \rightarrow I}(t)$  is a square wave with amplitude 1 and period,  $P_{AB}$ , which has experimentally been found to be approximately 1 *sec*. We let  $D_c$  denote the duty cycle of *AB* (the ratio of its active time to its period). During one period of *AB*, the variable  $s_{AB \rightarrow I}$  is equal to 1 for a time  $D_c P_{AB}$  and equal to 0 for a time  $P_{AB}[1 - D_c]$ .  $s_{AB \rightarrow M}(t)$  is similar in form to  $s_{AB \rightarrow I}(t)$  in that  $s_{AB \rightarrow M}$  takes oscillates between 0 and 1. The jump in  $s_{AB \rightarrow M}$  from 0 to 1 is instantaneous. However,  $s_{AB \rightarrow M}$  decreases from 1 to 0 with time constant  $\tau_{AB}$ ; see Figure 3.4. The differential equation that describes this behavior will be given later in this section.

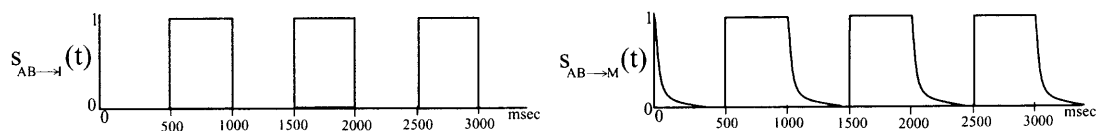


**Figure 3.4** The synaptic variables  $s_{AB \rightarrow I}(t)$  and  $s_{AB \rightarrow M}(t)$ . Note that  $s_{AB \rightarrow M}(t)$  decays with time constant  $\tau_{AB}$ .

The dimensional set of equations that describe the gastric mill rhythm are presented in Appendix B. In this Appendix, these equations are non-dimensionalized

and reveal that the dynamics of the system evolve on two distinct time scales. One is a slow time scale corresponding to the effect of slow pre-synaptic inhibition from *LG* to the excitatory component of the *MCN1* synapse. The other is a fast time scale along which all other synaptic and intrinsic properties evolve. The small parameter,  $\epsilon$ , characterizes the ratio of the fast and slow time scales. In Appendix B, it is shown that  $\epsilon = \tau/\tau_{AB}$  where  $\tau$  is the membrane time constant of *MCN1*. In this work, we will be using the non-dimensionalized system of equations to perform the analytic computations and the dimensionalized system of equations to perform the numeric computations.

The non-dimensionalized equations that describe the activity of *LG*, *Int1*, and *MCN1* are:

$$\begin{aligned} \epsilon \frac{dV_L}{dt} = & -g_{leak,L}[V_L - E_{leak,L}] - \bar{g}_{I \rightarrow L} n_\infty(V_I)[V_L - E_{I \rightarrow L}] \\ & - g_s(V_L) s(t)[V_L - E_{exc}] - g_{elec}(V_L)[V_L - V_M] \end{aligned} \quad (3.22)$$

$$\begin{aligned} \epsilon \frac{dV_I}{dt} = & -g_{leak,I}[V_I - E_{leak,I}] - \bar{g}_{L \rightarrow I} n_\infty(V_L)[V_I - E_{L \rightarrow I}] \\ & - \bar{g}_{AB \rightarrow I} s_{AB \rightarrow I}(t)[V_I - E_{AB \rightarrow I}] \end{aligned} \quad (3.23)$$

$$\epsilon \frac{dV_M}{dt} = -g_{leak,M}[V_M - E_{leak,M}] - \bar{g}_{AB \rightarrow M} s_{AB \rightarrow M}(t)[V_M - E_{AB \rightarrow M}] \quad (3.24)$$

where  $V_L$  is the voltage of *LG*,  $V_I$  is the voltage of *Int1*, and  $V_M$  is the voltage of *MCN1*.  $g_{leak,L}$ ,  $g_{leak,I}$ , and  $g_{leak,M}$  are the conductances of the leak currents in *LG*, *Int1*, and *MCN1*.  $E_{leak,L}$ ,  $E_{leak,I}$ , and  $E_{leak,M}$  are the reversal potentials of the leak currents in *LG*, *Int1*, and *MCN1*. As determined by the non-dimensionalization

of the equations found in Appendix B,  $E_{leak,M} = 1$ . Denote the right-hand sides of equations (3.22) and (3.23) by  $f(V_L, V_I, s)$  and  $g(V_I, V_L, s_{AB \rightarrow I})$ , respectively.

The parameters of the reciprocally inhibitory synapses between *Int1* and *LG* are  $\bar{g}_{I \rightarrow L}$  and  $\bar{g}_{L \rightarrow I}$  (the maximal conductances) and  $E_{I \rightarrow L}$  and  $E_{L \rightarrow I}$  (the reversal potentials).  $n_\infty(V_I)$  and  $n_\infty(V_L)$  are sigmoidal shaped gating functions lying between 0 and 1:

$$n_\infty(V_x) = \left( 1 + \exp \frac{v_x - V_x E_{leak,M1}}{k_x} \right)^{-1} \quad (3.25)$$

where  $v_x$  is the half-activation voltage and  $k_x$  is inversely related to the slope at this point and  $E_{leak,M1}$  appears as a result of the non-dimensionalization discussed in Appendix B.

The fast, periodic inhibitory input from the neuron *AB* to *MCN1* is described by  $\bar{g}_{AB \rightarrow M} s_{AB \rightarrow M}(t) [V_M - E_{AB \rightarrow M}]$  where  $\bar{g}_{AB \rightarrow M}$  is the conductance of the synapse and  $E_{AB \rightarrow M}$  is the reversal potential.  $E_{AB \rightarrow M}$  is chosen to be less than the threshold for *MCN1* activity, denoted by  $V_{Th(M)}$ , so that the input from *AB* to *MCN1* is inhibitory. The equation to describe the activity of  $s_{AB \rightarrow M}(t)$  with respect to *AB* is

$$\epsilon \frac{ds_{AB \rightarrow M}}{dt} = \begin{cases} [1 - s_{AB \rightarrow M}] / \tau_M & V_{AB} \geq V_{Th(AB)} \\ -\epsilon s_{AB \rightarrow M} & V_{AB} < V_{Th(AB)} \end{cases} \quad (3.26)$$

where  $V_{AB}$  is a square wave with period  $P_{AB}$  and duty-cycle=0.5. Thus, when  $s_{AB \rightarrow M} = 0$ ,  $V_M$  lies at a maximum voltage of  $E_{leak,M}$ . When  $s_{AB \rightarrow M} = 1$ ,  $V_M$  lies at a minimum voltage of  $V_M^*$  where

$$V_M^* = \frac{g_{leak,M} E_{leak,M} + \bar{g}_{AB \rightarrow M} E_{AB \rightarrow M}}{g_{leak,M} + \bar{g}_{AB \rightarrow M}}. \quad (3.27)$$

The periodic, inhibitory input from  $AB$  to  $Int1$  is given by  $\bar{g}_{AB \rightarrow I} s_{AB \rightarrow I}(t)(V_I - E_{AB \rightarrow I})$ .  $\bar{g}_{AB \rightarrow I}$  is the conductance and  $E_{AB \rightarrow I}$  is the reversal potential. To consider the case when  $AB$  does not inhibit  $Int1$ , we set  $\bar{g}_{AB \rightarrow I} = 0$ . An important aspect of this work is to highlight the fact that different phase relationships of  $AB$  input to  $MCN1$  and  $Int1$  lead to dramatically different frequencies of the gastric mill rhythm. To this end, the parameter,  $m$ , is used to delay the  $AB$  input to  $Int1$  relative to  $MCN1$ . In other words, if the  $AB$  input to  $MCN1$  turns on at  $t = 0$ , the input from  $AB$  to  $Int1$  does not turn on until  $t = m$ . The parameter  $m$  is a constant which can range between 0 and  $P_{AB}$  (the period of  $AB$ ).

The voltage dependent electrical coupling between  $MCN1$  and  $LG$  is added into the reduced model through a unidirectional synapse from  $MCN1$  to  $LG$ . The conductance of this electrical synapse increases as the voltage of  $LG$  increases and is modeled by  $g_{elec}(V_L)$  where  $g_{elec}(V_L) = \bar{g}_c g_\infty(V_L)$ .  $\bar{g}_c$  is a maximal conductance and  $g_\infty(V_L)$  is a sigmoidal shaped gating function lying between 0 and 1 of the form (3.25).

The effect of the excitation that  $LG$  receives from  $MCN1$  is seen in (3.22) by  $g_s(V_L)s(t)[V_L - E_{exc}]$  where  $g_s(V_L) = \bar{g}_s s_\infty(V_L)$  is the voltage dependent conductance of the synapse,  $E_{exc}$  is the reversal potential and  $s(t)$  models the amount of excitation  $LG$  receives. The function  $s_\infty$  is a sigmoidal gating function similar in form to  $m_\infty$ . Its exact form will be discussed later in Chapter 5.

We express  $s(t) = s_1(t)s_2(t)$  as the product of two different effects.  $s_2(t)$  models the effect of the rhythmicity of  $MCN1$  on the excitatory component from  $MCN1$  to  $LG$ . As in Manor et al. [40],  $s_1(t)$  models the pre-synaptic inhibition of the slow excitatory synapse. Thus,  $s_1$  decreases to 0 when the pre-synaptic inhibition turns on and  $s_1$  increases to 1 when the pre-synaptic inhibition turns off. We let  $V_{Th(M)}$  and  $V_T$  denote the activation thresholds for these two synapses.  $V_{Th(M)}$  is chosen such

that the time it takes for  $V_M$  to increase from  $V_M^*$  to  $V_{Th(M)}$  is some predetermined small time,  $T_C$ . Thus, we have:

$$\frac{ds_1}{dt} = \begin{cases} [1 - s_1]/\tau_{r1} & V_L \leq V_T \\ -s_1/\tau_{f1} & V_L > V_T \end{cases} \quad (3.28)$$

$$\epsilon \frac{ds_2}{dt} = \begin{cases} [1 - s_2]/\tau_{r2} & V_M \geq V_{Th(M)} \\ [s_{2min} - s_2]/\tau_{f2} & V_M < V_{Th(M)}. \end{cases} \quad (3.29)$$

That is, when  $V_M \geq V_{Th(M)}$ , the excitation from *MCN1* to *LG* is on ( $s_2$  increases to 1 with rate  $1/\epsilon\tau_{r2}$ ) but whether or not *LG* “feels” this excitation depends on whether or not the pre-synaptic inhibition from *LG* to the *MCN1* synapse is on. If  $V_L \leq V_T$ , the pre-synaptic inhibition turns off ( $s_1$  increases to 1 with rate  $1/\tau_{r1}$ ) but if  $V_L > V_T$ , the pre-synaptic inhibition turns on ( $s_1$  decreases to 0 with rate  $1/\tau_{f1}$ ) and blocks the excitation from *MCN1*. When *AB* inhibits *MCN1*,  $V_M$  goes below  $V_{Th(M)}$  and the excitation from *MCN1* to *LG* turns off ( $s_2$  decreases to  $s_{2min}$  with rate  $1/\epsilon\tau_{f2}$ ). The excitation from *MCN1* to *LG* is slow while the periodic inhibition of *MCN1* by *AB* is fast. Thus, the time constants  $\tau_{r1}$ ,  $\tau_{f1}$ ,  $\tau_{r2}$ ,  $\tau_{f2}$ , and  $\tau_M$  in (3.28), (3.29), and (3.26) are  $O(1)$  with respect to  $\epsilon$ .

As a simplification, we shall first consider the case when the synapse from *MCN1* to *LG* is not voltage dependent and when the electrical coupling between *MCN1* and *LG* is not present. We do this by letting  $s_\infty(V_L) \equiv 1$  and  $g_{elec}(V_L) \equiv 0$ . The voltage dependent excitation from *MCN1* to *LG* and the presence of electrical coupling between *MCN1* and *LG* will both be considered in Chapter 5. The voltage traces of *Int1* and *LG* computed with the reduced model are shown in Figure 3.5. It can be seen in this figure compared with Figure 3.2 that the reduced model simply

models the envelope of the *LG* and *Int1* activity and not the action potentials as the full model does.

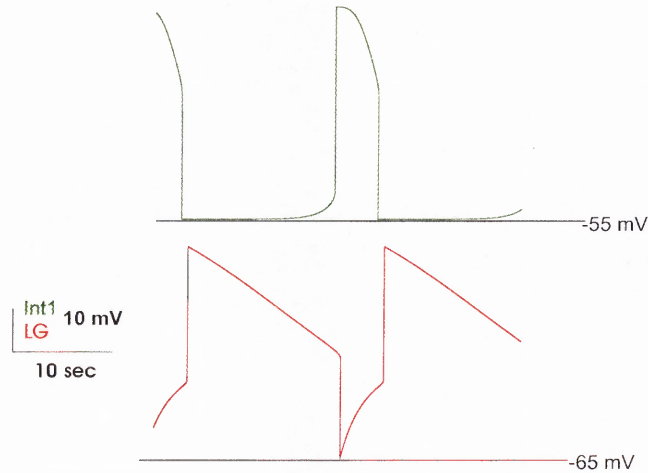


**Figure 3.5** Voltage traces of *LG* and *Int1* computed from simulation of the expanded, reduced model when the *AB* inputs to *MCN1* and *LG* are not present.

### 3.5 Geometric Singular Perturbation Theory and Phase Plane Analysis

To understand which parameters are important in controlling the gastric mill frequency, we use phase-plane analysis along with geometric singular perturbation theory to reduce the full flow to a study of flow on lower dimensional slow manifolds [47, 58]. The flow is the solution of the set of differential equations over all sets of initial conditions. From Equations (3.22)-(3.24) and (3.28)-(3.29), we see that  $V_L$ ,  $V_I$ ,  $V_M$ , and  $s_2$  evolve on a faster time scale than  $s_1$ . Considering the system of equations in the limit as  $\epsilon$  approaches 0, we obtain the slow time dynamic. Rescaling time by  $\zeta = t/\epsilon$ , we can obtain equations for which solutions evolve on the fast time scale.

Setting  $\epsilon = 0$  in the equations yields the slow equations:

$$0 = f(V_L, V_I, s), \quad (3.30)$$

$$0 = g(V_I, V_L, s_{AB \rightarrow I}), \quad (3.31)$$

$$0 = -g_{leak,M}[V_M - E_{leak,M}] - \bar{g}_{AB \rightarrow M} s_{AB \rightarrow M}(t)[V_M - E_{AB \rightarrow M}], \quad (3.32)$$

$$\frac{ds_1}{dt} = \begin{cases} [1 - s_1]/\tau_{r1} & V_L \leq V_T, \\ -s_1/\tau_{f1} & V_L > V_T, \end{cases} \quad (3.33)$$

$$0 = \begin{cases} [1 - s_2]/\tau_{r2} & V_M \geq V_{Th(M)}, \\ [s_{2min} - s_2]/\tau_{f2}(s_2) & V_M < V_{Th(M)}, \end{cases} \quad (3.34)$$

$$0 = [1 - s_{AB \rightarrow M}]/\tau_M, \quad V_{AB} \geq V_{Th(AB)}, \quad (3.35)$$

$$\frac{ds_{AB \rightarrow M}}{dt} = -s_{AB \rightarrow M}, \quad V_{AB} < V_{Th(AB)}.$$

$f(V_L, V_I, s)$  and  $g(V_I, V_L, s_{AB \rightarrow I})$  are the right-hand sides of Equations (3.22) and (3.23) (for  $\bar{g}_c = 0$ ), respectively. The set of points satisfying  $f(V_L, V_I, s) = 0$  and  $g(V_I, V_L, s_{AB \rightarrow I}) = 0$  are called the  $V_L$  and  $V_I$  nullclines, respectively. In slow time, Equations (3.30) and (3.31) imply that any trajectory is forced to lie on the  $V_L$  and  $V_I$  nullclines while  $s_1$  slowly evolves between 0 and 1 and  $s_2$  instantaneously jumps between  $s_{2min}$  and 1 whenever  $V_M$  crosses the threshold  $V_{Th(M)}$ . In slow time,  $s_{AB \rightarrow M}$  jumps to 1 whenever  $V_{AB}$  increases above  $V_{Th(AB)}$  and exponentially decays to 0 whenever  $V_{AB}$  decreases below  $V_{Th(AB)}$ .

Note that when  $\bar{g}_{AB \rightarrow M} = 0$ , then  $V_M$  is always greater than  $V_{Th(M)}$ , and we refer to *MCN1* as being tonically active. In this case,  $s_2 = 1$  for all time after some transient period. Alternatively, when  $\bar{g}_{AB \rightarrow M}$  is sufficiently large, then  $V_M$  goes above and below  $V_{Th(M)}$  in pyloric time and we say that *MCN1* is rhythmically active. In

this case,  $s_2$  jumps between  $s_{2min}$  and 1 each time  $V_M$  crosses  $V_{Th(M)}$ . We note that  $V_M$  may cross  $V_{Th(M)}$  several times before  $V_L$  crosses  $V_T$ .

To define fast equations, let  $\zeta = t/\epsilon$ . This implies:

$$\frac{dV}{dt} = \frac{dV}{d\zeta} \frac{d\zeta}{dt} = \frac{dV}{d\zeta} \frac{1}{\epsilon}. \quad (3.36)$$

Making this change of variables in equations (3.22)-(3.24) and (3.28)-(3.29) and then setting  $\epsilon = 0$  we obtain:

$$\frac{dV_L}{d\zeta} = f(V_L, V_I, s), \quad (3.37)$$

$$\frac{dV_I}{d\zeta} = g(V_I, V_L, s_{AB \rightarrow I}), \quad (3.38)$$

$$\frac{dV_M}{d\zeta} = 0, \quad (3.39)$$

$$\frac{ds_1}{d\zeta} = 0, \quad (3.40)$$

$$\frac{ds_2}{d\zeta} = \begin{cases} [1 - s_2]/\tau_{r2} & V_M \geq V_{Th(M)}, \\ [s_{2min} - s_2]/\tau_{f2}(s_2) & V_M < V_{Th(M)}, \end{cases} \quad (3.41)$$

$$\frac{ds_{AB \rightarrow M}}{dt} = \begin{cases} [1 - s_{AB \rightarrow M}]/\tau_M & V_{AB} \geq V_{Th(AB)} \\ 0 & V_{AB} < V_{Th(AB)}. \end{cases} \quad (3.42)$$

Therefore, in fast time  $V_L$  and  $V_I$  evolve according to the dynamics of  $f(V_L, V_I, s)$  and  $g(V_I, V_L, s_{AB \rightarrow I})$  and  $s_2$  increases and decreases between 1 and  $s_{2min}$  while  $s_1$  remains constant. This fixed value that  $s_1$  remains at is the value of  $s_1$  when the transition from slow time to fast time occurs. These equations govern transitions between the different branches of the  $V_I$  and  $V_L$  nullclines.

We find the explicit equations for the nullclines by solving (3.30) for  $V_L$  and (3.31) for  $V_I$  to find that

$$V_L = F(V_I, s) = \frac{g_{leak,L} E_{leak,L} + g_{I \rightarrow L} n_\infty(V_I) E_{I \rightarrow L} + \bar{g}_s s E_{exc}}{g_{leak,L} + g_{L \rightarrow I} n_\infty(V_I) + \bar{g}_s s} \quad (3.43)$$

and

$$V_I = G(V_L, s_{AB \rightarrow I}) = \frac{g_{leak,I} E_{leak,I} + g_{L \rightarrow I} n_\infty(V_L) E_{L \rightarrow I} + \bar{g}_{AB \rightarrow I} s_{AB \rightarrow I}(t) E_{AB \rightarrow I}}{g_{leak,I} + g_{L \rightarrow I} n_\infty(V_L) + \bar{g}_{AB \rightarrow I} s_{AB \rightarrow I}(t)}. \quad (3.44)$$

A simultaneous solution to (3.30) and (3.31) can be found graphically by plotting  $F(V_I, s)$  versus  $G(V_L, s_{AB \rightarrow I})$ . An intersection of these two nullclines corresponds to a fixed point of the fast equations. The intersection points represent the steady state solutions of  $V_L$  and  $V_I$  for a fixed value of  $s$ . The position of the nullclines in  $V_I - V_L$  phase space changes as a function of  $s$  (see Figure 3.6) and  $s_{AB \rightarrow I}$ . In general, increases (decreases) in  $s$  move the  $V_L$  nullcline to the right (left), either in slow time due to changes in  $s_1$  or in fast time due to changes in  $s_2$ .

The  $V_I$  nullcline has two possible positions in phase space depending on whether  $s_{AB \rightarrow I} = 0$  or 1. The nullcline corresponding to  $s_{AB \rightarrow I} = 1$  is lower in phase space than the one for  $s_{AB \rightarrow I} = 0$ . We note that the left branch of the  $V_I$  nullcline shifts down much more than the right branch since on the right branch  $V_I$  is already close to  $E_{AB \rightarrow I}$  independent of  $s_{AB \rightarrow I}(t)$ ; see Figure 3.7.

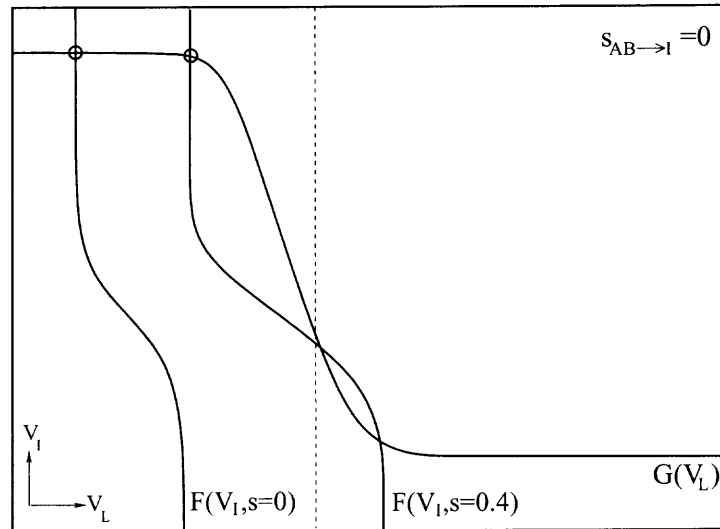


**Figure 3.6** The  $V_L$  and  $V_I$  nullclines plotted in phase space for two different values of  $s(t)$  for  $s_{AB \rightarrow I} = 0$ . The  $V_L$  nullcline is labeled  $F$  and the  $V_I$  nullcline is labeled  $G$ . When  $s = 0$ , the  $V_L$  nullcline is to the far left. As  $s$  increases, the  $V_L$  nullcline shifts to the right.

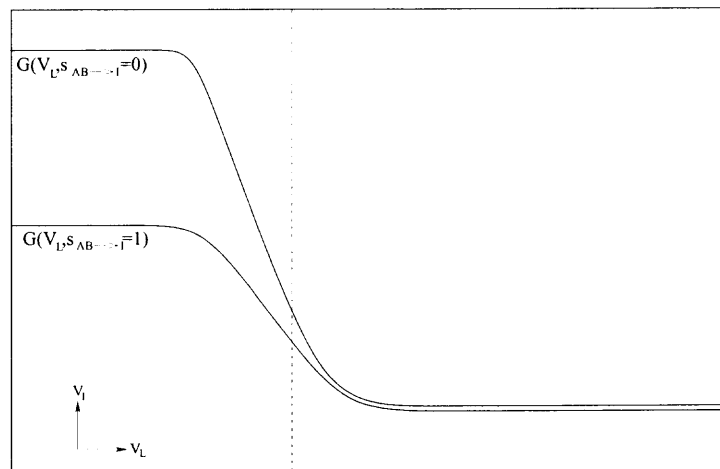


**Figure 3.7** The  $V_I$  nullcline is shifted upward when  $s_{AB \rightarrow I} = 0$  and is shifted downward when  $s_{AB \rightarrow I} = 1$ .

The number and stability of fixed points also changes as a function of  $s$  and  $s_{AB \rightarrow I}$ . When the intersection of the  $V_L$  and  $V_I$  nullclines occurs on their left branches, the fixed point is stable. When the intersection occurs on the right branches of the nullclines, the fixed point is also stable. However, when the intersection occurs on the middle branches of both the  $V_L$  and  $V_I$  nullclines, the fixed point is unstable. The stability of the fixed points can be determined by calculating the eigenvalues of the Jacobian matrix. This calculation is given in Appendix C. Furthermore, when the trajectory lies at a stable fixed point on the left branches of the nullclines,  $V_L < V_T$  and, therefore,  $s_1$  increases with rate  $1/\tau_{r1}$ . When the trajectory lies at a stable fixed point on the right branches of the nullclines,  $V_L > V_T$ , therefore, causing  $s_1$  to decrease with rate  $1/\tau_{f1}$ ; see Figure 3.8.

We identify four important values of  $(s, s_{AB \rightarrow I})$  as  $(s_L^{off}, 0)$ ,  $(s_L^{on}, 1)$ ,  $(s_R^{off}, 0)$  and  $(s_R^{on}, 1)$ ; see Figure 3.9. These points correspond to values when the two nullclines intersect tangentially resulting in the loss (or gain) of two fixed points through a saddle-node bifurcation. Because  $s_1$  is increasing on the left branches and decreasing on the right, the ordering of these bifurcation points is  $s_R^{on} < s_R^{off} < s_L^{on} < s_L^{off}$ . These values can be calculated analytically; see Appendix D.

On the slow time scale, the solution trajectory must lie at the intersection of the  $V_I$  and  $V_L$  nullclines, i.e., at a fixed point. Thus to understand the evolution of trajectories in the  $V_I - V_L$  phase space, we need to understand how the position of fixed points change as a function of  $s$  and  $s_{AB \rightarrow I}$ .

Let us first consider the case when  $s_{AB \rightarrow M}(t) \equiv 0$ . Then  $MCN1$  is tonically active and sits at a value of  $E_{leak,M}$ .  $E_{leak,M}$  is chosen to be larger than  $V_{Th(M)}$  which we see from (3.34) allows  $s_2 = 1$ . As a result, we have  $s(t) = s_1(t) * 1$  which means that  $s(t)$  increases towards 1 with time constant  $1/\tau_{r1}$  when  $V_L < V_T$  and decreases towards 0 with time constant  $1/\tau_{f1}$  when  $V_L > V_T$ ; see Figure 3.10(A.). In addition, the  $V_I$  nullcline is fixed in its upward position.

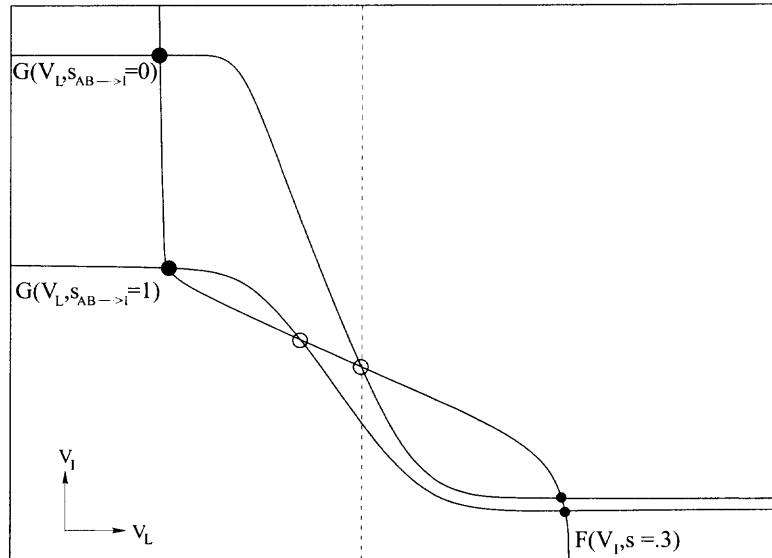


**Figure 3.8** The  $V_L$  nullcline is plotted for  $s = .3$  and the  $V_I$  nullcline is plotted for  $s_{AB \rightarrow I}(t) = 0$  and  $s_{AB \rightarrow I}(t) = 1$ . At the intersection of the nullclines on either the left or right branches of the nullclines, the fixed point (shown by  $\bullet$ ) is stable. When the intersection of the nullclines is on the middle branches of the nullclines, the fixed point (shown by  $\circ$ ) is unstable. When the solution trajectory lies at a stable fixed point on the left branches,  $V_L < V_T$ . Thus, by Equation (3.33),  $s_1$  increases. When the solution trajectory lies at a stable fixed point on the right branches,  $V_L > V_T$ . Now, by Equation (3.33),  $s_1$  decreases. Whether or not the trajectory lies at the stable fixed point on either the left or right branches is determined by the value of  $s$ . The dashed line indicates where  $V_L = V_T$ .

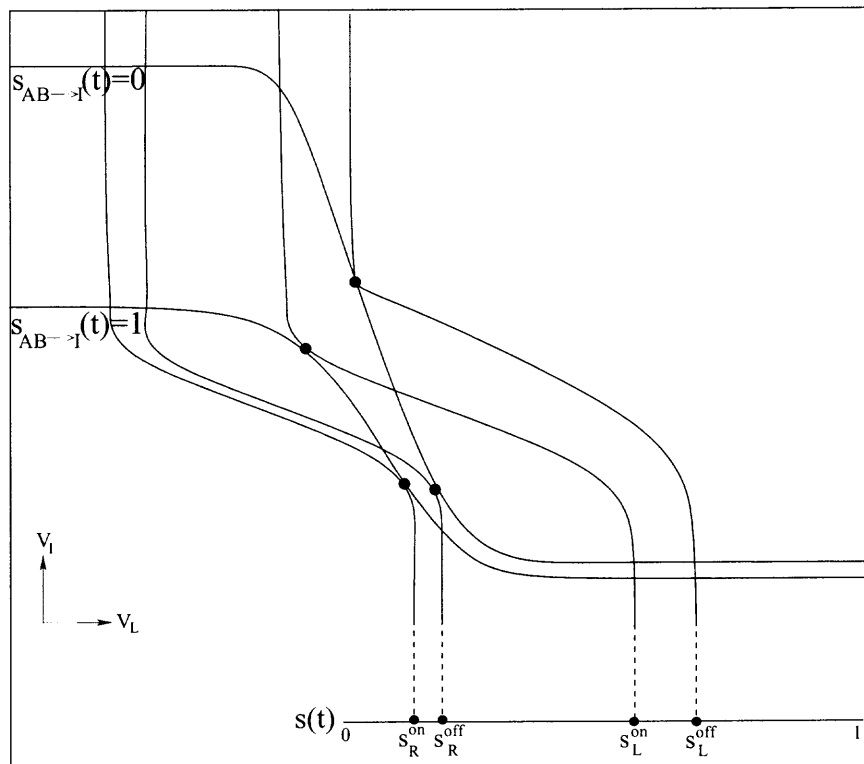


**Figure 3.9** Position of the  $V_L$  and  $V_I$  nullclines for  $(s, s_{AB \rightarrow I}) = (s_R^{on}, 1), (s_R^{off}, 0), (s_L^{on}, 1),$  and  $(s_L^{off}, 0)$ . At these four points, the nullclines intersect tangentially, resulting in the loss (or gain) of two fixed points through a saddle-node bifurcation.

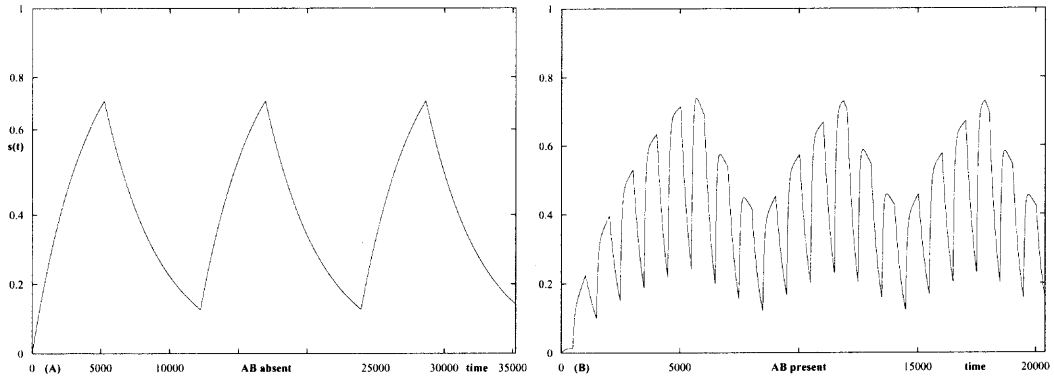


**Figure 3.10** (A.)  $s$  versus time for the case when the *MCN1* to *LG* excitation is constant ( $s_2 = 1$ ).  $s$  increases to 1 with rate  $1/\tau_{r1}$  when  $V_L \leq V_T$  and  $s$  decreases to 0 with rate  $1/\tau_{f1}$  when  $V_L > V_T$ . (B.)  $s$  versus time for the case when the *MCN1* to *LG* excitation is rhythmic. When  $V_L \leq V_T$ ,  $s_1$  increases to 1 with rate  $1/\tau_{r1}$  and  $s_2$  jumps between 1 and  $s_{2min}$  when  $s_{AB \rightarrow M}(t)$  changes between 0 and 1. When  $V_L > V_T$ ,  $s_1$  decreases to 0 with rate  $1/\tau_{f1}$  and  $s_2$  jumps between 1 and  $s_{2min}$  when  $s_{AB \rightarrow M}(t)$  changes between 0 and 1.

From (3.43), we see that as  $s$  slowly increases, the  $V_L$  nullcline slowly shifts to the right, thus causing the position of the stable fixed point to shift to the right. This continues until the  $V_L$  nullcline shifts far enough to the right so that the stable fixed point on the left branches of the nullclines is lost through a saddle-node bifurcation when  $s = s_L^{off}$ . Once the fixed point is lost, the trajectory is forced to jump on the fast time scale (Equations (3.37)-(3.38)) to the only remaining stable fixed point which is on the right branches of the nullclines. This jump pushes  $V_L$  above  $V_T$  causing  $s(t)$  to begin to decrease. When  $s$  decreases, the  $V_L$  nullcline slowly shifts to the left until the stable fixed point on the right branches of the  $V_L$  and  $V_I$  nullclines similarly undergoes a saddle-node bifurcation at  $s = s_R^{off}$ . The trajectory then makes a jump in fast time back to the left branches of the nullclines which forces  $V_L$  below  $V_T$ . Figure 3.11 shows the  $V_L$  and  $V_I$  nullclines for different values of  $s(t)$  when  $s_{AB \rightarrow I}(t) \equiv 0$ . Similar dynamics occur when  $s_{AB \rightarrow I}(t) \equiv 1$  except now the trajectory passes through the bifurcation points  $s_L^{on}$  and  $s_R^{on}$  during its transition between left and right branches.

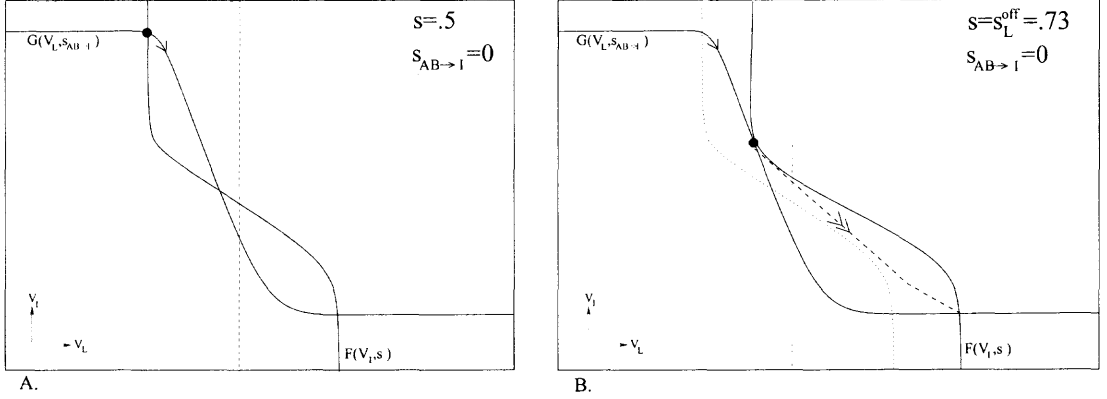


**Figure 3.11**  $V_L$  and  $V_I$  nullclines for different values of  $s$  when  $s_{AB \rightarrow I}(t) = 0$ . (A.)  $s = 0.5$  and the trajectory lies at the fixed point on the left branches of the  $V_L$  and  $V_I$  nullclines. At the fixed point,  $V_L < V_T$  so  $s$  increases. (B.)  $s$  reaches  $s_L^{off}$  and the fixed point undergoes a saddle-node bifurcation at  $\bullet$ . The trajectory is therefore, forced to jump to the stable fixed point on the right branches of the nullclines where  $V_L > V_T$ .

When the *MCN1* excitation to *LG* is rhythmic instead of tonic,  $s_2$  changes on the fast timescale between 1 and  $s_{2min}$  as  $V_M$  crosses over  $V_{Th(M)}$  while  $s_1$  increases towards 1 when  $V_L < V_T$  and decreases towards 0 when  $V_L > V_T$  on the slow timescale. This causes  $s(t)$  to generally have a shape as shown in figure 3.10(B.). Notice that the envelope of  $s(t)$  activity is the same as in the tonic excitability case seen in figure 3.10(A.), but now there are rapid changes in  $s(t)$  due to the rapid changes in  $s_2(t)$ . The jump of  $s_2$  between  $s_{2min}$  and 1 causes the  $V_L$  nullcline to instantaneously jump to the right when  $s_2$  jumps to 1 and instantaneously jump to the left when  $s_2$  jumps to  $s_{2min}$ . The distance of these jumps of the  $V_L$  nullcline, calculated from (3.43), is  $F(V_I, s_1 * 1) - F(V_I, s_1 * s_{2min})$ .

Note that in the *MCN1* rhythmic case, fixed points can be lost in two different ways. They may be lost as before through a saddle node bifurcation as  $s$  is slowly changing due to changes in  $s_1$ ; Figure 3.12(A.). Or they may be lost when  $s_2$  changes on the fast time scale. For example, on the left branches, it may be that  $s_1 * s_{2min} < s_L^{off}$ , but  $s_1 * 1 > s_L^{off}$ . In this case, the fixed point would be instantaneously lost if

$s_{2min}$  jumped to 1 due to a change in *MCN1* activity; see Figure 3.12(B.). On the right branches, it may be that  $s_1 * 1 > s_R^{off}$ , but  $s_1 * s_{2min} < s_R^{off}$ . In this case, the fixed point would be lost when  $s_2$  jumped from 1 to  $s_{2min}$ .

In the case where  $s_{AB \rightarrow I}(t)$  is a square wave, the trajectory will always lie on a nullcline with either  $s_{AB \rightarrow I} = 0$  or  $s_{AB \rightarrow I} = 1$ . Now fixed points can be lost in three different ways when *MCN1* is rhythmic. Consider the left branches. As before, a fixed point can be lost as  $s$  increases slowly through a bifurcation point or instantaneously as  $s_2$  changes from  $s_{2min}$  to 1. The third way it can be lost is if  $s_L^{off} > s > s_L^{on}$  and  $s_{AB \rightarrow I}$  switches from 0 to 1; see Figure 3.12(C.).

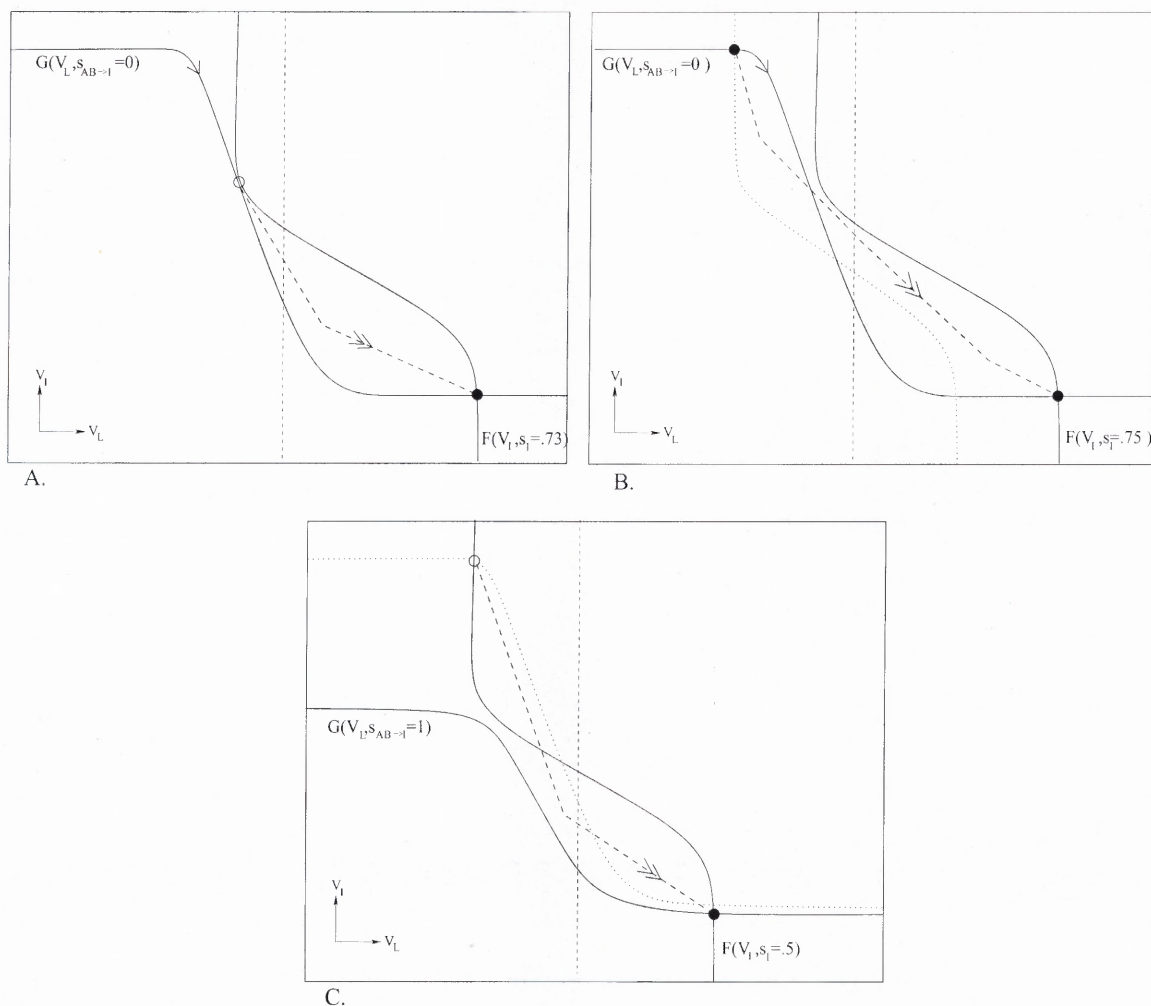


**Figure 3.12** When *MCN1* is rhythmic and the *AB* input to *Int1* is absent, fixed points can be lost in two ways: through a saddle-node bifurcation as  $s$  slowly changes due to  $s_1$  or when  $s_2$  changes on the fast timescale. (A.) On the left branches of the nullclines,  $s_2 = 1$  and  $s_1$  moves the  $V_L$  nullcline to the right resulting in a saddle-node bifurcation of the fixed point at  $\circ$  once  $s = s_L^{off}$ . The trajectory is forced to jump to the stable fixed point on the right branches of the nullclines (shown by  $\bullet$ ). This can also occur when  $s_{AB \rightarrow I} = 1$  and  $s_1$  reaches  $s_L^{on}$ . (B.) When  $s_2$  jumps from  $s_{2min}$  to 1, the fixed point on the left branches of the nullclines is instantaneously lost because  $s > s_L^{off}$  and the trajectory will jump to the fixed point on the right branches of the nullclines (shown by  $\bullet$ ). This can also occur when  $s_{AB \rightarrow I} = 1$  and  $s_2$  jumps to 1 when  $s > s_L^{on}$ . (C.) The fixed point can be lost in a third way when *MCN1* is rhythmic and the *AB* input to *Int1* is present. While  $s_2 = 1$  and  $s_{AB \rightarrow I}(t)$  jumps from 0 to 1, the fixed point on the left branches of the nullclines (shown by  $\circ$ ) is instantaneously lost because  $s > s_L^{on}$  and the solution trajectory is forced to jump to the fixed point on the right branches of the nullclines ( $\bullet$ ).

## CHAPTER 4

### EXISTENCE AND STABILITY OF PERIODIC SOLUTIONS AND THE CALCULATION OF FREQUENCY

To understand how the two different inputs of  $AB$  and  $MCN1$  affect the gastric mill frequency, we shall consider four different cases (see Figure 1.9):

**Case 1.** Tonic  $MCN1$  excitation without  $AB$  input to  $Int1$

**Case 2.** Tonic  $MCN1$  excitation with  $AB$  input to  $Int1$

**Case 3.** Rhythmic  $MCN1$  excitation without  $AB$  input to  $Int1$

**Case 4.** Rhythmic  $MCN1$  excitation with  $AB$  input to  $Int1$

In each case, we shall prove the existence, local uniqueness, and stability of a particular periodic solution and then calculate the period of this solution. The proofs of existence, local uniqueness and stability of periodic solutions exploit the different time scales present in the system of equations. In Cases 2 through 4, this will reduce to finding fixed points of appropriate 1-dimensional maps. In the proofs, we construct singular periodic solutions which are valid at  $\epsilon = 0$ . However, there is no difficulty in extending their existence, local uniqueness and stability to the  $\epsilon$  sufficiently small case using the work of Mischenko and Rozov [47].

The main emphasis of this work is to show that the period of the solution in Cases 3 and 4 can be identical if the value of  $m$ , representing the time mismatch of  $AB$  and  $MCN1$  input to the gastric mill network, is chosen in an appropriate range. When  $m$  is chosen outside of this range, then the periods will differ.

#### 4.1 Case 1: Tonic *MCN1* Excitation without *AB* input to *Int1*

In Case 1, the input from *AB* to *Int1* and from *AB* to *MCN1* is removed. Thus, the only source of input to the gastric mill is the tonic excitation from *MCN1*. The antiphase oscillations of the gastric mill rhythm can be understood by examining the position of the nullclines and, thus, the behavior of the solution trajectory in phase space. Before considering the effect of *MCN1* on the gastric mill rhythm, it is useful to consider the dynamics of the gastric mill network without input from *MCN1* and *AB*. *Int1* is modeled as having a suprathreshold resting potential and *LG* is modeled as having a subthreshold resting potential. Therefore, without external input, the reciprocal inhibition between *LG* and *Int1* causes *LG* to be further suppressed by *Int1* and there are no antiphase oscillations of *LG* and *Int1*. In the absence of *MCN1* and *AB* input, we set  $\bar{g}_{AB \rightarrow I} = 0$  and  $\bar{g}_s = 0$  in Equations (3.22) and (3.23). Therefore, the solution trajectory is stuck at the stable fixed point on the left branches of the nullclines where  $V_L$  is low and  $V_I$  is high. When the tonic input from *MCN1* is added, we remove the restriction that  $\bar{g}_s = 0$  in Equation (3.22) and we set  $\bar{g}_{AB \rightarrow M} = 0$  in Equation (3.24). When  $\bar{g}_{AB \rightarrow M} = 0$ ,  $V_M > V_{Th(M)}$  for all  $t$  and *MCN1* is tonically active. This allows us to set  $s_2 = 1$  so that  $s = s_1 * s_2$  will only follow the dynamics of  $s_1$ .

Suppose that initially, the fixed point lies on the left branches of the nullclines (*LG* is in its interburst phase). Here,  $V_L < V_T$  which causes  $s_1$  to increase. The increase in  $s_1$  pushes the  $V_L$  nullcline, and consequently, the position of the stable fixed point to the right. Eventually,  $s_1$  increases sufficiently so that the fixed point undergoes a saddle-node bifurcation when  $s = s_L^{off}$ . This forces the trajectory to jump to the stable fixed point, now on the right branches of the nullclines. Here,  $V_L > V_T$  (*LG* enters its burst phase) so  $s_1$  begins to slowly decrease. As  $s_1$  decreases, the  $V_L$  nullcline, and consequently, the position of the stable fixed point on the right branches of the nullclines slowly shifts to the left. This continues until the saddle-node

bifurcation occurs when  $s = s_R^{off}$  and the solution trajectory returns to the left branches of the nullclines ( $LG$  re-enters its interburst phase). Here, the process repeats.

In Case 1, the only way a fast transition between branches can occur is by  $s_1$  passing through the bifurcation points  $s_L^{off}$  or  $s_R^{off}$ . To construct a periodic solution, let  $s_1(0) = s_R^{off}$  such that the trajectory at  $t = 0^-$  is at the bifurcation point on the right branches at the intersection of the  $V_I$  and  $V_L$  nullclines. At  $t = 0^+$ , the trajectory jumps back to the left branches at the intersection of the nullclines; see Figure 4.1(A.). On these branches,  $V_L < V_T$  and thus  $s_1$  will increase until it reaches the bifurcation point  $s_L^{off}$  at  $t = T_1$ ; see Figure 4.1(B.)-(C.). Once  $s$  reaches  $s_L^{off}$ , the trajectory will jump back to the right branch and since  $V_L > V_T$ ,  $s_1$  will now decrease until it comes back to  $s_R^{off}$  at  $t = T_2$ ; see Figure 4.1(D.). Thus the value of  $s_1$  will have returned to its original value at time  $T_2$ . Since all the fast variables are slaved through Equations (3.30) and (3.31) to the behavior of  $s_1$ , we do not explicitly need to check their evolution during the time interval  $[0, T_2]$ . In this sense, proving the existence of this periodic solution has been reduced to proving that the single variable  $s_1$  is periodic. Thus it is seen that there exists a singular periodic solution whose period is  $T_2$ . In section 4.5, the value of  $T_2$  is calculated both analytically and numerically. It is clear, however, that the period in Case 1 is determined by the rate at which  $s_1$  increases and the rate at which it decreases.

The solution is unique and stable since if  $s_1(0) > s_R^{off}$  and the trajectory is on the right branches of the nullclines, for example, then the solution can be flowed forward a time  $\hat{t}$  such that  $s_1(\hat{t}) = s_R^{off}$ . From here the solution trajectory would follow the dynamics described above and return to  $s_R^{off}$  at time  $t = T_2 + \hat{t}$ . Thus, by flowing backwards in time, it is seen that  $s_1(T_2) = s_1(0)$ .

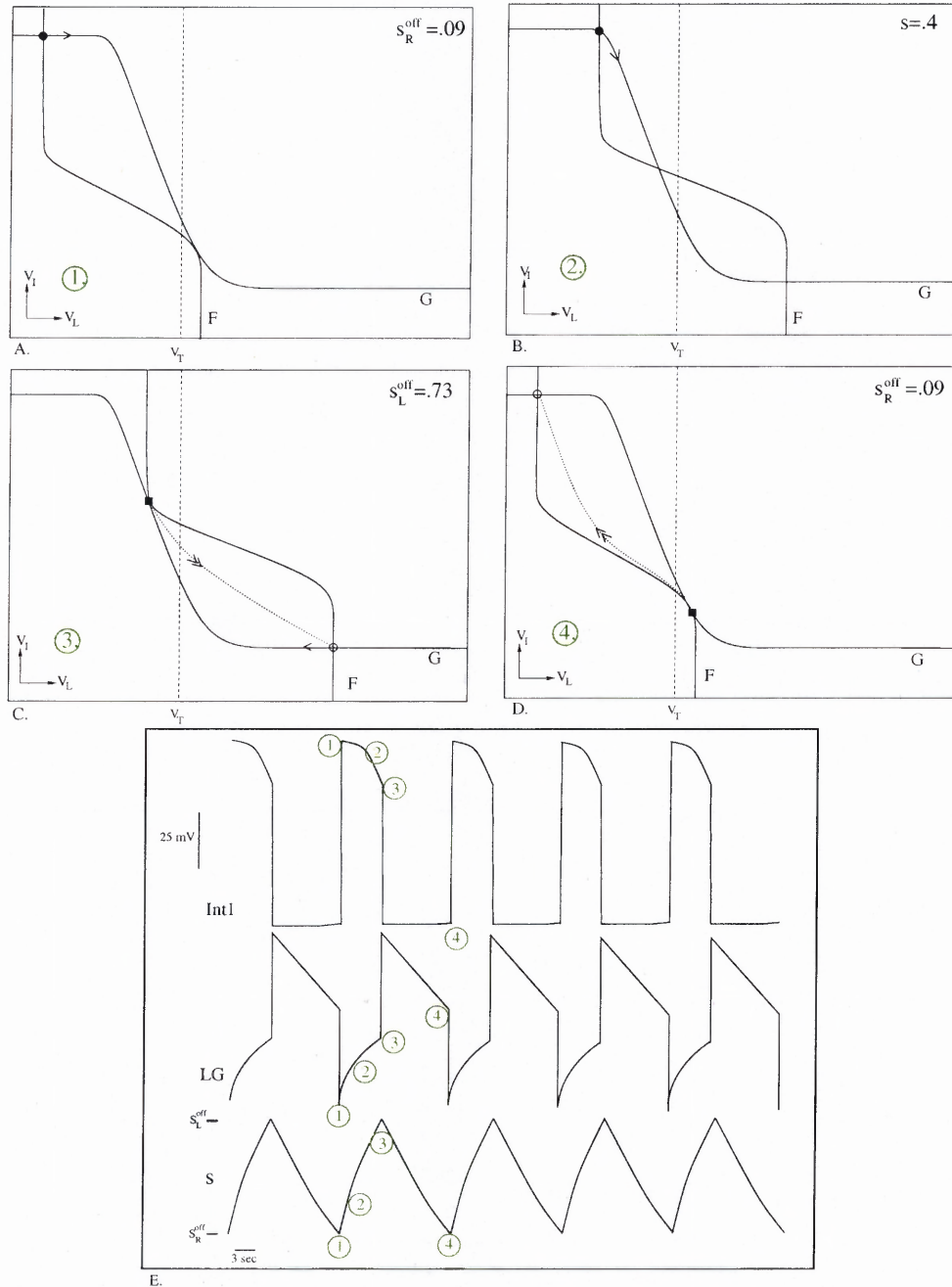


**Figure 4.1** Plots of the  $V_I$  (G) and  $V_L$  (F) nullclines for different values of  $s$  in Case 1. • marks the position of the trajectory at a stable fixed point and ◦ marks the point to which the trajectory will jump when the stable fixed point bifurcates. (A.)  $s = s_R^{off}$  and the trajectory is forced to lie at the fixed point on the left branches of the nullclines. (B.) At the fixed point on the left branches,  $V_L < V_T$  which forces  $s$  to increase towards 1. (C.)  $s$  continues to increase until it reaches the value  $s_L^{off}$  at which the stable fixed point on the left branches of the nullclines undergoes a saddle-node bifurcation. The trajectory is, therefore, forced to jump to the fixed point on the right branches of the nullclines. This jump causes  $s$  to cross above  $V_T$  so that  $s$  begins to decrease. (D.)  $s$  decreases to  $s = s_R^{off} =$  at which the fixed point on the right branches is again lost and the trajectory returns to the upper left branches of the nullclines. Therefore, the solution trajectory lies on a periodic orbit. (E.) The voltage traces of  $LG$  and  $Int1$  as  $s$  changes between  $s_L^{off}$  and  $s_R^{off}$ .

#### 4.2 Case 2: Tonic MCN1 Excitation with AB Input to Int1

We examine the effect of  $AB$  on the gastric mill rhythm by first considering the inhibitory synapse from  $AB$  to  $Int1$ . In this case,  $\bar{g}_{AB \rightarrow M} = 0$  so that  $s_2 \equiv 1$  and, therefore, the  $MCN1$  to  $LG$  excitation is tonic. Now the  $AB$  to  $Int1$  inhibition is present ( $\bar{g}_{AB \rightarrow I} > 0$ ). Without loss of generality, let  $m = 0$  in (3.23). Hence,  $s$  causes the  $V_L$  nullcline to slowly shift to the right and left as in Case 1 and  $s_{AB \rightarrow I}(t)$  causes the  $V_I$  nullcline to instantaneously jump down when  $s_{AB \rightarrow I}(t)$  goes to 1 and to jump back up when  $s_{AB \rightarrow I}(t)$  returns to 0; see Figure 4.2.

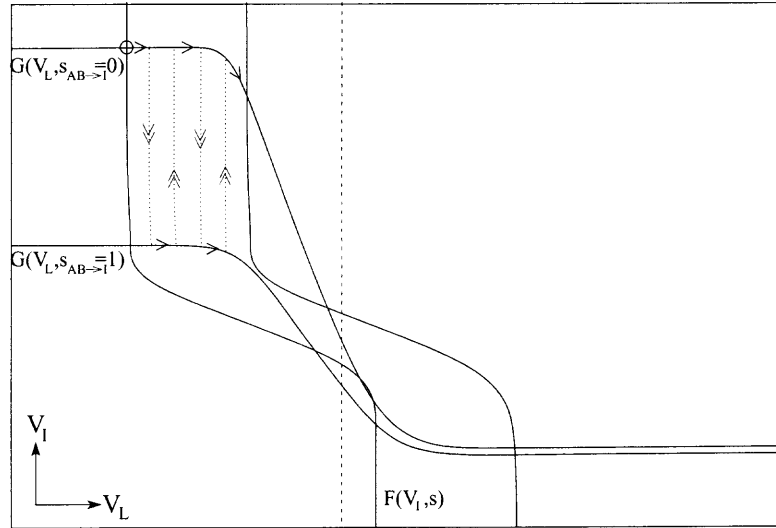


**Figure 4.2** In Case 2, when the stable fixed point occurs on the left branches of the nullclines,  $s(t)$  slowly increases and, thereby, slowly pushes the  $V_L$  nullcline to the right while the  $V_I$  nullcline jumps up and down each time  $s_{AB \rightarrow I}$  jumps between 0 and 1. The dotted line indicates the movement of the trajectory as the  $V_I$  nullcline shifts up and down and  $s(t)$  increases.

To understand the control of frequency in Case 2, we must again consider the nullclines in the phase-plane. When  $V_L < V_T$ , the  $V_L$  nullcline moves to the right slowly because  $\tau_{r1}$  is large. The  $AB$  input to  $Int1$ , on the other hand, is fast and periodic so that the  $V_I$  nullcline shifts up and down repeatedly and instantaneously compared with the shift of the  $V_L$  nullcline. If the solution trajectory initially lies at a fixed point on left branches of the nullclines,  $s_1$  will slowly increase and the  $V_L$

nullcline will shift to the right. Hence, the value of  $V_L$  will slowly increase and the value of  $V_I$  will slowly decrease. Then, at a time when  $s_{AB \rightarrow I}(t)$  jumps from 0 to 1, the  $V_I$  nullcline will instantaneously shift downward and the solution trajectory will be forced to the new stable fixed point on the left branches. At this new fixed point, however, the value of  $V_I$  is significantly lower than the value of  $V_I$  when the  $V_I$  nullcline is shifted upward. When  $s_{AB \rightarrow I}(t)$  returns to 0, the  $V_I$  nullcline will jump back to its upward position and the solution trajectory will return to the stable fixed point on the left branches of the nullclines where the voltage of  $V_I$  is high. Thus, each time  $s_{AB \rightarrow I}(t)$  jumps between 0 and 1 the voltage of  $Int1$  sharply decreases. This is representative of the fact that at each time  $s_{AB \rightarrow I}(t) = 1$ ,  $Int1$  is inhibited by  $AB$ .

#### 4.2.1 Possible Solution Trajectories for Case 2

On the left branches of the nullclines, three cases arise for the loss of the fixed point. The first possibility is that while  $s_L^{on} < s < s_L^{off}$  for  $s_{AB \rightarrow I}(t) = 0$ , when  $s_{AB \rightarrow I}(t) \rightarrow 1$ , the  $V_I$  nullcline jumps down causing the stable fixed point to be immediately lost. This forces the trajectory to jump directly to the only remaining stable fixed point on the right branches of the  $V_I$  and  $V_L$  nullclines; see Figure 4.3(A.).

The second possibility is that on one of the jump downs of the  $V_I$  nullcline, the trajectory jumps to the stable fixed point still on the left branches of the  $V_I$  and  $V_L$  nullclines and then while  $s_{AB \rightarrow I}(t)$  is still equal to 1,  $s$  continues to increase until the fixed point is lost through the saddle-node bifurcation at  $s = s_L^{on}$ ; see Figure 4.3(B.). The third possible way for the fixed point on the left branches to be lost is as in Case 1. That is, while  $s_{AB \rightarrow I} = 0$ ,  $s$  increases to  $s_L^{off}$ ; see Figure 4.1(C.).

On the right branches of the nullclines, three similar cases arise for the loss of the fixed point. The first possibility is that while  $s_R^{on} < s < s_R^{off}$  for  $s_{AB \rightarrow I}(t) = 1$ , when  $s_{AB \rightarrow I}(t) \rightarrow 0$ , the  $V_I$  nullcline jumps up causing the stable fixed point to be

immediately lost. This forces the trajectory to jump directly to the stable fixed point on the left branches of the  $V_I$  and  $V_L$  nullclines; see Figure 4.3(C.).

The second possibility is that on one of the jump downs of the  $V_I$  nullcline, the trajectory jumps to the stable fixed point still on the right branches of the  $V_I$  and  $V_L$  nullclines and then while  $s_{AB \rightarrow I}(t)$  is still equal to 1,  $s$  continues to decrease until the fixed point is lost through the saddle-node bifurcation at  $s = s_R^{on}$ ; see Figure 4.3(D.). The third possible way for the fixed point on the right branches to be lost is as in Case 1. That is, while  $s_{AB \rightarrow I} = 0$ ,  $s$  decreases to  $s_R^{off}$ ; see Figure 4.1(D.).

Which of the above cases occurs depends upon the amount of time that  $s_{AB \rightarrow I}(t)$  spends in its active and inactive phases, the rates at which  $s_1$  increases and decreases, and the timing of the  $AB$  input to  $Int1$ . In other words, the timing of the periodic jumps in  $s_{AB \rightarrow I}$  affects the timing of the shifts in the  $V_I$  nullcline which in turn determines which case occurs. We note that the downward shift of the  $V_I$  nullcline due to  $s_{AB \rightarrow I}(t)$  jumping from 0 to 1 is much more significant on its left branch than on its right. Thus,  $s_L^{on}$  is significantly smaller than  $s_L^{off}$ .

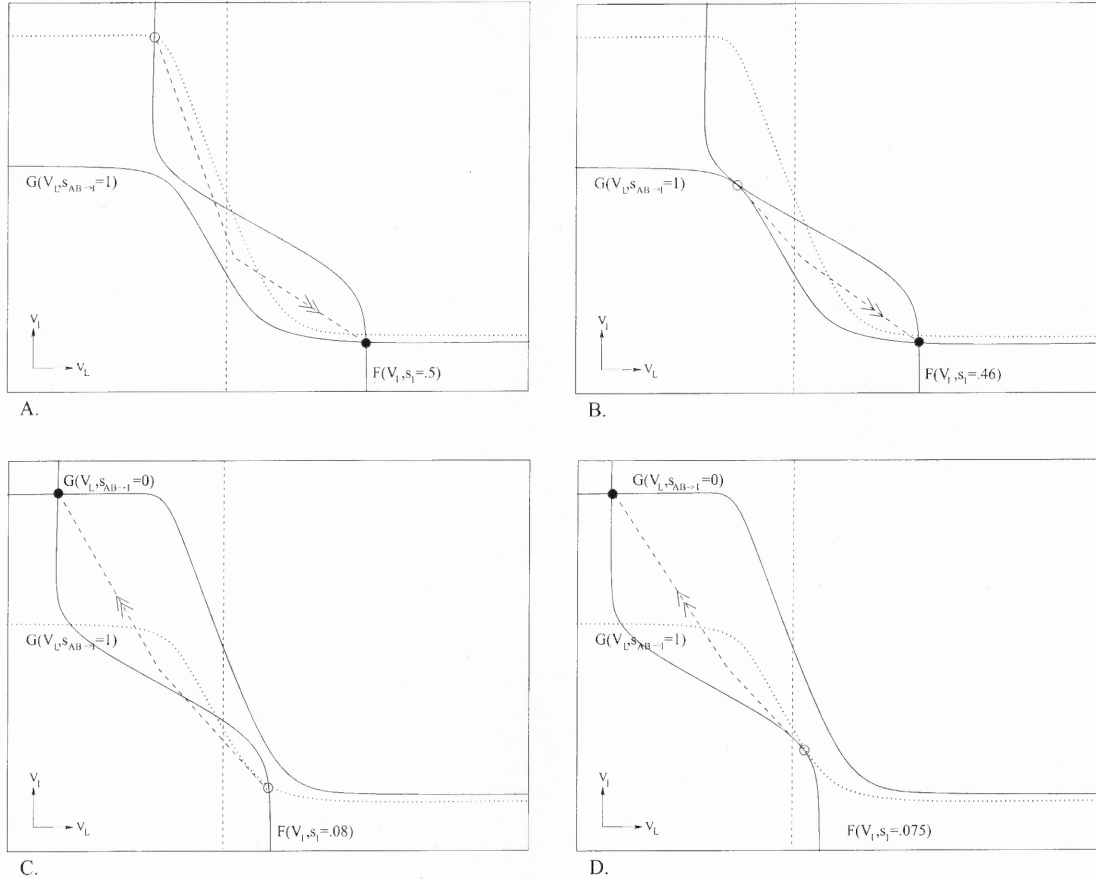


**Figure 4.3** For *MCN1* tonic and the *AB* input to *Int1* present, fixed points can be lost in multiple ways. (A.) On the left branches of the nullclines, while  $s_L^{on} < s < s_L^{off}$  for  $s_{AB \rightarrow I}(t) = 0$ , when  $s_{AB \rightarrow I}(t) \rightarrow 1$ , the  $V_I$  nullcline jumps down causing the stable fixed point (shown by  $\circ$ ) to be immediately lost. This forces the trajectory to jump directly to the stable fixed point (shown by  $\bullet$ ) on the right branches of the  $V_I$  and  $V_L$  nullclines. (B.) A second possible way the fixed point can be lost on the left branches of the nullclines for *MCN1* tonic is if on the jump down of the  $V_I$  nullcline, the trajectory jumps to the stable fixed point still on the left branches of the  $V_I$  and  $V_L$  nullclines and then while  $s_{AB \rightarrow I}(t)$  is still equal to 1,  $s$  continues to increase until the fixed point is lost through the saddle-node bifurcation at  $s = s_L^{on}$ . (C.) On the right branches of the nullclines for *MCN1* tonic, when  $s_{AB \rightarrow I}$  jumps from 1 to 0, the fixed point is instantaneously lost because  $s_R^{on} < s < s_R^{off}$  and the solution trajectory must jump to the fixed point on the left branches of the nullclines ( $\bullet$ ). (D.) A second possible way the fixed point can be lost on the right branches of the nullclines for *MCN1* tonic is if on one of the jump downs of the  $V_I$  nullcline, the trajectory jumps to the stable fixed point still on the right branches of the  $V_I$  and  $V_L$  nullclines. Then while  $s_{AB \rightarrow I}(t)$  is still equal to 1,  $s$  continues to decrease until the fixed point is lost through the saddle-node bifurcation at  $s = s_R^{on}$ .

### 4.2.2 Construction of Periodic Solution for Case 2

Recall that the pyloric period is much shorter than the gastric mill period. Thus, while  $LG$  is inactive ( $V_L < V_T$ ),  $s_{AB \rightarrow I}$  oscillates several times between 0 and 1. The exact number of times depends on the time constant  $\tau_{r1}$ . Similarly when  $LG$  is active ( $V_L > V_T$ ), the number of oscillations of  $s_{AB \rightarrow I}$  depends on the time constant  $\tau_{f1}$ . This implies that the periodic solution in Case 2 depends on the relationship between  $\tau_{r1}$ ,  $\tau_{f1}$  and the pyloric input frequency of  $AB$ . More specifically, let us say that a periodic solution obeys Property A if the associated trajectory jumps from the right to left branches when  $s_{AB \rightarrow I}(t)$  switches from 1 to 0 and from left to right branches through the bifurcation point  $s_L^{on}$ ; see Figure 4.4.

In the following theorem we will derive a relationship which  $\tau_{r1}$  and  $\tau_{f1}$  need to satisfy in order to find a periodic solution with Property A. This involves fixing the integers  $j$  and  $k$  first. To that end define

$$h(k) = \frac{D_c}{\ln \left( \frac{1 - s_R^{off} (s_R^{off} / s_L^{on})^{D_c/k}}{1 - s_R^{off}} \right)} \ln \left( \frac{1 - s_R^{off}}{1 - s_L^{on}} \right) + D_c - 1. \quad (4.1)$$

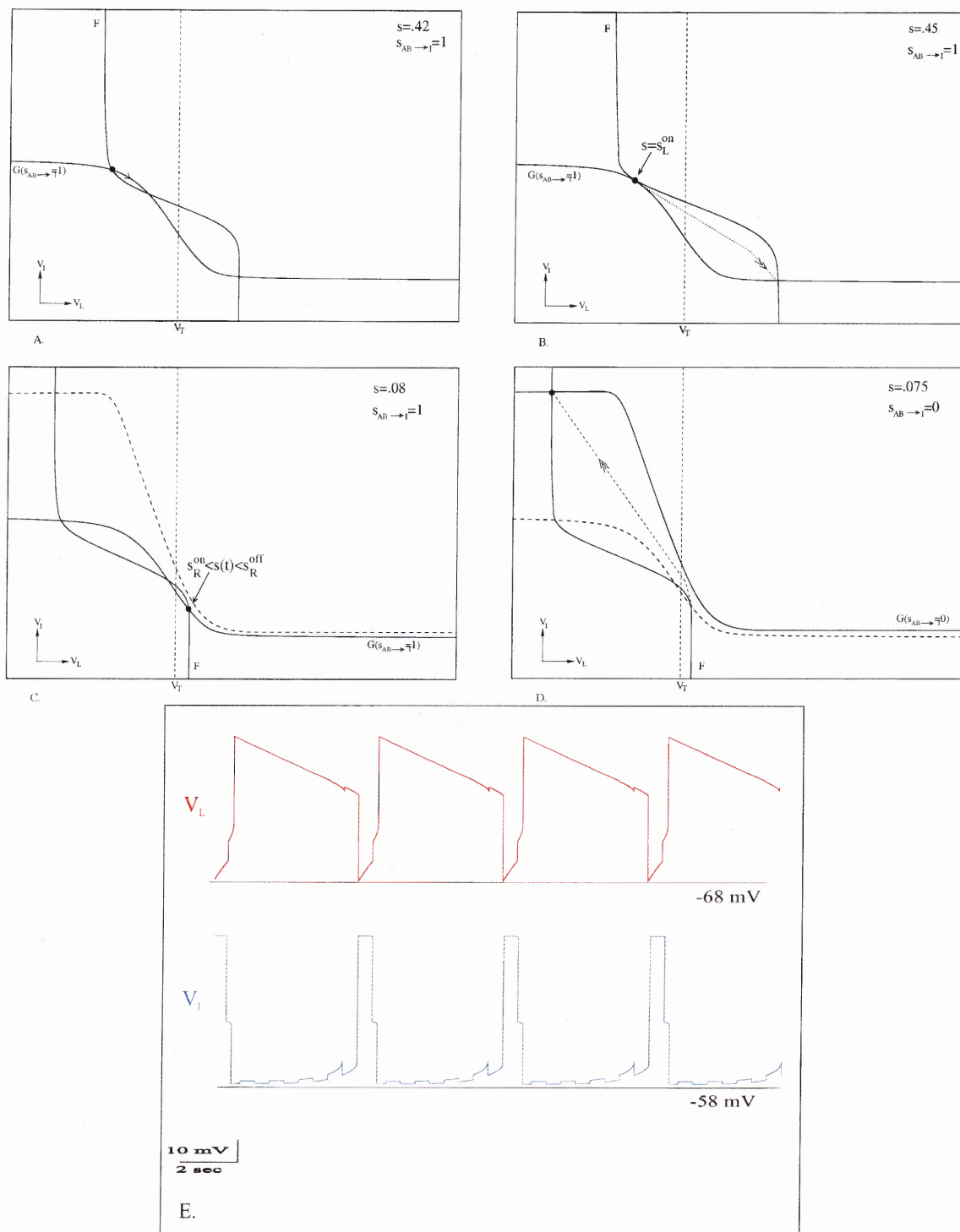


**Figure 4.4** In Case 2, a periodic orbit obeying property A jumps from the left to right branches and from the right to left branches of the nullclines in the following way. (A.) The trajectory lies at the stable fixed point ( $\bullet$ ) on the left branches of the nullclines where  $s_{AB \rightarrow I} = 1$  and  $s$  increases towards 1. (B.) While  $s_{AB \rightarrow I}$  remains equal to 1,  $s$  increases sufficiently large for a saddle-node bifurcation to occur at  $s_L^{on}$ . (C.) On the right branches of the nullclines, while  $s_{AB \rightarrow I} = 1$ ,  $s$  decreases below  $s_R^{off}$  but does not reach  $s_R^{on}$ . (D.) As soon as  $s_{AB \rightarrow I}$  jumps back to 0, the fixed point on the right branches of the nullclines is instantaneously lost because  $s < s_R^{off}$ . (E.) Voltage traces of  $V_L$  and  $V_I$  for a periodic orbit obeying property A.

**Theorem 1** Consider any ordered pair  $(j, k)$ , with  $1 \leq j < h(k)$ . There exists values  $\tau_{r1}(j)$ ,  $\tau_{f1}(k)$  and  $\bar{g}_{AB \rightarrow I}$  large enough such that Equations (3.22)-(3.24) and (3.28)-(3.29) possess a unique, asymptotically stable periodic solution obeying Property A with period  $P = (j + k + 1)P_{AB}$  where  $j$  is the number of times  $s_{AB \rightarrow I}$  oscillates between 0 and 1 while  $V_L < V_T$  and  $k$  is the number of time  $s_{AB \rightarrow I}$  oscillates between 0 and 1 when  $V_L > V_T$ , where  $P_{AB}$  is the period of  $s_{AB \rightarrow I}(t)$ .

**Proof:** A Poincare map  $\mathcal{P}$  of a certain interval  $\mathcal{I}$  into itself is constructed. We do this by first constructing an interval  $\mathcal{I}$  and then constructing the Poincare map  $\mathcal{P}$ . Existence and stability of the periodic solution is determined by showing that  $\mathcal{P}$  is a contraction on  $\mathcal{I}$ , thereby also yielding local uniqueness of the periodic solution. To construct the periodic solution in question, it will be shown that the associated trajectory will jump from the left to the right branches from the bifurcation point  $s_L^{on}$ . It will jump from the right to the left branches from a point  $s^* \in \mathcal{I}$  at one of the times when  $s_{AB \rightarrow I}$  switches from one to zero.

To construct  $\mathcal{I}$ , consider the points  $s_R^{off}$  and  $s_R^{on}$  corresponding to the bifurcation points along the right branches of the  $V_I$  and  $V_L$  nullclines when  $s_{AB \rightarrow I} = 0$  ( $AB$  off) and  $s_{AB \rightarrow I} = 1$  ( $AB$  on), respectively. By choosing  $\bar{g}_{AB \rightarrow I}$  and  $\tau_{f1}$  sufficiently large, we can guarantee that the time distance between  $s_R^{on}$  and  $s_R^{off}$  under the dynamics  $s' = -s/\tau_{f1}$  is larger than  $D_c P_{AB}$ . Indeed the time  $\Delta t$  between these two points on the right branches is  $\tau_{f1} \ln(s_R^{off}/s_R^{on})$ , where  $s_R^{on}$  is a decreasing function of  $\bar{g}_{AB \rightarrow I}$ . Moreover, there exists  $\hat{s}$  such that  $\hat{s} = s_R^{off} \exp(-D_c P_{AB}/\tau_{f1})$ . Thus the time distance between  $\hat{s}$  and  $s_R^{off}$  on the right branches is exactly  $D_c P_{AB}$ . Therefore, let  $\mathcal{I} = [\hat{s}, s_R^{off}]$ ; see Figure 4.5. Note that at this point, we have only stated that  $\tau_{f1}$  must be sufficiently large. Below, we will be more specific.

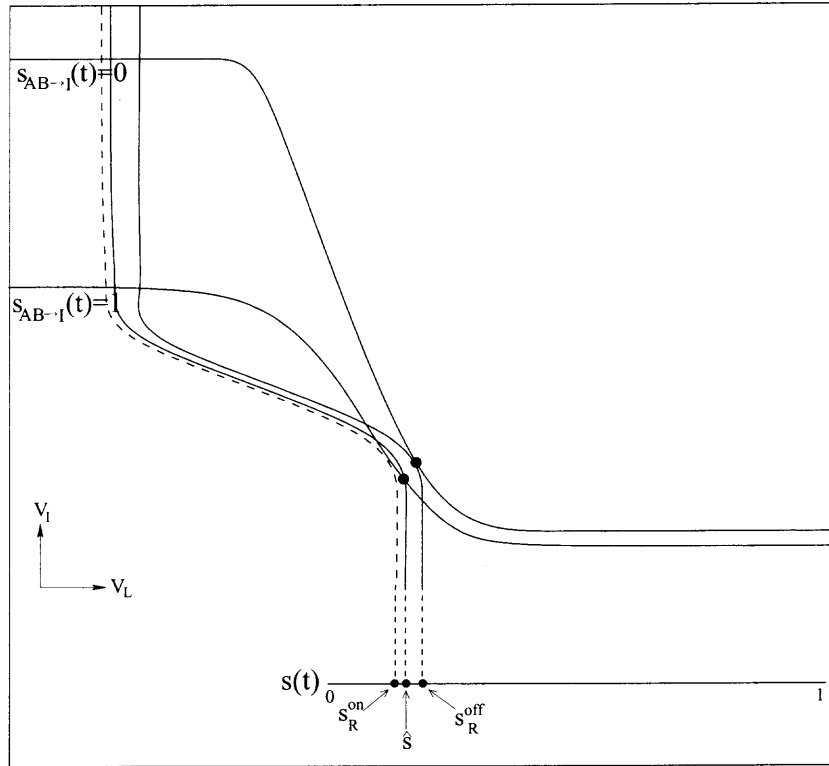


**Figure 4.5** To define the Poincaré map for Case 2, we let  $I = [\hat{s}, s_R^{off}]$  where  $\hat{s} = s_R^{off} \exp(-D_c P_{AB}/\tau_{f1})$ . Note that  $\tau_{f1}$  is chosen sufficiently large to ensure that  $\hat{s} > s_R^{on}$ .

Next, we show that  $\mathcal{I}$  maps into itself under the flow if  $\tau_{r1}$  and  $\tau_{f1}$  are chosen appropriately. We flow the endpoints of the interval  $\mathcal{I}$ ,  $s_R^{off}$  and  $\hat{s}$ , through one cycle of the  $V_I$  and  $V_L$  oscillation and show that these endpoints are mapped into  $\mathcal{I}$ . Thus by continuous dependence on initial conditions, all points in  $\mathcal{I}$  will map into  $\mathcal{I}$ .

First, consider a trajectory  $s_a(t)$  where  $s_a(0) = s_R^{off}$  and the trajectory is on the right branch. Let  $s_{AB \rightarrow I}(0^-) = 1$  and  $s_{AB \rightarrow I}(0^+) = 0$ , so that the trajectory jumps back to the left branch at  $t = 0^+$ . The dynamics of  $s_a$  on the left branches obey  $s' = (1 - s)/\tau_{r1}$ . By choosing

$$\tau_{r1}(j) = (j + 1 - D_c)P_{AB}/\ln([1 - s_R^{off}]/[1 - s_L^{on}]), \quad (4.2)$$

we can guarantee that  $s_a([j+1-D_c]P_{AB}) = s_L^{on}$ . This means that the trajectory which starts at  $s_R^{off}$  will leave the left branches of the nullclines through the bifurcation point  $s_L^{on}$  along the  $s_{AB \rightarrow I} = 1$  nullcline at time  $t = (j+1-D_c)P_{AB}$ .

Next consider a trajectory  $s_b(t)$  with the initial condition given by  $s_b(0) = \hat{s}$ . Recall that the time distance from  $\hat{s}$  to  $s_R^{off}$  on the right branches is  $D_c P_{AB}$ . This time is mostly determined by the time constant  $\tau_{f1}$ . On the left branches, the time between these points is governed by  $\tau_{r1}$  and is equal to  $\tau_{r1} \ln([1-\hat{s}]/[1-s_R^{off}])$ . Thus if

$$\tau_{r1} < \tau_{f1} \frac{\ln(s_R^{off}/\hat{s})}{\ln([1-\hat{s}]/[1-s_R^{off}])} \quad (4.3)$$

then the time between these points on the left branches will be less than  $D_c P_{AB}$ . In particular, the trajectory starting with initial condition at  $\hat{s}$  at  $t = 0$  will reach  $s_L^{on}$  when  $s_{AB \rightarrow I} = 1$  at a time  $T_1$  bounded between  $(j+1-D_c)P_{AB}$  and  $(j+1)P_{AB}$ . Therefore, any trajectory with  $s(0) \in \mathcal{I}$  will do the same.

Note that the time between any two trajectories remains invariant while they both evolve on the left branches and even across the jump back to the right branches. That the trajectories remain the same time distance apart on the left branches follows from the fact that they both obey the same differential equation ( $s' = (1-s)/\tau_{r1}$ ). Since they leave the left branches through the same point  $s_L^{on}$ , the time distance between them when the leading trajectory reaches the bifurcation point,  $s_L^{on}$ , is the same as the time distance apart when the trailing cell reaches this point. When both trajectories are on the right branches, the time distance, again remains invariant since both trajectories evolve under  $s' = -s/\tau_{f1}$ . In particular, the time distance between  $s_a(T_1)$  and  $s_b(T_1)$  is less than  $D_c P_{AB}$ .

Consider again the trajectory  $s_a(t)$  which had  $s_a(0) = s_R^{off}$  and  $s_a([j+1-D_c]P_{AB}) = s_L^{on}$ . We want this trajectory to spend  $k$  oscillations of  $s_{AB \rightarrow I}$  on the right branches. We also want the trajectory to be in a position to jump back to the left

branches when  $s_{AB \rightarrow I}$  switches from one to zero. Finally, since we want  $\mathcal{I}$  to map into itself, we choose

$$\tau_{f1}(k) = \frac{(k + D_c)P_{AB}}{\ln(s_L^{on}/\hat{s})}, \quad (4.4)$$

such that  $s_a([j+k+1]P_{AB}) = \hat{s}$ . We can replace  $\hat{s}$  in (4.4) by  $\hat{s} = s_R^{off} \exp(-D_c P_{AB}/\tau_{f1})$  to obtain

$$\tau_{f1}(k) = \frac{kP_{AB}}{\ln(s_L^{on}/s_R^{off})}. \quad (4.5)$$

In other words, with the choices of  $\tau_{r1}$  and  $\tau_{f1}$  that have been made, the trajectory with initial condition  $s_a(0) = s_R^{off}$  is mapped back to  $\hat{s}$  at a time  $T_2^- = (j + k + 1)P_{AB}$ . We point out here that these choices of  $\tau_{r1}$  and  $\tau_{f1}$  are made solely for the mathematical construction of the periodic orbit and do not make predictions about the physiological values of the synaptic rise and decay times.

Next consider the trajectory  $s_b(t)$  where  $s_b(0) = \hat{s}$  and  $s_b(T_1) = s_L^{on}$ . To construct the Poincare map, we need  $s_b(T_2^-) \in \mathcal{I}$ . Thus we need  $\hat{s} < s_b(T_2^-) < s_R^{off}$ . That  $\hat{s} < s_b(T_2^-)$  follows by continuity since  $\hat{s} = s_a(T_2^-) < s_b(T_2^-)$ . The value  $s_b(T_2^-) < s_R^{off}$  since the time between  $s_a(T_2^-) = \hat{s}$  and  $s_R^{off}$  is  $D_c P_{AB}$ , whereas the time between  $s_a(T_2^-)$  and  $s_b(T_2^-)$  is less than  $D_c P_{AB}$ .

It has just been shown that when  $\tau_{r1}$  is chosen to satisfy (4.2), the trajectories whose  $s$  values are associated with the end points of the interval  $\mathcal{I}$  get mapped to  $s_L^{on}$  at a time bounded between  $t = (j + 1 - D_c)P_{AB}$  and  $t = (j + 1)P_{AB}$ . Thus by continuity with respect to initial conditions on the left branches of the nullclines, any trajectory with  $s(0) \in \mathcal{I}$  will reach  $s_L^{on}$  at a time bounded between  $t = (j + 1 - D_c)P_{AB}$  and  $t = (j + 1)P_{AB}$ . Furthermore, with  $\tau_{f1}$  satisfying (4.5), the trajectories whose  $s$  values are associated with the end points of the interval  $\mathcal{I}$  get mapped back to  $\mathcal{I}$  at  $t = T_2^-$ . Again, the behavior of the solution trajectories is determined by the 1-dimensional flow for  $s$  and the trajectories with initial conditions lying in  $\mathcal{I}$  reach  $s_L^{on}$

between  $t = (j + 1 - D_c)P_{AB}$  and  $t = (j + 1)P_{AB}$ . Therefore, the solution trajectories for all initial conditions lying in  $\mathcal{I}$  are also flowed into  $\mathcal{I}$  at  $t = T_2^-$  by continuity with respect to initial conditions on the right branches of the nullclines. Therefore we can define a 1-dimensional Poincare map  $\mathcal{P} : \mathcal{I} \rightarrow \mathcal{I}$  where  $\mathcal{P}(s) = s(T_2^-)$ .

To show that  $\mathcal{P}$  is a contraction mapping on  $\mathcal{I}$ , let  $s_a(0) > s_b(0) \in \mathcal{I}$  be arbitrary. Let  $\Delta t$  denote the time on the right branch between them. At  $t = 0^+$ , the trajectories jump back to the left branch. Because of our choice of time constants  $\tau_{r1}(j)$  and  $\tau_{f1}(k)$ , the new time between these points is less than  $\Delta t$ . As before the time distance between these trajectories remains invariant as they evolve along the left branches, across the jump to the right branches and then back to  $\mathcal{I}$ . Since this new time is less than the original time,  $s_a(T_2^-) - s_b(T_2^-) < \alpha[s_a(0) - s_b(0)]$ , where  $\alpha < 1$  is dependent on  $\tau_{r1}$  and  $\tau_{f1}$ . Therefore  $\mathcal{P}$  is a contraction. As a result, there exists a unique value  $s_{Case\ 2}^* \in \mathcal{I}$  such that  $\mathcal{P}(s_{Case\ 2}^*) = s_{Case\ 2}^*$ . This value is asymptotically stable, and corresponds to a locally unique periodic solution of Equations (3.22)-(3.24) and (3.28)- (3.29).

Equation (4.3) provides a condition on the time constants  $\tau_{f1}$  and  $\tau_{r1}$  for which the theorem holds. This condition can be translated into a relationship between the integers  $j$  and  $k$ . Namely, by substituting  $\hat{s} = s_R^{off} \exp(-D_c P_{AB}/\tau_{f1})$  into the fraction on the right hand side of (4.3), we see that the numerator of that expression reduces to  $D_c P_{AB}/\tau_{f1}$ , while the denominator reduces to

$$\ln \left( \frac{1 - s_R^{off} \exp(-D_c P_{AB}/\tau_{f1})}{1 - s_R^{off}} \right). \quad (4.6)$$

Now substituting (4.5) into (4.6) and then substituting the resulting expression into (4.3), we obtain

$$\tau_{r1} < \tau_{f1} \frac{(D_c P_{AB}/\tau_{f1})}{\ln \left( \frac{1 - s_R^{off} (s_R^{off}/s_L^{on})^{D_c/k}}{1 - s_R^{off}} \right)}. \quad (4.7)$$

Canceling  $\tau_{f1}$  from the right-hand side, substituting  $\tau_{\tau1}$  from (4.2) and solving for  $j$ , we obtain

$$j < \frac{D_c}{\ln \left( \frac{1-s_R^{off}(s_R^{off}/s_L^{on})^{D_c/k}}{1-s_R^{off}} \right)} \ln \left( \frac{1-s_R^{off}}{1-s_L^{on}} \right) + D_c - 1. \quad (4.8)$$

The right-hand side of (4.8) is what we call  $h(k)$  in the statement of the theorem.

**Remark:** Note that if (4.8) is not satisfied, then we cannot find time constants  $\tau_{\tau1}$  and  $\tau_{f1}$  for which a periodic solution satisfying Property A exists. However, by choosing  $\tau_{\tau1}$  and  $\tau_{f1}$  differently, we could instead have easily constructed a periodic solution whose  $s_1$  value passed through the bifurcation point  $s_R^{off}$  on the transition from right to left branches and which jumped back to the right branches with  $s_1 \in (s_L^{on}, s_L^{off})$  when  $s_{AB \rightarrow I}$  switched from one to zero. In addition, we note that  $T_2^-$  is an integer multiple of  $P_{AB}$  as the full model of Nadim et al. [49] predicts it should be.

### 4.3 Case 3: Rhythmic MCN1 Excitation with AB Input to Int1 Absent

In Case 3, the input from AB to MCN1 is present ( $\bar{g}_{AB \rightarrow M} > 0$ ) so that the MCN1 elicited excitation to LG is rhythmic. Once again, we set  $\bar{g}_{AB \rightarrow I} = 0$  so that the  $V_I$  nullcline remains at a fixed position. In this case,  $s_2$  jumps instantaneously between  $s_{2min}$  and 1 while  $s_1$  increases with rate  $1/\tau_{\tau1}$  and decreases with rate  $1/\tau_{f1}$ , thus, causing the activity of  $s$  to be rhythmic. Therefore, the  $V_L$  nullcline slowly shifts to the right and left due to the dynamics of  $s_1$  while making instantaneous jumps to the left and right due to  $s_2$ .

#### 4.3.1 Possible Solution Trajectories for Case 3

Again, consider the nullclines. Suppose, the trajectory is at the stable fixed point on the right branches of the nullclines. When  $V_L > V_T$  and  $V_M > V_{Th(M)}$ , the  $V_L$  nullcline slowly shifts to the left due to  $s_1$  and then jumps further to the left when  $V_M < V_{Th(M)}$  due to the change in  $s_2$ . The jump to the left causes  $V_L$  to be at a lower

voltage. This is because when  $V_M$  goes below  $V_{Th(M)}$ , the excitation to  $LG$  is removed and, therefore, the voltage of  $LG$  is lowered. The distance that the trajectory jumps to the left depends on  $\tau_{f2}$  and the amount of time that  $AB$  inhibits  $MCN1$ .

At this point,  $s_1$  is still slowly pushing the  $V_L$  nullcline to the left. When  $V_M$  goes back above  $V_{Th(M)}$ ,  $s_2$  forces the  $V_L$  nullcline to jump back to the right (the excitation to  $LG$  is restored), returning the nullcline to the position it would have been at if  $V_M$  had never gone below  $V_{Th(M)}$ . The trajectory eventually jumps to the fixed point on the left branches of the nullclines when **(a.)**  $s_2 = 1$  and  $s_1$  moves the fixed point to the position where the nullclines are tangent as in Case 1, i.e.  $s_1 = s_R^{off}$  (see Figure 4.1(D.)) or **(b.)** when  $s_2 = s_{2min}$  and  $s_1$  decreases to  $s_R^{off}/s_{2min}$  moving the fixed point to the position where the nullclines are tangent or **(c.)** when  $s_2$  jumps to  $s_{2min}$  resulting in an instantaneous shift of the  $V_L$  nullcline past the point of bifurcation of the fixed points. Which case occurs depends on the speed at which  $s_1$  decreases ( $\tau_{f1}$ ), the amount of time the  $V_L$  nullcline spends being shifted to the left by  $s_2$  (the amount of time that  $s_{AB \rightarrow M}(t)$  spends in its active or inactive phases), and the timing of the instantaneous shifting of the  $V_L$  nullcline (timing of the  $AB$  input to  $MCN1$ ).

Once the trajectory has jumped to the left branches of the nullclines, the  $V_L$  nullcline slowly shifts to the right due to  $s_1$  and then instantaneously jumps to the left when  $V_M < V_{Th(M)}$  and back to the right when  $V_M > V_{Th(M)}$ . Again, the trajectory eventually jumps to the fixed point on the right branches of the nullclines when **(a'.)**  $s_2 = 1$  and  $s_1$  moves the fixed point to the position where the nullclines are tangent (i.e.  $s_1 = s_L^{off}$ ) as in Figure 3.12(A.) or when **(b'.)**  $s_2 = s_{2min}$  and  $s_1$  moves the fixed point to the position where the nullclines are tangent or when **(c'.)**  $s_2$  jumps to 1 resulting in an instantaneous shift of the  $V_L$  nullcline past the point of bifurcation of the fixed points as in Figure 3.12(B.).

### 4.3.2 Construction of Periodic Solution for Case 3

We shall establish the existence of the periodic solution which follows the subcases (c.) and (a'.) above. Namely, the trajectory will jump from the left to the right branches through the bifurcation point  $s_L^{off}$  and from the the right to the left branches when  $s_2$  jumps down from 1 to  $s_{2min}$ . Let us say that a periodic solution obeys Property B if the associated trajectory jumps from the right to left branches and from left to right branches in such a manner; see Figure 4.6.

Recall that  $s(t) = s_1(t) * s_2(t)$  where we consider  $s_2(t) = 1$  when  $V_M \geq V_{Th(M)}$  and  $s_2(t) = s_{2min}$  when  $V_M < V_{Th(M)}$ . When  $s_{AB \rightarrow M}(t)$  jumps to 1,  $V_M$  instantaneously jumps below  $V_{Th(M)}$ . Thus,  $s_2(t)$  instantaneously jumps to  $s_{2min}$ . However,  $s_{AB \rightarrow M}(t)$  does not instantaneously jump from 1 to 0, but slowly decays. Thus,  $V_M$  requires a a small amount of time,  $T_C$ , to go above  $V_{Th(M)}$ . In our model, we chose  $V_{Th(M)}$  such that  $T_C$  is approximately  $P_{AB}/20$ . Hence, for one cycle of  $AB$  activity,  $s_2(t) = s_{2min}$  for time  $D_c P_{AB} + T_C$  and  $s_2(t) = 1$  for time  $(1 - D_c)P_{AB} - T_C$ .

**Theorem 2** *Consider any ordered pair  $(j, k)$ , with  $1 \leq j < g(k)$ . There exists values  $\tau_{r1}(j)$ ,  $\tau_{f1}(k)$  such that Equations (3.22)-(3.24) and (3.28)-(3.29) possess a unique, asymptotically stable periodic solution obeying Property B with period  $P = (j + k + 1)P_{AB}$  where  $j$  is the number of times  $s_{AB \rightarrow M}$  oscillates between 0 and 1 while  $V_L < V_T$  and  $k$  is the number of time  $s_{AB \rightarrow M}$  oscillates between 0 and 1 while  $V_L > V_T$ .*

**Proof:**

As in Case 2, a Poincare map  $\mathcal{P}$  is constructed of an interval of  $s$  values on the right branch,  $I = [\tilde{s}, s_R]$ , into itself. Here  $s_R = s_1^R * 1$  where  $s_1^R = s_R^{off}/s_{2min}$ . Next let  $\tilde{s} = [s_1^R \exp([([D_c - 1]P_{AB} + T_C)/\tau_{f1})] * 1$  so that the time distance between  $s_R$  and  $\tilde{s}$  is  $[1 - D_c]P_{AB} - T_C$ . Let  $\tilde{s}_1 = [s_1^R \exp([([D_c - 1]P_{AB} + T_C)/\tau_{f1})]$ ; see Figure 4.7.

We consider a trajectory  $s_a(t)$  where  $s_a(0^-) = s_1^R * s_2(0^-)$  and the trajectory is on the right branch of the nullclines. Let  $s_{AB \rightarrow M}(0^-) = 0$  and  $s_{AB \rightarrow M}(0^+) = 1$

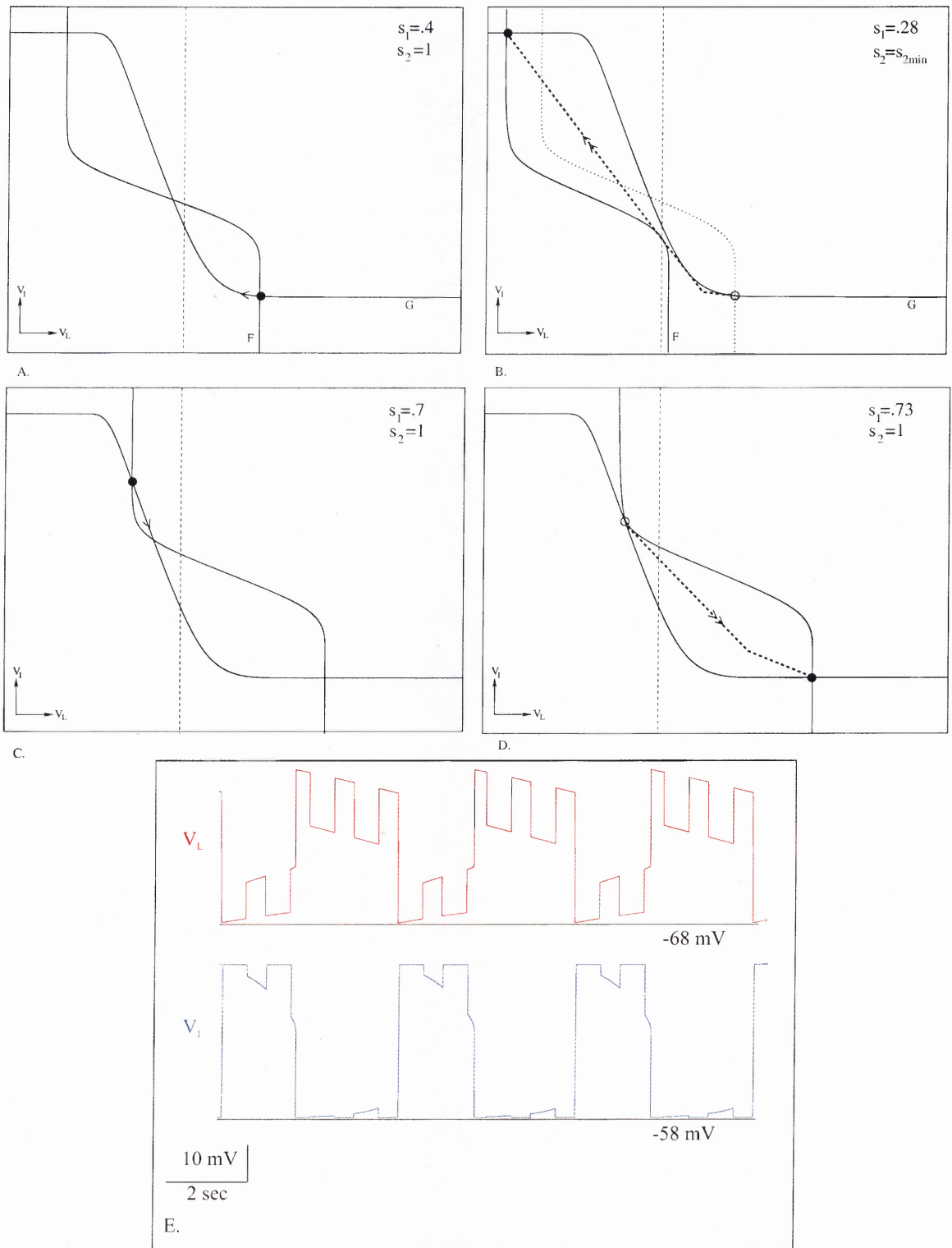


**Figure 4.6** Case 3 solution trajectory and nullclines obeying Property B. (A.) The trajectory lies at the stable fixed point (●) on the right branches of the nullclines where  $s_{AB \rightarrow I} = 0$  and  $s_2 = 1$ . (B.) When  $s_2$  jumps to  $s_{2min}$ ,  $s$  instantaneously goes below  $s_R^{off}$  and the fixed point is lost. (C.)-(D.) On the right branches of the nullclines, the fixed point is lost while  $s_2 = 1$  and  $s_1$  increases large enough for the saddle-node bifurcation to occur through  $s_L^{off}$ . (E.) Voltage traces of  $LG$  and  $Int1$  for  $s$  satisfying the above conditions.

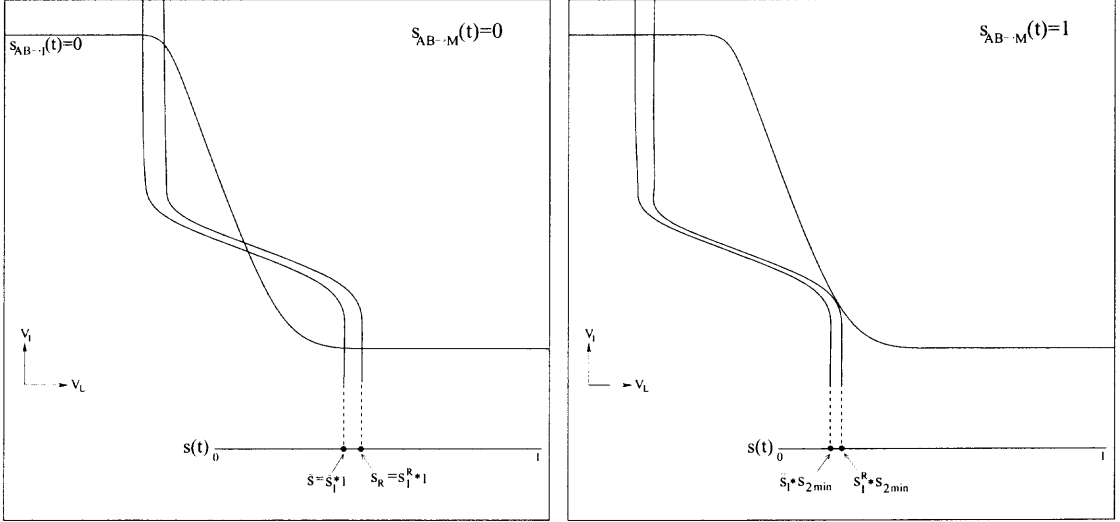


**Figure 4.7** (A.) To define the Poincare map for Case 3, we let  $I = [\tilde{s}, s_R]$  where  $s_R = s_1^R * 1$ ,  $s_1^R = s_L^{off} / s_{2min}$  and  $\tilde{s} = [s_1^R \exp([(D_c - 1)P_{AB} + T_C] / \tau_{f1}) * 1$ . (B.) For  $s = s_R$ , when  $s_2$  jumps from 1 to  $s_{2min}$ ,  $s$  jumps to  $s_R^{off}$ . Similarly, for  $s = \tilde{s}$ , when  $s_2$  jumps to  $s_{2min}$ ,  $s$  jumps to  $\tilde{s}_1 * s_{2min}$ .

so that  $s_2(0^-) = 1$  and  $s_2(0^+) = s_{2min}$ . Thus the trajectory jumps back to the left branch at  $t = 0^+$  when  $s_2$  jumps from 1 to  $s_{2min}$ .

We then choose

$$\tau_{\tau_1}(j) = ((j + D_c)P_{AB} + T_C) / \ln([1 - s_1^R] / [1 - s_L^{off}]) \quad (4.9)$$

which guarantees that  $s_a((j + D_c)P_{AB} + T_C) = s_L^{off}$  so that the trajectory which starts at  $s_R$  at  $t = 0^-$  will leave the left branches of the nullclines through the bifurcation point  $s_L^{off}$  at  $t = (j + D_c)P_{AB} + T_C$ . Using the same argument as in Case 2 with an equivalent condition on  $\tau_{\tau_1}$  as in (4.3), the trajectory  $s_b(t)$  with initial condition  $s_b(0) = \tilde{s}_1 * s_2(0)$  will be forced to reach  $s_L^{off}$  at a time  $T_1$  bounded between  $(j + D_c)P_{AB} + T_C$  and  $(j + 1)P_{AB}$ . Therefore, any trajectory with  $s(0) \in I$  will also reach  $s_L^{off}$  during these times. This exact condition on  $\tau_{\tau_1}$  is

$$\tau_{r1} < \tau_{f1} \frac{\ln(s_1^R/\tilde{s}_1)}{\ln(1-\tilde{s}_1)/(1-s_1^R)}. \quad (4.10)$$

With this condition satisfied, the time distance between  $s_1^R$  and  $\tilde{s}_1$  on the right branches of the nullclines is  $(1-D_c)P_{AB} - T_C$  but the time distance between  $s_1^R$  and  $\tilde{s}_1$  on the left branches of the nullclines is less than  $(1-D_c)P_{AB} - T_C$ .

Next, we choose  $\tau_{f1}(k)$  so that  $s_a(t)$  gets mapped back to  $I$ , particularly to  $\tilde{s}$  at the instant before  $s_{AB \rightarrow M}(t)$  jumps from 0 to 1. Therefore, we let

$$\tau_{f1}(k) = [[k + [1 - D_c]]P_{AB} - T_C] / \ln(s_L^{off}/\tilde{s}_1). \quad (4.11)$$

By plugging  $\tilde{s}_1 = s_1^R \exp\left[-\frac{(1-D_c)P_{AB}-T_C}{\tau_{f1}}\right]$  into (4.11), this condition on  $\tau_{f1}(k)$  simplifies to

$$\tau_{f1}(k) = \frac{kP_{AB}}{\ln(s_L^{off}/s_1^R)}. \quad (4.12)$$

Thus, at  $s_a(T_2^-)$  where  $T_2 = (k+j+1)P_{AB}$ ,  $s_a(t)$  lies in  $I$ . In a similar argument to that of Case 2, the trajectory  $s_b(t)$  with  $s_b(0) = \tilde{s}_1 * s_2(0)$  and  $s_b((j+1)P_{AB}) = s_L^{off}$  will also lie in  $I$  at  $t = T_2^-$  with  $\tilde{s} = s_a(T_2^-) < s_b(T_2^-) < s_R$ . Again, as in Case 2, since the behavior of the solution trajectories is determined by the 1-dimensional flow for  $s$  and the trajectories with initial conditions being the endpoints of  $\mathcal{I}$  are flowed back into  $\mathcal{I}$  at a time  $t = T_2^-$ , the solution trajectories for all initial conditions lying in  $\mathcal{I}$  are also flowed into  $\mathcal{I}$  at  $t = T_2^-$ .

This defines a one-dimensional Poincare map  $\mathcal{P} : \mathcal{I} \rightarrow \mathcal{I}$  where  $\mathcal{P}(s) = s(T_2)$ . The argument showing that  $\mathcal{P}$  is a contraction mapping on  $I$  is the same as in Case 2. Consequently, there exists a locally unique, asymptotically stable value  $s_{Case\ 3}^* \in I$  such that  $\mathcal{P}(s_{Case\ 3}^*) = s_{Case\ 3}^*$ .

Again, we can find a relationship between  $j$  and  $k$  for which Theorem 2 holds. Substituting  $\tilde{s}_1 = s_1^R \exp\left[-\frac{[(1-D_c)P_{AB}-T_C]}{\tau_{f1}}\right]$  into the right-hand side of (4.10), we obtain the new relationship

$$\tau_{r1} < \frac{(1-D_c)P_{AB}-T_C}{\ln \frac{1-s_1^R \exp\left[-\frac{[(1-D_c)P_{AB}-T_C]}{\tau_{f1}}\right]}{(1-s_1^R)}}. \quad (4.13)$$

Then plugging (4.12) into (4.13), this equation simplifies to

$$\tau_{r1} < \frac{(1-D_c)P_{AB}-T_C}{\ln \frac{1-s_1^R (s_1^R/s_L^{off})^{[(1-D_c)P_{AB}-T_C]/kP_{AB}}}{(1-s_1^R)}}. \quad (4.14)$$

Finally, we can replace  $\tau_{r1}$  in Equation (4.14) by (4.9) to obtain

$$j < \frac{[(1-D_c)P_{AB}-T_C] \ln\left(\frac{1-s_1^R}{1-s_L^{off}}\right)}{P_{AB} \ln \frac{1-s_1^R (s_1^R/s_L^{off})^{[(1-D_c)P_{AB}-T_C]/kP_{AB}}}{(1-s_1^R)}} - T_C - D_c P_{AB}. \quad (4.15)$$

The right-hand side of Equation (4.15) is the function  $g(k)$  in the statement of Theorem 2.

**Remark-** The period of the constructed solutions in Cases 2 and 3 are both  $(j+k+1)P_{AB}$ . Note that this occurs since the values of  $\tau_{r1}(j)$  and  $\tau_{f1}(k)$  are chosen to be different in both cases. In general, if *a priori*,  $\tau_{r1}$  is chosen to have the same value for both Cases 2 and 3, and similarly for  $\tau_{f1}$ , then the periods of Cases 2 and 3 need not be the same.

#### 4.4 Case 4: Rhythmic MCN1 Excitation with AB Input to Int1 Present

In Case 4, the MCN1 to LG excitation is rhythmic ( $\bar{g}_{AB \rightarrow M} > 0$ ) and AB inhibits Int1 ( $\bar{g}_{AB \rightarrow I} > 0$ ). Consequently, the  $V_L$  nullcline shifts to the right and left with slow changes in  $s_1$  and with quick jumps of  $s_2$  between 1 and  $s_{2min}$ . The  $V_I$  nullcline jumps up and down instantaneously due to the  $s_{AB \rightarrow I}$  oscillations between 0 and 1.

##### 4.4.1 Possible Solution Trajectories for Case 4

Suppose the trajectory lies at the stable fixed point on the left branches of the  $V_L$  and  $V_I$  nullclines. Here,  $V_L < V_T$  which allows  $s_1$  to increase. When  $s_{AB \rightarrow M}(t) \rightarrow 1$ , the  $V_L$  nullcline jumps to the left. Similarly, when  $s_{AB \rightarrow I}(t) \rightarrow 1$ , the  $V_I$  nullcline jumps down. Recall that the time difference between when the  $V_L$  and  $V_I$  nullclines shift is controlled by the parameter  $m$ . For example, if  $m = 0$ , the  $V_L$  nullcline jumps to the left at the same time that the  $V_I$  nullcline jumps down. However if  $m = D_c P_{AB}$  then when the  $V_L$  nullcline jumps to the left, the  $V_I$  nullcline jumps up. This creates several possibilities for the length of the period.

To provide more insight into the role of  $m$ , suppose again that  $m = 0$ . In Case 2, the jumping down of the  $V_I$  nullcline allowed the fixed point to bifurcate at smaller values of  $s_1$  relative to Case 1. However, for  $m = 0$ , whenever the  $V_I$  nullcline jumps down, the  $V_L$  nullcline jumps back to the left. If this jump to the left is large enough ( $1 - s_{2min}$  is large) and the jump down in the  $V_I$  nullcline is not extremely large, there will still exist a stable fixed point on the left branches. In this case, the trajectory will have to wait until  $s_2 = 1$  and  $s_1$  has grown large enough so that the fixed point occurs where the nullclines intersect tangentially for  $s_{AB \rightarrow I}(t) = 0$  (figure 3.12(A.)) or when  $s_2$  jumps to 1 ( $s_{AB \rightarrow M}(t)$  jumps to 0) and the fixed point is instantaneously lost (figure 3.12(B.)). This is equivalent to (a.) and (c.) in Case 3. If the jump to the left of the  $V_L$  nullcline is not large and/or the jump down in the  $V_I$  nullcline is extremely large, the fixed point will be lost and the trajectory will immediately jump to the

stable fixed point on the right branches of the nullclines. This is equivalent to Case 2. The above result also extends to the situation in which  $m \in (0, T_C]$  because for  $0 < m \leq T_C$ , each time the  $V_I$  nullcline is in the downward position, the  $V_L$  nullcline is shifted to the left. Therefore, the fixed point can not be lost until  $s_1$  grows large enough for the bifurcation to occur while  $s_2 = 1$ .

Next suppose that  $m = D_c P_{AB}$ . For  $m = D_c P_{AB}$ , each time the  $V_I$  nullcline is shifted in the downward position, the  $V_L$  nullcline remains to the right. Therefore, as opposed to the situation in which  $m = 0$ , the fixed point on the left branches of the nullclines can be lost due to the jump down of the  $V_I$  nullcline as in Case 2; see Figure 3.12(C.). This same idea extends to values of  $m$  lying in a neighborhood,  $[R_1, R_2]$ , of  $D_c P_{AB}$  where  $R_1 > T_C$ ,  $R_2 < P_{AB}$ . For  $m \in [R_1, R_2]$ , there is always some amount of time for which the  $V_L$  nullcline is to the right while the  $V_I$  nullcline is shifted downward, thus allowing the fixed point to be lost at an earlier time than in Case 3.

#### 4.4.2 Construction of Periodic Solution for Case 4

We now consider the existence of a periodic solution for Case 4 with  $\tau_{r1}(j)$  and  $\tau_{f1}(k)$  defined as in Case 3. For  $m \in (0, T_C]$ , the periodic orbit will be defined in exactly the same way as Case 3. Consider the interval  $I$  on the right branches as defined in Case 3 with  $s_{AB \rightarrow M}(0^-) = 0$  and  $s_{AB \rightarrow M}(0^+) = 1$ . Let  $s_a(t)$  be a trajectory with  $s_a(0) = s_1^R * s_2(0)$ . At  $t = 0^+$ ,  $s_{AB \rightarrow M}$  jumps to 1 and  $s_{AB \rightarrow I}$  remains equal to 0 because of the small delay  $m$ . Thus,  $s_2$  instantaneously jumping to  $s_{2min}$  forces the trajectory to the left branches in the same way as Case 3 because the  $V_I$  nullcline remains in the upward position at  $t = 0^+$ .

On the left branches with  $m \in (0, T_C]$ , each time  $s_{AB \rightarrow I} = 1$ , pushing the  $V_I$  nullcline down,  $s_2 = s_{2min}$  and the  $V_L$  nullcline is forced to the left. Thus, the trajectory with initial conditions as stated above can not jump from  $s_L^{on}$  as in Case

2 because each time the  $V_I$  nullcline is in its downward position, the  $V_L$  nullcline is shifted too far to the left for  $s$  to reach  $s_L^{on}$ . Therefore, the only time at which the fixed point of the left branches can be lost is when  $s_2 = 1$ . At  $t = (j + D_C)P_{AB}$ ,  $s_{AB \rightarrow M}(t)$  will jump to 0. However,  $s_2$  will not jump to 1, returning the  $V_L$  nullcline to the right, until  $t = (j + D_C)P_{AB} + T_C$ . Hence, at  $t = (j + D_C)P_{AB} + T_C$ ,  $s_{AB \rightarrow I}$  will already be equal to 0 since  $m \leq T_C$  and the trajectory will reach  $s_L^{off}$  tangentially as in Case 3. By choosing  $\tau_{f1}(k)$  as in Case 3,  $s_a(t)$  gets mapped to  $\tilde{s}$  at  $t = T_2^-$ .

With the same argument as in Case 3, the trajectory  $s_b(t)$  with  $s_b(0) = \tilde{s}_1 * s_2(0)$  and  $s_b(T_1) = s_L^{off}$  (where  $T_1 \in ((j + D_C)P_{AB} + T_C, (j + 1)P_{AB} + T_C)$ ) will also be mapped back to  $I$  at  $t = T_2^-$  with  $\tilde{s} = s_a(T_2^-) < s_b(T_2^-) < s_R$ . Therefore, the 1-dimensional Poincare map  $\mathcal{P} : \mathcal{I} \rightarrow \mathcal{I}$  where  $\mathcal{P}(s) = s(T_2)$  is established exactly as in Case 3. Thus for  $m \in (0, T_C]$ , the same arguments apply to show that there exists a unique, asymptotically stable periodic orbit in Case 4 and the periodic orbits of Cases 3 and 4 have the same period.

For  $m \in [R_1, R_2]$ , the period of the solution trajectories in Case 4 is locked to the period of  $s_{AB}$  oscillations and is, therefore, much shorter than the period of solution trajectories in Case 3. For  $m \in [R_1, R_2]$ , as stated above, on the left branches of the nullclines, the inhibition from  $AB$  to  $MCN1$  and to  $Int1$  is timed such that while the  $V_I$  nullcline is shifted downward,  $s_2 = 1$  which places the  $V_L$  nullcline to the right. Thus,  $s_1$  does not need to grow very large for the  $LG$  interburst to end. Once on the right branches, the burst of  $LG$  is ended during the first time  $s_2$  jumps to  $s_{2min}$  because  $s_1$  is sufficiently small (due to the fact that the  $LG$  interburst was ended for a small value of  $s_1$ ) to push the  $V_L$  nullcline far enough to the left to cause a loss in the fixed point. Similarly, once the solution trajectory is back to the left branches,  $s_1$  is large enough (because  $s_1$  did not decay a long time on the right branches) so that the first jump in  $s_2$  back to 1 causes a loss in the fixed point and an end to the  $LG$  interburst (because while  $s_2 = 1$ , the  $V_I$  nullcline is shifted downward).

In the regions  $T_C < m < R_1$  and  $R_2 < m \leq P_{AB}$ , the solution trajectories remain periodic but are slightly more complicated to describe than those outside of these regions. For example, with the parameters fixed as above, when  $m \in (0, T_C]$  or  $m \in [R_1, R_2]$  consecutive *LG* bursts have exactly the same length as do consecutive *Int1* burst. However, when  $m$  is not in these regions, consecutive *LG* bursts and consecutive *Int1* bursts need not have the same length. Instead, several cycles of *LG* and *Int1* oscillations may be required before the *LG* (and *Int1*) burst duplicates its length. We further explain this in the next section.

#### 4.5 Determining the Frequency of Solutions

The period of the gastric mill rhythm can be computed as the sum of the *LG* burst time and the *LG* interburst time. Thus, the period of the solution trajectories is calculated as the amount of time spent on the left branches (*LG* in its interburst) plus the amount of time spent on the right branches (*LG* in its burst). We assume that the jump from the left to right branches and from the right to left branches of the nullclines is instantaneous. The amount of time the solution trajectory spends on the left and right branches of the nullclines is determined by the dynamics of  $s_1(t)$ . During the interburst,  $s_1$  increases towards a maximum value which we shall denote  $s_{max}$ . Similarly, during the burst,  $s_1$  decreases towards a minimum value  $s_{min}$ . The periodic solutions in Cases 1-4 are then computed by finding out how much times is needed for  $s_1$  to evolve between the values of  $s_{max}$  and  $s_{min}$  on the left (during the interburst) and right (during the burst) branches.

When  $s_1$  is increasing, the trajectory is on the left branches and when  $s_1$  is decreasing, the trajectory is on the right branches of the nullclines. Therefore, we rewrite

$$\frac{ds_1}{dt} = \begin{cases} [1 - s_1]/\tau_{r1} & V_L \leq V_T \\ -s_1/\tau_{f1} & V_L > V_T \end{cases} \quad (4.16)$$

as two separate equations.  $s_{1rise}(t)$  is the value of  $s_1$  while it is increasing on the left branches of the nullclines and  $s_{1fall}(t)$  is the value of  $s_1$  while it is decreasing on the right branches of the nullclines. This implies that

$$\frac{ds_{1rise}}{dt} = \frac{1 - s_{1rise}}{\tau_{r1}} \quad \text{and} \quad \frac{ds_{1fall}}{dt} = -\frac{s_{1fall}}{\tau_{f1}} \quad (4.17)$$

Solving (4.17) for  $s_{1rise}$  and  $s_{1fall}$ , we obtain  $s_{1rise}(t) = 1 + c_1 e^{-\frac{t}{\tau_{r1}}}$  and  $s_{1fall}(t) = c_2 e^{-\frac{t}{\tau_{f1}}}$ . Next, we define  $s_{1rise}$  to be at its minimum,  $s_{min}$ , at time  $t = 0$ . Thus, we find that  $c_1 = s_{min} - 1$ .

$$\Rightarrow s_{1rise}(t) = 1 + (s_{min} - 1)e^{-\frac{t}{\tau_{r1}}}. \quad (4.18)$$

Similarly, we define  $s_{1rise}(t)$  to reach its maximum,  $s_{max}$ , at time  $t = B$ .

$$\Rightarrow s_{1rise}(B) = 1 + (s_{min} - 1)e^{-\frac{B}{\tau_{r1}}} = s_{max} \quad (4.19)$$

By continuity at  $t = B$ ,  $s_{1fall}(t)$  is at  $s_{max}$

$$\Rightarrow s_{1fall}(B) = c_2 e^{-\frac{B}{\tau_{f1}}} = s_{max}. \quad (4.20)$$

Solving (4.20) for  $c_2$ , we find that

$$s_{1fall}(t) = s_{max} e^{\frac{B-t}{\tau_{f1}}}. \quad (4.21)$$

We then define  $t = P$  to be the time at which  $s_{1fall}$  reaches  $s_{min}$ . Note that the period of one *LG* or *Int1* oscillation is  $P$ .

$$\Rightarrow s_{1fall}(P) = s_{max} e^{\frac{B-P}{\tau_{f1}}} = s_{min} \quad (4.22)$$

Solving (4.22) for  $B - P$ , we find

$$B - P = \tau_{f1} \ln \left( \frac{s_{min}}{s_{max}} \right) \quad (4.23)$$

and from (4.19),  $B = -\tau_{r1} \ln \left( \frac{s_{max}-1}{s_{min}-1} \right)$

$$\Rightarrow P = \tau_{r1} \ln \left( \frac{1 - s_{min}}{1 - s_{max}} \right) + \tau_{f1} \ln \left( \frac{s_{max}}{s_{min}} \right) \quad (4.24)$$

The main question now is to determine the values  $s_{min}$  and  $s_{max}$  for each of the four cases. However, these values have already been determined in the construction of the periodic solutions above. In particular, for Case 1,  $s_{min} = s_R^{off}$  and  $s_{max} = s_L^{off}$ . For Case 2,  $s_{min} = s_{Case\ 2}^*$  and  $s_{max} = s_L^{on}$ . We can approximate  $s_{Case\ 2}^*$  as the average of  $s_R^{off}$  and  $s_L^{on}$ . Note that  $s_L^{on} < s_L^{off}$ . Thus from Equation (4.24), it is seen that the period of Case 2 is smaller than the period of Case 1 since the interburst phase of *LG* is shorter. This result is consistent with what was found by Manor et al. [40].

In Case 3,  $s_{min} = s_{Case\ 3}^*$  and  $s_{max} = s_L^{off}$ . Here  $s_{Case\ 3}^* \in [s_1^R \exp(([(D_c - 1]P_{AB} + T_C)/\tau_{f1}]), s_1^R]$  and can, therefore, be approximated by  $s_R^{off}/s_{2min}$ . Again,  $s_1^R = s_R^{off}/s_{2min}$ . Finally, for Case 4, when  $m \in (0, T_c]$ , the periodic solution is different than the one constructed in Case 3 due to the shifting of the  $V_I$  nullcline. However, the period of the solutions in Cases 3 and 4 are the same because the values of  $s_{min}$  and  $s_{max}$  are the same. In Case 4, the values of  $s_{max}$  and  $s_{min}$  depend on  $m$ . For  $m$  near 0, for example,  $s_{max}$  and  $s_{min}$  are calculated as in Case 3. When

$m > T_c$ ,  $s_{min} \in [s_1^R \exp([D_c - 1]P_{AB} + T_C)/\tau_{f1}), s_1^R]$  and  $s_{max} \in [s_L^{on}, 1 + (s_L^{on} - 1)\exp(-(D_C P_{AB} + T_C)/\tau_{r1})]$ . Calculations of  $s_L^{off}$ ,  $s_R^{off}$ ,  $s_L^{on}$ , and  $s_R^{on}$  can be found in Appendix D.

To confirm the validity of our analytical computations of the period from (4.24), we numerically solved the set of dimensional equations in our model using XPPAUT [22]. The parameter values of the reduced model are given in Table 4.1. The results of the numeric calculations are given in Table 4.2 for Cases 1-3 and show a close match between the periods obtained analytically and numerically. The period of the gastric mill rhythm in Case 4 is dependent upon the value of  $m$  and we, therefore, do not analytically calculate the period over the full range of  $m$ . In section 4.6, the period of the gastric mill rhythm over the full range of  $m$  values is numerically calculated.

**Table 4.1** Parameters of The Expanded, Reduced Model

$g_{leak,L} = 1mS/cm^2$	$E_{leak,L} = -60mV$	$g_{I \rightarrow L} = 5mS/cm^2$	$E_{I \rightarrow L} = -80mV$
$g_{leak,I} = .75mS/cm^2$	$E_{leak,I} = 10mV$	$g_{L \rightarrow I} = 2mS/cm^2$	$E_{L \rightarrow I} = -80mV$
$g_{leak,M} = 2mS/cm^2$	$E_{leak,M} = 10mV$		$E_{AB \rightarrow M} = -60mV$
$g_s = 4mS/cm^2$	$E_s = 43mV$	$V_T = -30mV$	$E_{AB \rightarrow I} = -60mV$

**Table 4.2** Comparison of The Frequency Calculated Through XPP Simulations and The Analytic Formula

Period Calculation for $\tau_{r1} = 4900$ msec, $\tau_{f1} = 4000$ msec		
	XPP Simulation	Analytic Formula
Case 1	Period=10,140 msec	Period=10,075 msec
Case 2	Period=5,000 msec	Period=4,688 msec
Case 3	Period=4,000 msec	Period=3794 msec

#### 4.6 Comparison Between Simulations of The Expanded, Reduced Model and Experimental Results

The motivation behind considering the effect of rhythmic *MCN1* excitation on the gastric mill rhythm emanated from recent experimental work on the STG done by Wood et al. [73] and work done by Bartos et al. [5]. In their experiments, Bartos et al. used the dynamic clamp technique to artificially replicate the *AB* affect on the gastric mill. Bartos et al. showed that when *MCN1* is tonic, the pyloric rhythm regulates the speed of the gastric mill network through the inhibitory synapse from *AB* to *Int1*. In the absence of the inhibitory input from *AB* to *Int1*, the gastric mill rhythm is slow but when the synapse from *AB* to *Int1* is intact, the rhythm frequency greatly increases.

Wood et al. [73] examined the effect of the rhythmic behavior of *MCN1* on the gastric mill network in the presence and absence of the direct *AB* input to *Int1*. In this work, Wood et al. artificially replicated the effect of *AB* activity to *MCN1* through computer controlled stimulation of *MCN1*. Wood et al. showed that when *MCN1* is rhythmic and the *AB* synapse to *Int1* is absent, there is a comparable frequency of the gastric mill rhythm to the case when *MCN1* is tonic and the *AB* synapse to *Int1* is present. We reiterate that the rhythmicity of *MCN1* is a result of the periodic inhibition of *MCN1* by *AB*. Therefore, it seems that the rhythmic *MCN1* input to *LG* may serve as a second pathway by which the pyloric circuit regulates the rhythm of the gastric mill circuit [73].

In addition, Wood et al. [73] showed that when *MCN1* is rhythmic and the *AB* synapse to *Int1* is intact, there is no change in frequency from when *MCN1* is rhythmic and the *AB* synapse to *Int1* is not present. Figure 4.8 shows the gastric mill rhythm frequency as found in experiments by Wood et al. for Cases 1-4. We see that for *MCN1* tonic, the frequency of the network is much higher when the *AB* input to *Int1* is present. For *MCN1* rhythmic, the frequency of the network is higher

than when *MCN1* is tonic, however, there is no change in frequency when the *AB* input to *Int1* is added to the network.

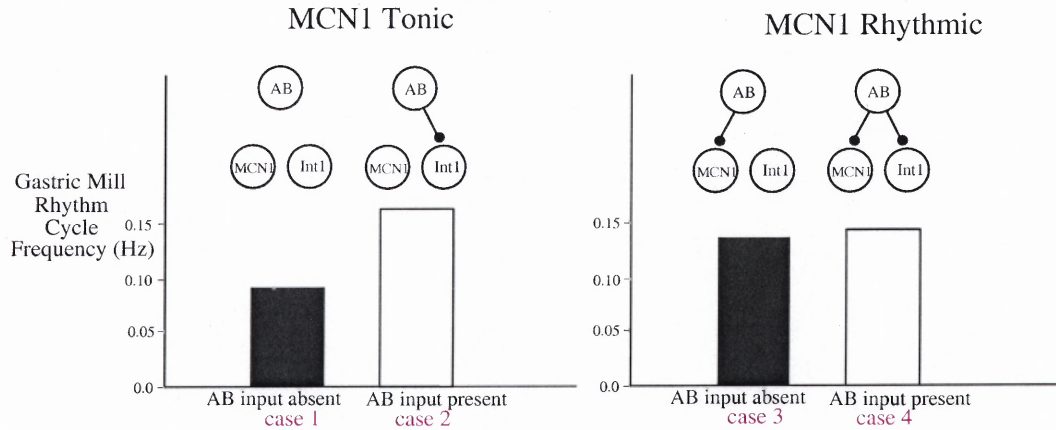


**Figure 4.8** Experimental findings of the gastric mill rhythm cycle frequency for Cases 1-4 [73].

While these experimental results are very useful in understanding the influence of the synaptic inputs on the gastric mill rhythm, they do not reveal the mechanism by which these behaviors are produced. In particular, it is unclear what prevents the direct *AB* input to *Int1* from further increasing the gastric mill frequency when *MCN1* is rhythmic as it does when *MCN1* is tonic. By use of our model, we can now explain these observations. In Case 1, it is clear that the period of the gastric mill rhythm is solely determined by the amount of excitation that *LG* receives from *MCN1* and by the rate at which the pre-synaptic inhibition from *LG* removes this excitation. Thus, the burst duration of *LG* is determined by the rate at which the conductance of the pre-synaptic inhibition increases and the interburst phase is determined by the rate at which the pre-synaptic inhibition decreases, thus, allowing *LG* to receive the excitation. In Case 2, *LG* again receives the excitatory input from *MCN1*. However, the periodic “disinhibition” of *LG* by *AB* allows *LG* to escape from *Int1*’s inhibition at an earlier time. This causes the interburst duration of *LG* and, therefore, the period of the gastric mill rhythm to be shorter. In Case 3, the period of the gastric mill rhythm is shorter because each time *AB* inhibits *MCN1*,

the excitation to  $LG$  is removed. This facilitates the ending of the  $LG$  burst in that it is not necessary for the conductance of the pre-synaptic inhibition to grow as large to end the  $LG$  burst.

In Case 4, the period of the gastric mill rhythm is dependent upon the delay between the timing of the  $AB$  inputs to  $Int1$  and to  $MCN1$ . For the delay in a neighborhood of 0, each time  $AB$  disinhibits  $LG$ , the  $MCN1$  excitation to  $LG$  is removed so that the disinhibition has no effect on ending  $LG$ 's inactive phase. The rhythmicity of  $MCN1$  facilitates the ending of  $LG$ 's burst duration by removing the  $MCN1$  excitation as in Case 3. Thus, for no or a small delay, the period of Case 4 is the same as the period of Case 3 because the  $AB$  input to  $Int1$  does not affect the  $LG$  interburst or burst. For a delay in the neighborhood of  $D_c P_{AB}$ , however, each time  $AB$  disinhibits  $LG$ , the  $MCN1$  excitation to  $LG$  is not removed. Consequently,  $AB$  does facilitate the ending of the  $LG$  interburst duration as it does in Case 2. In addition, the rhythmicity of  $MCN1$  facilitates the ending of  $LG$ 's burst duration as in Case 3. Therefore, the period of the gastric mill rhythm is shorter than in Cases 1-3 because the interburst and burst durations of  $LG$  are both shortened.

For a particular set of parameters, we obtained periodic solutions for Cases 1-4 and the region  $m$  for which the periods of Case 3 and Case 4 match. In Figure 4.9, the period of the gastric mill rhythm in Case 4 is plotted over the full range of possible  $m$  values for  $\tau_r = 7200$  and  $\tau_f = 5500$ . We see that for  $0 < m \leq 60$ , the period of the gastric mill rhythm for Case 3 is equal to that of Case 4. For  $470 < m \leq 740$ , the period of the gastric mill is equal to the period of  $AB$  activity. For  $60 < m \leq 470$ , there is a transition between having a period equal to that of Case 3 to the much shorter period of  $AB$  activity. Similarly, for  $740 < m \leq 1000$ , the period begins to increase from 1 sec up to the period found in Case 3. As stated in the previous section, for  $60 < m \leq 470$  and for  $740 < m \leq 1000$ , it may take several cycles of  $LG$  and  $Int1$  oscillations before the  $LG$  and  $Int1$  burst lengths duplicate themselves. In

these situations, the period is calculated as the time it takes to have two duplicate *LG* burst lengths divided by the number of cycles of *LG* oscillations occurring in that time.

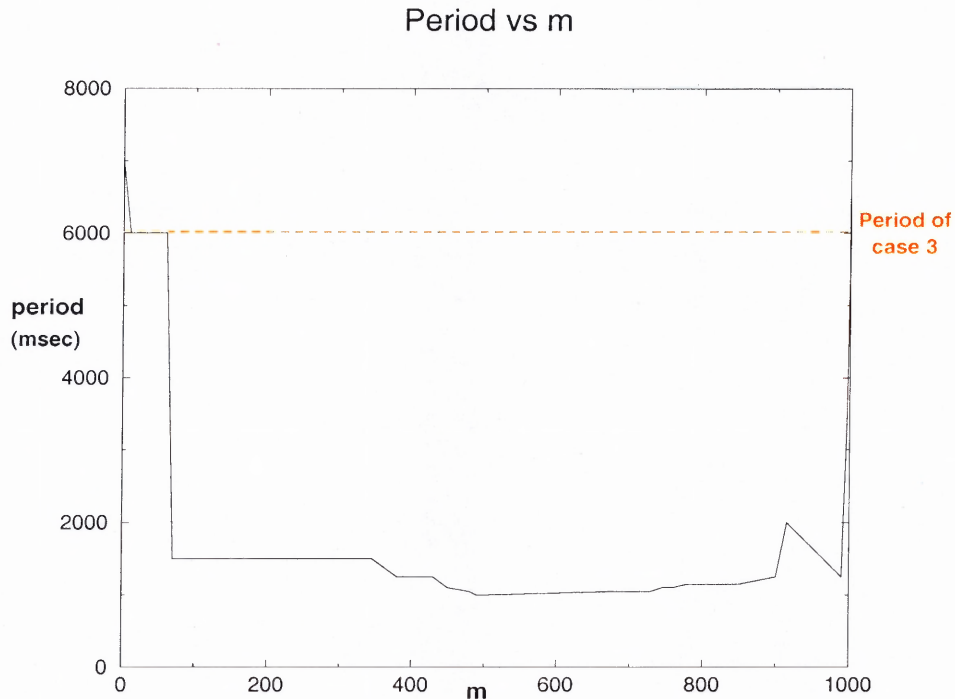


**Figure 4.9** The period of the gastric mill cycle is plotted for different delays,  $m$ , in Case 4. The period of Case 3 is marked by the dashed line. There is a small range of delays,  $0 < m \leq 60$ , for which the period of the gastric mill rhythm is equal for Cases 3 and 4.

In Figure 4.10, we see that our model accurately replicates the behavior of the gastric mill rhythm (see Figure 4.8) when  $0 < m \leq 60$ . Thus, the time mismatch between the pyloric and modulatory inputs to the gastric mill network is critical in establishing the correct frequency of the system. Upon relaxation of the conditions that  $s_{AB}(t)$  and  $s_2(t)$  jump between their minimum and maximum values instantaneously to the condition that the jump in  $s_2$  be fast compared with the rise and fall of  $s_1$ , the region  $m$  for which the period of Case 3 equals the period of Case 4 shifts to a neighborhood of approximately  $90 < m < 250$  depending upon the exact values of the parameters. In the biological system, the delay between *AB* activity and the inhibition from *AB* to *MCN1* is approximately 20 msec. The delay between *AB*

activity and the peak of *LG* disinhibition, however, can be from 200 to 400 ms [49]. This longer delay is believed to be a result of slow synaptic rise times [2, 49]. Thus, the range of delays found using the expanded, reduced model is consistent with the timing of the inputs in the biological circuit.

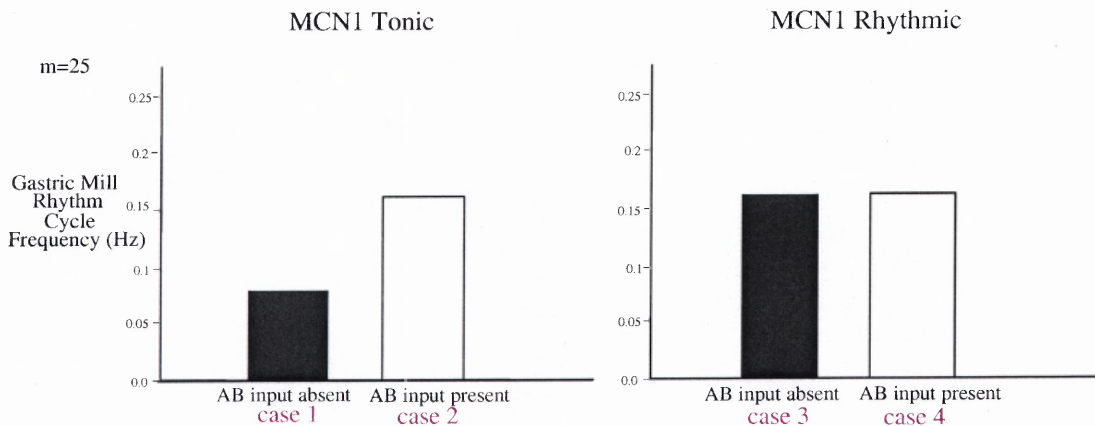


**Figure 4.10** Calculations of the gastric mill rhythm cycle frequency for Cases 1-4 using the expanded, reduced model with  $\tau_r = 7200msec$ ,  $\tau_f = 5500msec$ ,  $\tau_{rm} = 1msec$ ,  $\tau_{fm} = 1msec$ , period of  $s_{AB} = 1000msec$ ,  $m = 25msec$ , and  $g_{s1} = 6mS/cm^2$  in Cases 1 and 2 and  $g_{s1} = 7mS/cm^2$  in Cases 3 and 4.

While, the experimental work of Wood et al. [73] shows that the rhythmicity of *MCN1* serves as a second pathway by which the pyloric network regulates the activity of the gastric mill rhythm, these experiments also indicate that the direct inhibition from *AB* to *Int1* is required in order for *LG* and *Int1* to have the appropriate burst and interburst durations. The experimental calculations of the duty cycle of *LG* (defined as the amount of time *LG* is active divided by the period of *LG* activity) is different in each of the four cases. Thus, it is clear that having only one of the sources of the *AB* inputs is not sufficient to mimic the activity pattern when both of the *AB* inputs are present; see Figure 4.11.

In the expanded reduced model, the duty cycle of *LG* is different from Case 2 to Case 3 but is the same in Cases 3 and 4. The duty cycle of *LG* in Cases 3 and 4 match because the solution trajectory in Case 4 is defined to jump from  $s_R^{off}$  and  $s_L^{off}$  with the same timing as the solution trajectory in Case 3. If the condition that  $s_{AB}$

and  $s_2$  jump between their minimum and maximum values instantaneously is relaxed to being fast compared with the rate at which the excitation from  $MCN1$  to  $LG$  rises and decays, then the duty cycle of  $LG$  matches the experimental results because the solution trajectory in Case 4 spends slightly more time on the right branches of the nullclines than in Case 3 while still maintaining the same period as in Case 3; see Figure 4.11.

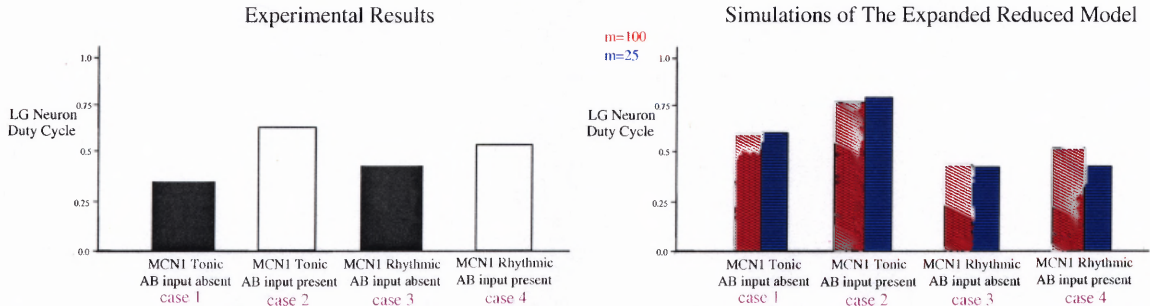


**Figure 4.11** Comparisons between the duty cycle of  $LG$  from the experimental work of Wood et al. [73] and from the expanded, reduced model. Shown in blue is the duty cycle with  $AB$  instantaneously inhibiting  $MCN1$  and  $LG$  and shown in red is  $AB$  not instantaneous but faster than the  $MCN1$  excitation.

Wood et al. [73] also determined that the latency locking between  $AB$  and rhythmic  $MCN1$  activity is essential to achieve the correct gastric mill activity pattern and coordination between the gastric mill and pyloric rhythms. Wood et al. compared the activity of the gastric mill rhythm when  $MCN1$  was pyloric timed as in the naturally occurring condition and when  $MCN1$  was free-running. In the latter case,  $MCN1$  activity was still rhythmic but not phase locked to  $AB$  activity. These experiments indicate that while the gastric mill frequency and  $LG$  duty cycle are unchanged by whether  $MCN1$  is pyloric timed or free-running, the timing of the gastric mill activity with regards to both  $MCN1$  and  $AB$  activity are affected; see Figures 4.12, 4.13, and 4.14.

This same behavior is not seen in the expanded, reduced model. Free-running  $MCN1$  activity is considered in the expanded, reduced model by fixing  $m$  and making the  $AB$  input to  $Int1$  (through  $s_{AB \rightarrow I}(t)$ ) and the  $AB$  input to  $MCN1$  (through

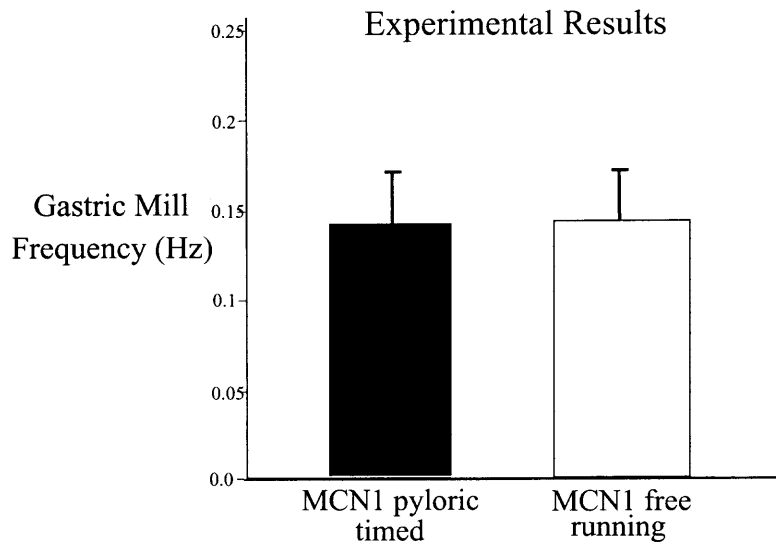


**Figure 4.12** Comparisons between the frequency of the gastric mill rhythm when *MCN1* activity is pyloric timed and when it is free-running with respect to *AB* activity. The experiments show that the frequency is not affected when *MCN1* is free-running [73].

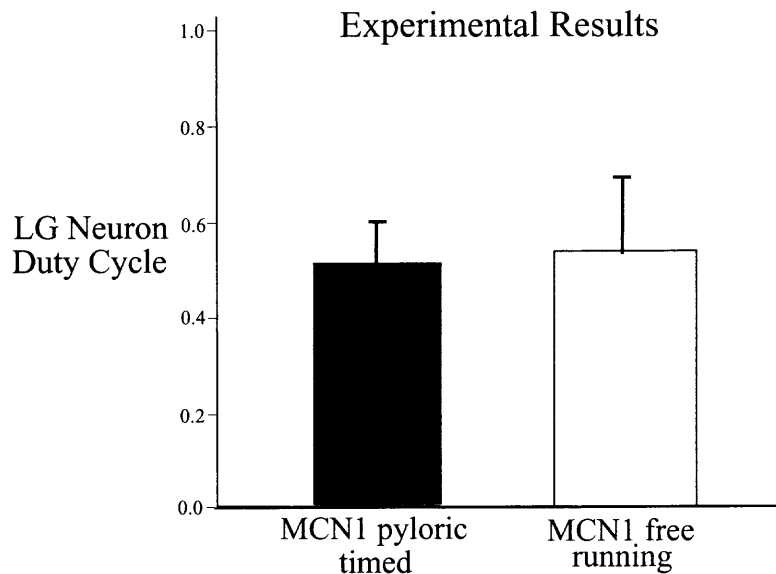


**Figure 4.13** Comparisons between the *LG* duty cycle when *MCN1* activity is pyloric timed and when it is free-running with respect to *AB* activity. The experiments show that the duty cycle of *LG* is not affected when *MCN1* is free-running [73].

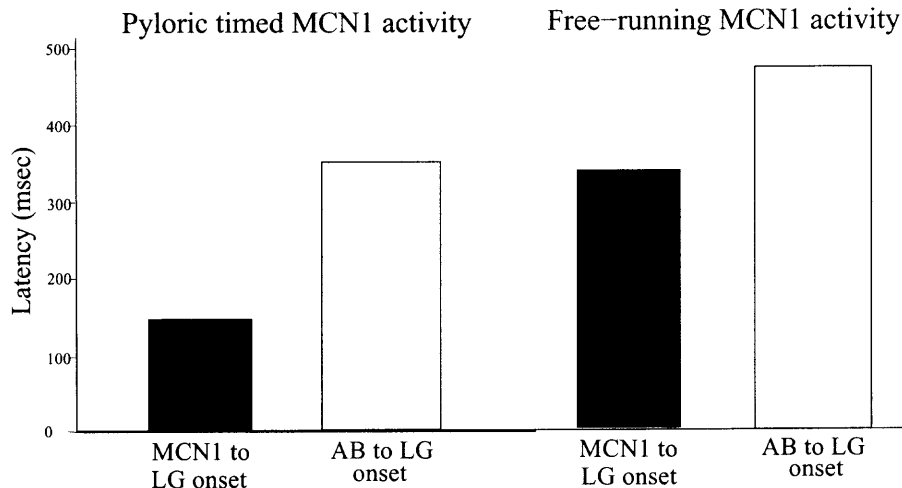


**Figure 4.14** The mean latency from the pyloric cycle preceding the *LG* burst to the onset of that *LG* burst increases from when *MCN1* activity is pyloric timed to when it is free-running [73].

$s_{AB \rightarrow M}(t)$  have slightly different frequencies. Thus, the *MCN1* input is rhythmic but not phase locked to *AB* activity. In this free-running case, the gastric mill rhythm and *LG* neuron duty cycle are not comparable with the rhythm and duty cycle obtained with the pyloric timed *MCN1* activity. In fact, with free-running *MCN1* rhythmicity, the gastric mill rhythm does not maintain repeating patterns of activity. Instead, the activity pattern continuously changes with oscillations of different frequencies; see Figure 4.15. This behavior occurs because the free-running activity of *MCN1* is essentially the same as running simulations of Case 4 with the delay  $m$  continuously changing so that the timing of the *MCN1* activity relative to *AB* is random. Thus, the period of the gastric mill rhythm is capable of taking on any value seen in Figure 4.9 throughout the duration of the simulation.

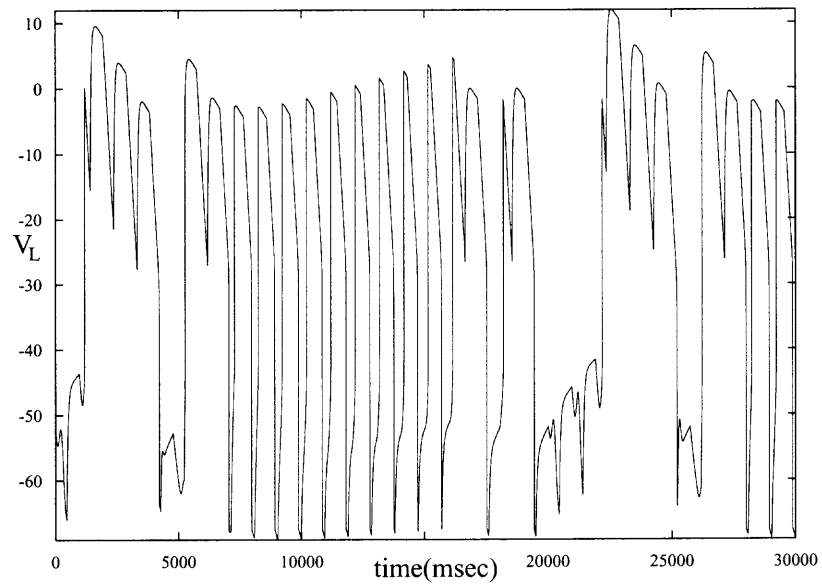


**Figure 4.15** Voltage trace of *LG* when the rhythmic *MCN1* activity is free-running with respect to the pyloric rhythm in the expanded, reduced model. The regularity of *LG* activity is not present when *MCN1* is free-running.

## CHAPTER 5

### A MORE BIOLOGICALLY ACCURATE REPRESENTATION OF THE REDUCED MODEL AND THE FULL MODEL

In this chapter, we expand upon the full model of Nadim et al. [49] to confirm that the results of our reduced model can be extended to the full model. Before returning to the full model, however, we consider the effect of making the excitatory synapse from *MCN1* to *LG* voltage dependent and restoring the electrical coupling between *MCN1* and *LG*. Restoring these two properties makes our reduced model a more realistic representation of the STG circuitry.

#### 5.1 Voltage Dependent *MCN1* to *LG* Synapse in The Expanded, Reduced Model

We now consider the effect of having voltage dependent coupling between *MCN1* and *LG* as opposed to a constant conductance synapse. Therefore, we return to Equation (3.22) with  $g_s(V_L) = \bar{g}_s s_\infty(V_L)$  where  $s_\infty(V_L)$  is a sigmoidal gating function going between 0 and 1 of the form

$$s_\infty(V) = \left( 1 + \exp \frac{v_k - V_k}{k} \right)^{-1}. \quad (5.1)$$

Due to this voltage dependency, the amount of excitation that *LG* receives from *MCN1* will depend upon the voltage of *LG* causing *LG* to receive less excitation when it, itself, is at a low voltage. Thus, when *LG* is in its interburst phase, the strength of the synapse will be weaker than in the work done in the previous chapter. When *LG* is in its burst phase, the strength of the synapse will increase to a value near to that in the previous chapter. As a consequence of the weaker conductance, in all of the Cases 1-4, the voltage dependency will increase the *LG* interburst duration because

$s$  will be required to grow to a larger value of  $s_{max}$  for the fixed point to be lost on the left branches of the nullclines. On the right branches of the nullclines, where  $LG$  is in its burst phase,  $s_{\infty}(V_L)$  is close to 1 and, therefore, the value of  $s_{min}$  will not be significantly different from when the conductance of the synapse is constant. However, since the value of  $s_{max}$  is larger, the time it takes for  $s$  to decrease to  $s_{min}$  is longer than when the conductance of the synapse is constant. In all Cases 1-4, this results in an increase in the period of the solutions.

Upon relaxing the conditions that  $s_2$  and  $s_{AB \rightarrow I}$  jump between their minimum and maximum values instantaneously, the voltage dependency also increases the range of  $m$  over which the period of Case 3 equals the period of Case 4. When  $s_2$  rises and decays exponentially,  $s_2$  moves continuously between its maximum and minimum values. In Manor et al. [40],  $s_{AB \rightarrow I}$  is treated as a half-sine function with duty-cycle equal to .5. Regardless of whether the conductance of the  $M CN1$  synapse to  $LG$  is constant or voltage dependent, the same condition must be satisfied for the period of Case 3 to equal the period of Case 4. This condition is that the fixed point on the left branches of the nullclines must be lost through  $s_L^{off}$ . That is,  $m$  must be chosen to live in a certain interval, say  $[M_1, M_2]$ , such that once  $s_1$  has grown large enough for  $s$  to reach  $s_L^{on}$  while  $s_{AB \rightarrow I} = 1$ , the  $V_L$  nullcline must be shifted far enough to the left by  $s_2$  when  $s_{AB \rightarrow M} = 1$  so that the saddle-node bifurcation does not occur at  $s_L^{on}$ . This situation persists until  $m$  becomes just larger than  $M_2$ . For  $M_2 < m < D_c P_{AB}$ , when  $s_{AB \rightarrow I}$  jumps to 1,  $s_{AB \rightarrow M}$  will already equal 1 so the  $V_L$  nullcline will already be to the left. However, before  $s_{AB \rightarrow I}$  returns to 0,  $s_{AB \rightarrow M}$  will return to 0. Consequently, the  $V_L$  nullcline will move to the right and the fixed point will not be lost through  $s_L^{on}$ .

When  $s_2$  rises and decays exponentially and  $m$  is slightly too large as described above, the loss of the fixed point through  $s_L^{on}$  when  $s_{\infty}(V_L) = 1$  often occurs while  $s_2$  is increasing towards 1 but has not yet reached its maximum value of 1. As a specific

example, for  $\tau_r = \tau_f = 4000$ ,  $\tau_{rm} = \tau_{fm} = 325$ , and conductance of the *MCN1* to *LG* synapse constant ( $s_\infty(V_L) = 1$ ), the periods of Cases 3 and Cases 4 are the same for  $80 \leq m \leq 275$ . Once  $m > 275$ , the saddle-node bifurcation occurs through  $s_L^{on}$  instead of  $s_L^{off}$ , thus, causing the period of Case 4 to be smaller than the period of Case 3.

Now let us consider the effect of the voltage dependent conductance on the position of the  $V_L$  nullcline and, therefore, the role it plays in altering the interval of  $m$  over which Case 3 equals Case 4. When *LG* is at a low voltage,  $s_\infty(V_L)$  is close to 0. Thus, on the left branches of the nullclines, when  $s_2$  decreases to its minimum, there is a much larger jump to the left of the  $V_L$  nullcline than when the conductance is constant. Furthermore, even as  $s_2$  increases back to 1, the  $V_L$  nullcline remains significantly far to the left until  $s_2$  gets very close to 1. Therefore, even as  $m$  increases to the range  $[M_2, D_c P_{AB}]$  where  $s_{AB \rightarrow M}$  jumps back to 0 (forcing  $s_2$  to increase back to 1) just before  $s_{AB \rightarrow I}$  returns to 0, the  $V_L$  nullcline will remain too far to the left (because it takes some amount of time for  $s_2$  to grow close enough to 1) for the saddle-node bifurcation to occur through  $s_L^{on}$ .

Hence, the fixed point cannot be lost through  $s_L^{on}$  while  $s_2$  is growing towards 1, as occurs when the conductance is constant. Furthermore, when  $s_{AB \rightarrow I}$  is a half-sine function, as in Manor et al. [40], the  $V_I$  nullcline spends less time in the lower position. Consequently, there is again a shorter range of time for  $s$  to reach  $s_L^{on}$  while the  $V_I$  nullcline is in the lower position. Accordingly, a larger interval of  $m$  will exist for the fixed point on the left branches of the nullclines to be lost from  $s_L^{off}$  as in Case 3 when the conductance is voltage dependent than when the conductance is constant. Returning to the example in the above paragraph, but now with the conductance of the *MCN1* to *LG* synapse voltage dependent, the interval of  $m$  for which the period of Case 3 equals the period of Case 4 extends to  $80 < m \leq 350$ . When  $s_2$  has instantaneous kinetics, there is no significant difference in the range of  $m$  between the

voltage dependent and non-voltage dependent cases because  $s_2$  is always equal either to 1 or 0, so the fixed point on the left branches cannot be lost while  $s_2$  is increasing towards 1.

## 5.2 Electrical Coupling Added to the Expanded, Reduced Model

An additional simplification in the model of Manor et al. [40] was the removal of voltage dependent electrical coupling between *MCN1* and *LG*. Coleman et al. [16] found that for *MCN1* in its tonic mode, while *LG* is in its burst phase and *LG* is pre-synaptically inhibiting *MCN1*, *LG* continues to receive excitatory post-synaptic potentials from *MCN1*. By blocking the chemical excitation from *MCN1*, they were able to deduce that these excitatory potentials were a result of electrical coupling between *MCN1* and *LG*. Furthermore, these excitatory post-synaptic potentials increased as the voltage of *LG* became more and more depolarized. This indicates that the electrical coupling is dependent upon the voltage of *LG* and that the inhibitory synapse from *LG* to *MCN1* does not inhibit *MCN1* activity. This supports the idea that the synapse simply cuts off the excitation from *MCN1* to *LG* by inhibiting the axon terminal of *MCN1*. Coleman et al. speculated that the role of the voltage dependent electrical coupling is to allow *LG* to receive excitation from *MCN1* when *LG* is in its burst phase while not opposing the inhibition from *Int1* that helps to control the *LG* interburst phase. This helps to sustain the *LG* burst when *MCN1* is tonic [16, 40]. The effect of the electrical coupling when *MCN1* is rhythmic remains unclear due to a lack of experimental data.

In this section, we determine the effect of the electrical coupling on the gastric mill rhythm using our expanded, reduced model. In this model, we add a voltage dependent electrical coupling term from *MCN1* to *LG*. Restoring the electrical coupling from *MCN1* to *LG*, the equation to describe the voltage of *LG* becomes:

$$\begin{aligned} \epsilon \frac{dV_L}{dt} = & -g_{leak,L}[V_L - E_{leak,L}] - g_{I \rightarrow L} n_{\infty I}(V_I)[V_L - E_{I \rightarrow L}] \\ & - g_s s(t)[V_L - E_{exc}] - g_{elec}(V_L)[V_L - V_M] \end{aligned} \quad (5.2)$$

where  $g_{elec}(V_L)$  measures the strength of the electrical coupling.  $g_{elec}(V_L)$  contains a maximal conductance term,  $\bar{g}_c$ , times a sigmoidal function of the form

$$g_{\infty}(V_L) = 1/(1 + \exp(k(V_L - V_k))), \quad (5.3)$$

where  $V_k$  is the half-activation voltage and  $k$  determines the slope at this point.  $g_{\infty}(V_L)$  lies between 0 and 1 so that the coupling is strong when  $V_L$  is at a high voltage and the coupling is weak when  $V_L$  is at a low voltage. The electrical coupling does not affect Equation (3.24) because this equation describes the voltage of *MCN1* in the soma and not at the axon where the electrical coupling is thought to actually exist. Therefore, in the expanded, reduced model, we only consider unidirectional electrical coupling from *MCN1* to *LG*. To check the effect of this simplification, we consider the electrical coupling to be bidirectional when we return to the full model of Nadim et al. [49]. We find that at a reasonable strength, the electrical coupling from *LG* to *MCN1* does not influence the *LG* burst or interburst durations because the conductance of the ionic currents in the *MCN1* axon overpower the effect of the electrical coupling.

In our reduced model, the electrical coupling causes the formerly 1-dimensional equation for the  $V_L$  nullcline to become 2-dimensional as it is now explicitly a function of both  $V_I$  and  $V_M$ . As stated in Chapter 3, the voltage of *MCN1* evolves on the fast time scale and lies between  $E_{leak,M}$  and  $V_M^*$  depending on the value of  $s_{AB \rightarrow M}$ . From (3.32), when  $s_{AB \rightarrow M}(t)$  decreases to 0,  $V_M$  increases to  $E_{leak,M} > V_{TH(M)}$ . When  $s_{AB \rightarrow M}(t)$  jumps to 1,  $V_M$  instantaneously jumps to  $V_M^*$  where

$$V_M^* = \frac{g_{leak,M} E_{leak,M} + \bar{g}_{AB \rightarrow M} E_{AB \rightarrow M}}{g_{leak,M} + \bar{g}_{AB \rightarrow M}}, \quad (5.4)$$

Thus, we can again consider the  $V_L$  nullcline in the  $V_L$  and  $V_I$  phase space where the position of the  $V_L$  nullcline shifts to the right and left due to  $s(t)$ . However, the position of the  $V_L$  nullcline is also affected by the value of  $V_M$ . When  $V_M = V_M^*$ , the  $V_L$  nullcline shifts farther to the left than in the absence of the electrical coupling and when  $V_M$  increases to  $E_{leak}$ , the nullcline shifts farther to the right than in the absence of the electrical coupling; see Figure 5.1.

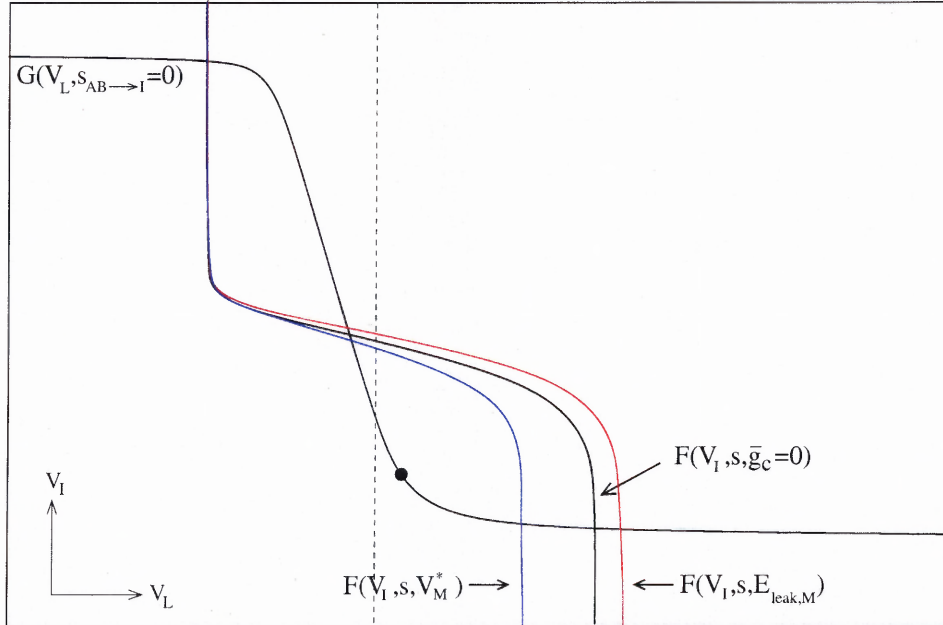


**Figure 5.1** The  $V_L$  and  $V_I$  nullclines are plotted in the absence ( $\bar{g}_c = 0$ , black  $V_L$  nullcline) and presence of electrical coupling ( $\bar{g}_c = .5$ ) between  $M CN1$  and  $LG$  for  $V_M = V_M^*$  (blue  $V_L$  nullcline) and  $V_M = E_{leak,M}$  (red  $V_L$  nullcline) for  $s(t) = .3$ . Note that only the right branch of the  $V_L$  nullcline is affected by the electrical coupling due to the voltage dependency of the coupling. The point at which the saddle-node bifurcation on the right branches occurs is marked by  $\bullet$ .

In Cases 1 and 2,  $s_{AB \rightarrow M} = 0$  and, therefore,  $V_M = E_{leak,M}$ . Thus, for a fixed value of  $s$ , the  $V_L$  nullcline is shifted farther to the right in the presence of the

electrical coupling than in its absence because  $E_{leak,M}$  is positive. Furthermore, due to the voltage dependency of the conductance, the shift of the right branch of the  $V_L$  nullcline to the right is much greater than the shift of the left branch. Consequently, when the electrical coupling is present and the trajectory lies at the stable fixed point on the right branches of the nullclines,  $s$  will need to decrease to a smaller value for the saddle-node bifurcation to occur through  $s_R^{on}$  or  $s_R^{off}$  than in the absence of the electrical coupling; see Figure 5.1. Therefore, the electrical coupling increases the  $LG$  burst duration. The electrical coupling does not greatly affect the  $LG$  interburst duration because on the left branches of the nullclines, the electrical coupling is weak. Thus, the electrical coupling requires  $s$  to grow to a slightly smaller value to reach either of the bifurcation points,  $s_L^{on}$  or  $s_L^{off}$ , than when the electric coupling is not present. However, on the left branches,  $s$  starts increasing from a smaller initial value than when the electrical coupling is not present. Thus, the interburst duration of  $LG$  is not significantly affected by the electrical coupling. Consequently, in Cases 1 and 2 the electrical coupling increases the gastric mill period by increasing the  $LG$  burst duration. The stronger the strength of the coupling, the larger the increase in the gastric mill period.

In Cases 3 and 4,  $V_M$  oscillates above and below  $V_{Th(M)}$ . Each time  $V_M$  increases to  $E_{leak,M}$ , the  $V_L$  nullcline shifts farther to the right than if there were no electrical coupling. However, each time  $V_M = V_M^*$ , the  $V_L$  nullcline shifts farther to the left than if there were no electrical coupling. Thus, on the right branches of the nullclines in Cases 3 and 4 when  $s_2$  jumps to  $s_{2min}$ ,  $V_M$  jumps to  $V_M^*$  and the  $V_L$  nullcline gets an extra push to the left depending on the strength of  $\bar{g}_c$ ; see Figure 5.2. Thus, as opposed to Cases 1 and 2, the electrical coupling helps to end the  $LG$  burst. On the left branches of the nullclines, the electrical coupling is again weak and does not cause a significant decrease in the  $LG$  interburst duration. Therefore, in Cases 3 and 4, there is no change in the gastric mill period when  $\bar{g}_c$  is small. There is a decrease

in the period of the gastric mill rhythm as  $\bar{g}_c$  increases because the electrical coupling helps to end the *LG* burst at an earlier time.

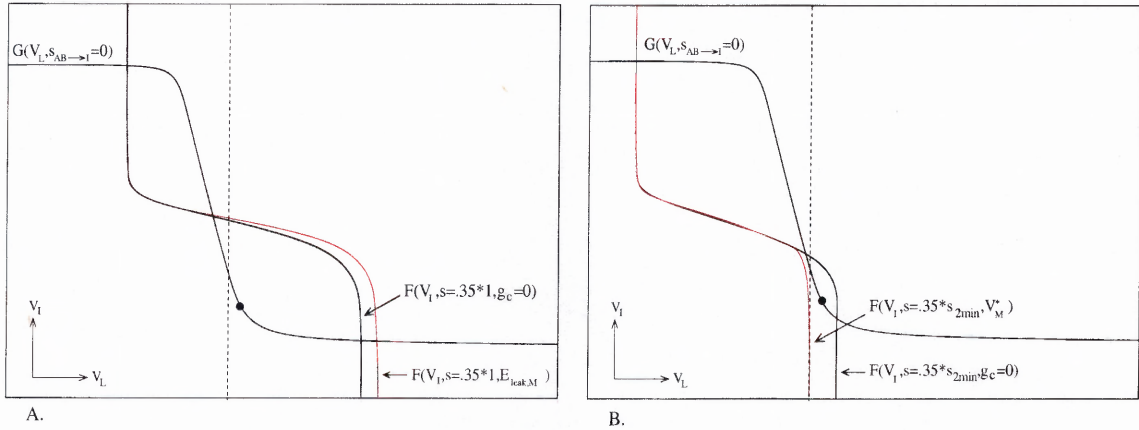


**Figure 5.2** The  $V_L$  and  $V_I$  nullclines are plotted in the absence of electrical coupling ( $\bar{g}_c = 0$ ) and presence of electrical coupling ( $\bar{g}_c = .5$ ) in Case 3. A.) When  $s_2 = 1$ ,  $V_M = E_{leak, M}$ . In this case, the  $V_L$  nullcline is shifted farther to the right in the presence of the electrical coupling than when  $\bar{g}_c = 0$ . B.) However, when  $s_2$  jumps to  $s_{2min}$ ,  $V_M$  jumps down to  $V_M^*$ . This pushes the  $V_L$  nullcline farther to the left in the presence of the electrical coupling than when  $\bar{g}_c = 0$ . Therefore, the burst duration of *LG* does not increase as a result of the electrical coupling.

Once  $\bar{g}_c$  becomes sufficiently large, the gastric mill rhythm becomes fixed to the activity of *MCN1*. Thus, when *MCN1* is above threshold, the voltage of *LG* goes above threshold and when *MCN1* is inhibited by *AB*, the voltage of *LG* also goes below threshold. Hence, the activity of *LG* becomes synchronized with the activity of *MCN1*. With the restriction that the electrical coupling only acts upon the voltage of *LG* when  $(V_M - V_L)$  is nonnegative, the burst duration of *LG* no longer decreases as  $\bar{g}_c$  increases. Instead, the electrical coupling has no effect on the ending of the *LG* burst duration and the end of the burst is determined solely by the dynamics of  $s(t)$ .

Furthermore, the electrical coupling between *MCN1* and *LG* does not affect the range of delays,  $m$  for which the period of Case 3 equals the period of Case 4 when the periodic solution satisfies Property B as in Theorem 2. This is because the jumps in  $V_M$  between  $V_M^*$  and  $E_{leak, M}$  occur with the same timing and direction as  $s_2$ , i.e. when  $V_M$  jumps to  $V_M^*$ ,  $s_2$  jumps to  $s_{2min}$  and when  $V_M$  increases to  $E_{leak, M}$ ,  $s_2$  jumps to 1.

On the right branches when  $s_2$  jumps from 1 to  $s_{2min}$ ,  $V_M$  also jumps from  $E_{leak,M}$  to  $V_M^*$ . Therefore, the  $V_L$  nullcline jumps from right to left due to the direct effect of  $V_M$  through the electrical coupling at the same time as the indirect effect of  $V_M$  through  $s_2$ . Thus, the presence of the electrical coupling does not interfere with the range of  $m$  over which the instantaneous loss of the fixed point on the right branches of the nullclines can occur. On the left branches of the nullclines, the electrical coupling is too weak for the  $V_L$  nullcline to be pushed through  $s_L^{on}$  while  $s_{AB \rightarrow I} = 1$  and  $V_M$  is increasing towards  $E_{leak,M}$  for  $m \in (0, T_C]$ . Therefore, there is again no interference with the range of  $m$  for which the fixed point is lost through  $s_L^{off}$  in Case 4. Although these results are reasonable for the reduced model, we will see in the following section that the reduced model cannot accurately capture the effect of the electrical coupling seen in the full model.

In our reduced model, we also considered the electrical coupling to be non-voltage dependent. This was done to determine the effect of the voltage dependency on the gastric mill rhythm. Again, the voltage dependency is such that the conductance of the electrical synapse increases as  $V_L$  increases. Thus for  $LG$  in its interburst phase, the conductance is weak and for  $LG$  in its burst phase, the conductance is almost equal to that of the non-voltage dependent conductance case. For a fixed value of  $\bar{g}_c$ , as would be expected, the  $LG$  burst duration was shorter when the electrical coupling was voltage dependent than when it was non-voltage dependent. This is because in the non-voltage dependent case, the conductance of the electrical coupling is  $\bar{g}_c * 1$  while the conductance in the voltage dependent case is  $\bar{g}_c * g_\infty(V_L)$  where  $0 < g_\infty(V_L) < 1$ . Therefore, the conductance is always stronger when the electrical coupling is non-voltage dependent and the voltage of  $LG$  is more depolarized by  $MCN1$ . We next checked the effect of the voltage dependency on the duty cycle of  $LG$ . This was done by increasing  $\bar{g}_c$  in the voltage dependent case until the  $LG$  burst durations were equal in both the voltage and non-voltage dependent cases. We found

that when  $\bar{g}_c$  was chosen so that the *LG* bursts matched, the interburst durations were not significantly different. Consequently, we concluded that the voltage dependency does not significantly alter the *LG* duty cycle.

### 5.3 Simulations of the Expanded, Full Model Using Network

The Hodgkin-Huxley-type full model of Nadim et al. [49] is a more accurate biophysical model of the gastric mill network than the expanded, reduced model. The equations for the membrane potentials of *LG*, *Int1*, and *MCN1* in the full model include terms for the ionic currents due to the movement of  $K^+$  and  $Na^+$  as well as leak currents. Each of these neurons is also modeled as being multicompartmental. Due to the simplicity of the expanded, reduced model, one may question the usefulness of the results. Thus, to confirm that the results on the control of frequency of the gastric mill rhythm are not an artifact of the simplicity of the model, we added the *AB* input to *MCN1* into the full model of Nadim et al. and ran simulations using Network for different delays in the timing of the *AB* inputs to *Int1* and *MCN1*. We refer to this expansion of the full model of Nadim et al. as the expanded, full model. In this expanded, full model, we also examined the effect of the voltage dependent electrical coupling on the gastric mill rhythm for *MCN1* rhythmic.

#### 5.3.1 Rhythmic *MCN1* Excitation in the Expanded, Full Model

In their experiments, Wood et al. [73] mimic the effect of the inhibition from *AB* to *MCN1* by stimulating *MCN1* between *AB* bursts. To replicate this experiment in the full model, we keep the voltage of *MCN1* below threshold each time *AB* fires an action potential. Thus, *MCN1* is rhythmic. In the expanded, full model, we found that the frequency in Case 3 is much higher than the frequency in Case 1. This is consistent with the findings of the reduced model and the experimental results of Wood et al.

Furthermore, the period of Case 3 is equal to the period of Case 4 only when there is a small delay from the time that  $AB$  inhibits  $MCN1$  to the time  $AB$  inhibits  $Int1$ ; see Figure 5.3. Figure 5.4 shows voltage traces of  $Int1$  and  $LG$  in Cases 3 and 4 for  $m$  near 0. For this small delay, the period of the gastric mill rhythm is equal in both Cases 3 and 4. Thus, the inhibition from  $AB$  to  $Int1$  does not affect the frequency of the gastric mill network. To obtain this result, we had to choose the parameters in our model to ensure that the rate of the rise of the excitation from  $MCN1$  to  $LG$  is faster than the rate of the decay of the excitation. This condition guarantees that the excitation to  $LG$  will build up despite the interruptions caused by the  $AB$  inhibition of  $MCN1$ . This condition is again consistent with the expanded, reduced model. In the expanded, reduced model,  $\tau_{rm}$  and  $\tau_{fm}$  are of the same order but the maximum value  $s_2$  can reach is 1 while the minimum value  $s_2$  can reach is  $s_{2min} > 0$ . Thus when  $LG$  is below threshold and  $MCN1$  is inhibited, the excitation to  $LG$  is not completely removed because  $s_2$  does not decay to 0. Additionally, while  $s_2 = s_{2min}$ ,  $s_1$  continues to increase. Therefore, when  $MCN1$  goes back above threshold, the excitation to  $LG$  is stronger than it was just before the excitation was removed due to  $AB$ .

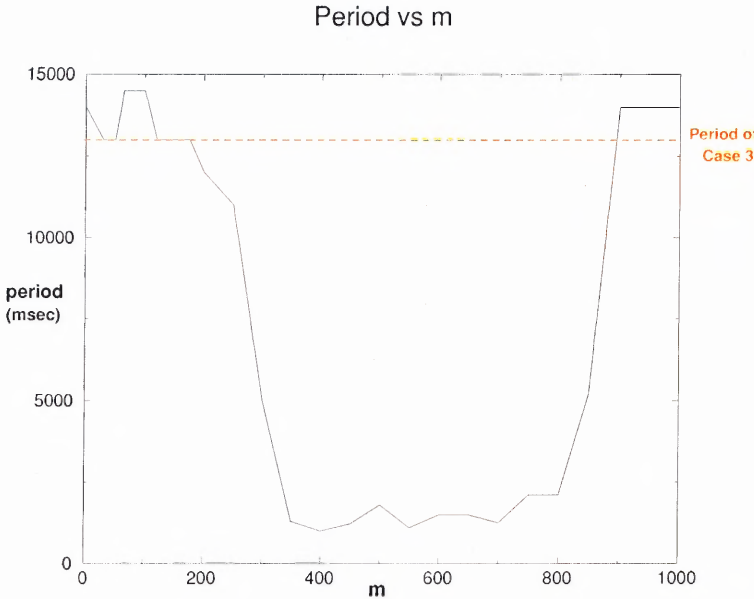


**Figure 5.3** The period of the gastric mill cycle calculated from the expanded, full model for different delays,  $m$ , in Case 4. The period of Case 3 is marked by the dashed line. There is a small range of delays,  $m$ , near 0 for which the period of the gastric mill rhythm is equal in Cases 3 and 4.

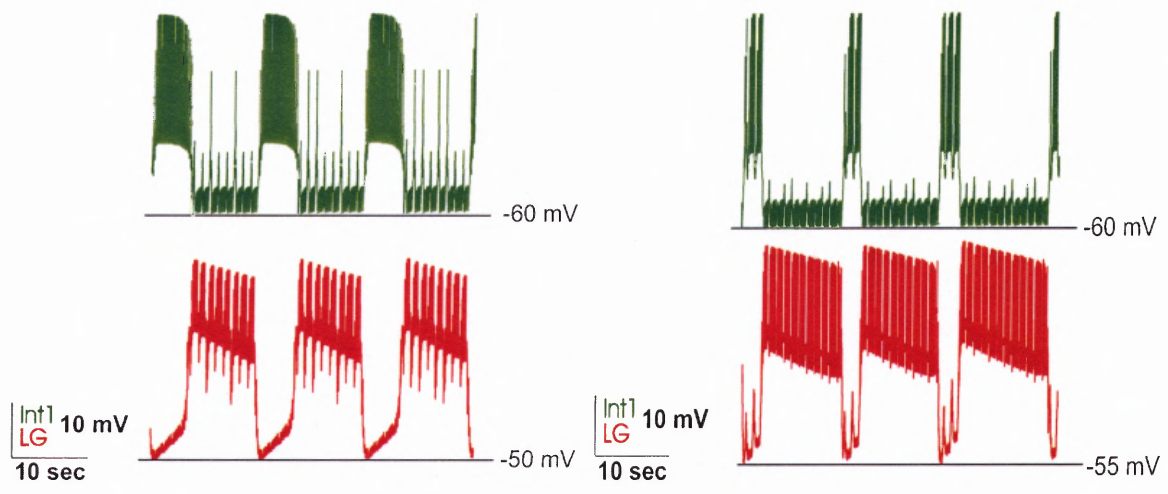


**Figure 5.4** Voltage traces of *LG* and *Int1* in Cases 3 (left) and 4 (right) for  $m = 180$ . For this delay, the period of the gastric mill rhythm is equal in Cases 3 and 4.

### 5.3.2 Electrical Coupling in the Expanded, Full Model

Based on experimental work, the full model of Nadim et al. [49] was constructed so that without electrical coupling, *MCN1* excitation alone could not evoke gastric mill rhythms. However, the full model of Nadim et al. [49] only considered the electrical coupling to be non-voltage dependent. Hence, we wanted to determine the effect of making the electrical coupling voltage dependent in our expanded, full model. As in the expanded, reduced model, we consider the conductance of the electrical coupling to be a maximal conductance,  $\bar{g}_c$ , times a sigmoidal function that increases from 0 to 1 as the voltage of *LG* increases. Similar to the expanded, reduced model, for a fixed value of  $\bar{g}_c$ , the *LG* burst duration was shorter when the electrical coupling was voltage dependent than when it was non-voltage dependent. We then checked the effect of the voltage dependency on the interburst duration of *LG* by increasing  $\bar{g}_c$  in the voltage dependent case until the *LG* burst durations were equal in both the voltage and non-voltage dependent cases. We again found that when  $\bar{g}_c$  was chosen so that the *LG* bursts matched, the interburst durations also matched. Thus, in the expanded, full model, the voltage dependency does not alter the *LG* duty cycle; see Figure 5.5.

To check if the influence of the electrical coupling in the full network is accurately described by the expanded, reduced model, we calculated the period of the gastric mill rhythm for increasing strengths of  $\bar{g}_c$ . In Cases 1 and 2, as  $\bar{g}_c$  increases (in both the non-voltage and voltage dependent situations), the burst duration of *LG* increases. This is consistent with the results of the reduced model. In Cases 3 and 4, as  $\bar{g}_c$  increases up to some  $\bar{g}_c^*$ , the burst duration of *LG* also increases. This, however, is not consistent with the results of the expanded, reduced model where the gastric mill period decreases as  $\bar{g}_c$  increases.

In Cases 3 and 4, when *LG* is in its burst phase and *MCN1* is inhibited by *AB* ( $V_M$  goes below threshold), The *LG* cell receives a hyperpolarizing current as a result

## Electrical Coupling in The Expanded Full Model

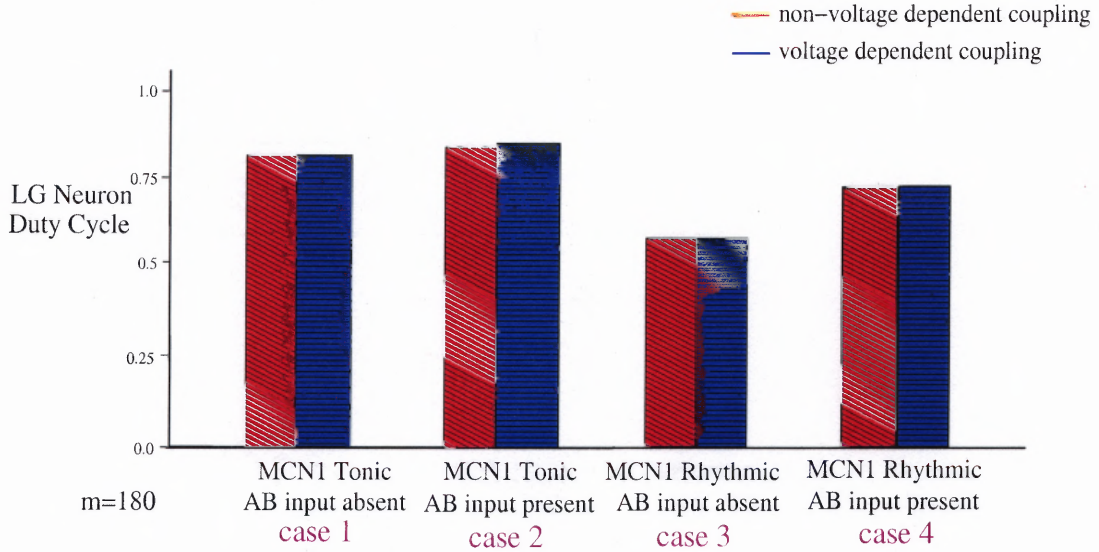


**Figure 5.5** The *LG* duty cycle is shown for Cases 1-4 when the conductance of the electrical coupling in the expanded, full model is constant ( $\bar{g}_c = 0.07$ ) shown in red and when the conductance is voltage dependent ( $\bar{g}_c = 0.0725$ ) shown in blue.

of the electrical coupling. In the expanded, full model, for  $0 < \bar{g}_c < \bar{g}_c^*$ , the burst duration does not end as a direct result of the hyperpolarizing current. Instead, the burst of *LG* ends when the excitation from *MCN1* has decayed sufficiently so that when *MCN1* switches from being inhibited by *AB* to being active, the depolarization due to the electrical coupling is not strong enough to sustain the *LG* burst.

Consider two different conductances of the electrical coupling,  $\bar{g}_{c1}$  and  $\bar{g}_{c2}$  with  $\bar{g}_{c1} > \bar{g}_{c2}$ . Each time *MCN1* is active,  $V_L$  will jump to a higher voltage for  $\bar{g}_c = \bar{g}_{c1}$  than for  $\bar{g}_c = \bar{g}_{c2}$ . Similarly, each time *MCN1* gets inhibited by *AB*,  $V_L$  will jump to a lower voltage for  $\bar{g}_c = \bar{g}_{c1}$  than for  $\bar{g}_c = \bar{g}_{c2}$ . However, the *LG* burst phase will not end as a result of the hyperpolarizing current due to the electrical coupling for either  $\bar{g}_{c1}$  or  $\bar{g}_{c2}$ . For  $\bar{g}_c = \bar{g}_{c2}$ , there is a region for which the excitation from *MCN1* has decayed sufficiently so that when *MCN1* changes from being inhibited by *AB* to being active, the electrical coupling is not strong enough to maintain the *LG* burst phase. In this same region for  $\bar{g}_c = \bar{g}_{c1}$ , once  $V_M$  becomes active again, the electrical coupling is strong enough so that  $V_L$  will become sufficiently depolarized to sustain

the *LG* burst. Thus, the *LG* burst duration and, consequently the gastric mill period increase as the strength of the electrical coupling increases; see Figure 5.6.

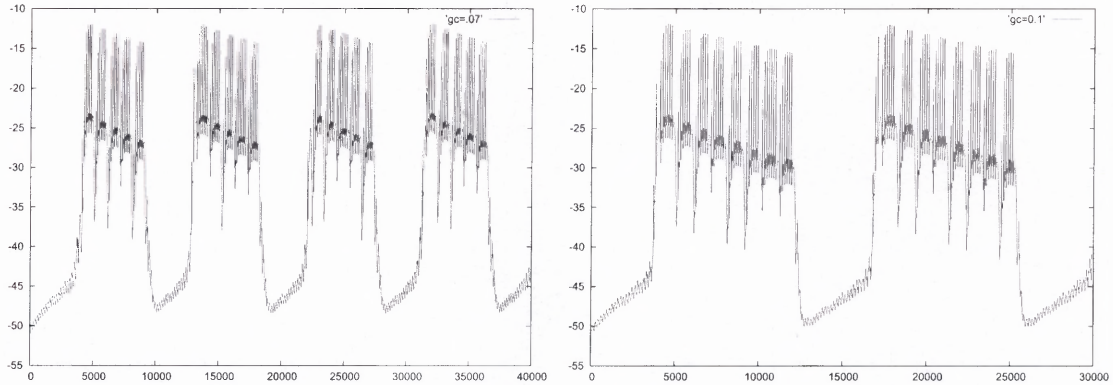


**Figure 5.6** Voltage traces of *LG* for two different strengths of  $\bar{g}_c$  obtained through simulations using Network. The *LG* burst duration and, consequently, the gastric mill period are shorter for  $\bar{g}_c = 0.07$  (left) than for  $\bar{g}_c = 0.1$  (right).

This behavior is not displayed by the expanded, reduced model. Thus, with regard to the electrical coupling, the simplicity of the expanded, reduced model places a limitation on the dynamics that it can capture. While our reduced model proves useful in understanding the behavior of the gastric mill rhythm in Cases 1 through 4, it cannot accurately describe all of the components of the full network. In the expanded, full model, as in the expanded, reduced model, once  $\bar{g}_c \geq \bar{g}_c^*$ , the activity of *LG* becomes locked to the *MCN1* activity. However,  $\bar{g}_c \geq \bar{g}_c^*$  is likely to be an unreasonably large value for the conductance in the biological circuit.

### 5.3.3 Comparison Between Simulations of the Expanded, Full Model and Experimental Results

In this section, simulations of the expanded, full model are compared to the experimental results of Wood et al. [73] to further validate the accuracy of the expanded, full model in modeling the gastric mill rhythm. Figure 5.7 shows the frequency of the gastric mill rhythm for *MCN1* tonic and rhythmic in the presence and absence of the *AB* input to *Int1*. As is seen experimentally (see Figure 4.8), when *MCN1* is tonic, the

*AB* input to *Int1* increases the frequency of the gastric mill rhythm. Additionally, the rhythmic *MCN1* activity increases the frequency of the gastric mill rhythm and when *MCN1* activity is rhythmic, the *AB* input to *Int1* does not further increase the gastric mill rhythm frequency as it does when *MCN1* is tonic. In our full model, the duty cycle of *LG* in Cases 1 and 2 are nearly identical. However, the duty cycle of Cases 2-4 are all different as in the experimental calculations; see Figure 5.8. Consequently, the expanded, full model shows that neither of the *AB* inputs alone is sufficient to mimic the activity pattern of having both of the *AB* inputs present. Free-running rhythmic activity of *MCN1* also produces the same result in the expanded, full model as in the expanded, reduced model. With free-running activity, the gastric mill rhythm does not maintain repeating patterns of activity but continuously changes with oscillations of different frequencies; see Figure 5.9. This occurs because, as in the expanded reduced model, the expanded full model is not tuned to be robust in properly integrating mixed inputs.

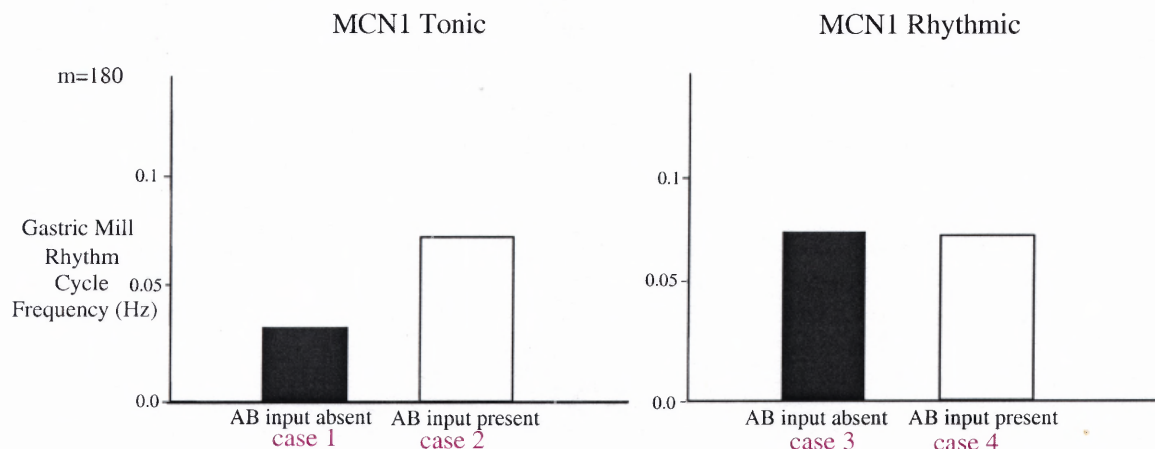


**Figure 5.7** The gastric mill rhythm cycle frequency for Cases 1-4 determined through simulations of the expanded, full model.

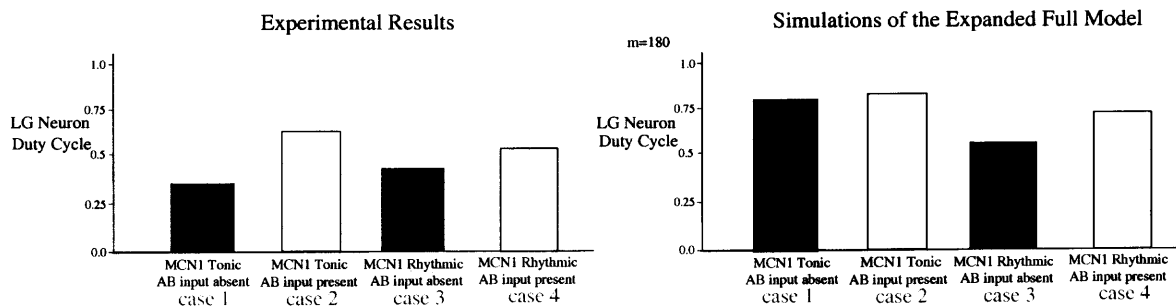


**Figure 5.8** The *LG* neuron duty cycle for Cases 1-4 determined through experiments and through simulations of the expanded, full model.

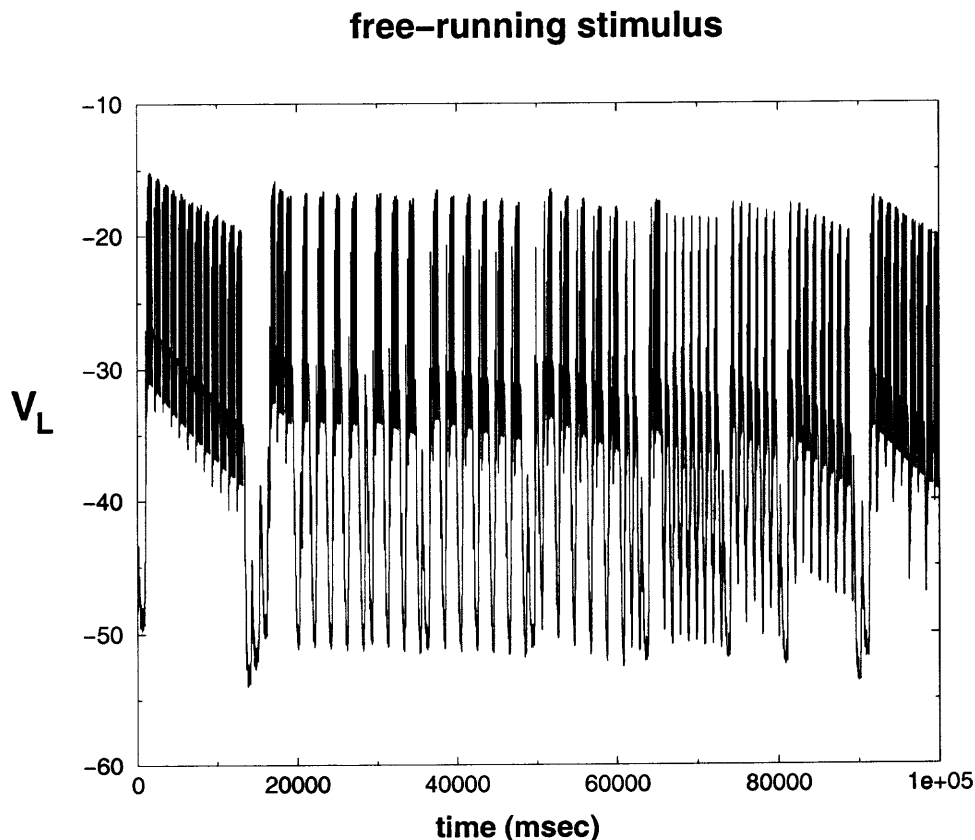


**Figure 5.9** Voltage trace of *LG* when the rhythmic *MCN1* activity is free-running with respect to the pyloric rhythm in the expanded, full model. The regularity of *LG* activity is altered when *MCN1* is free-running.

## CHAPTER 6

### CONCLUSION

#### 6.1 Summary of Results and Discussion

Many networks of interest involve an excitable system that requires external input to become active or to oscillate at the appropriate frequency [42, 68]. It has been observed that while tonic stimulation may often times be sufficient to elicit the network activity, the synaptic inputs driving these circuits are themselves rhythmic [10, 71]. An example of this is the pyloric network of the lobster stomatogastric nervous system which receives rhythmic excitatory input. The same effects of this rhythmic input, however, can be achieved through tonic firing of the input cells [46].

Furthermore, it has been noted in many cases that although one source of input is sufficient to produce oscillations in the target network, multiple inputs act together to generate and set the frequency of the network. Networks of this type are often seen in electrical circuits but can extend to other areas such as biological systems [15, 18, 19, 43]. The heartbeat of the leech, for example, is controlled by pairs of reciprocally inhibitory neurons. These oscillators receive inhibitory input from interneurons that act to coordinate the activity of the separate oscillators [14]. Einum et al. [21] also recently showed that reticulospinal neurons of the lamprey brain stem receive both excitatory and inhibitory rhythmic inputs from neurons in the spinal cord during locomotor activity.

In such networks, the frequency, strength, and timing of the oscillatory inputs are crucial for setting the appropriate frequency of the excitable system. If the strengths of each input are not weighted properly, the effect of one input may be overpowered by another. Similarly, the timing of the inputs will determine if they work together to magnify their effects or if they cancel one another. One can see how such factors are important in rhythmic movements where there is often the need for a

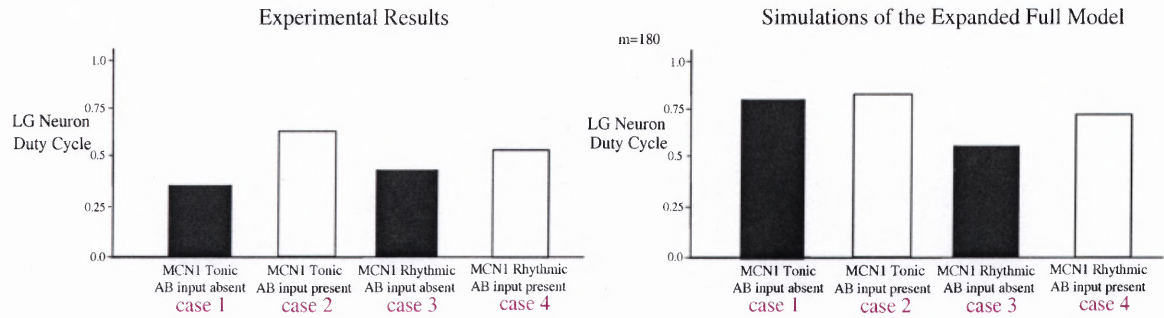


**Figure 5.8** The *LG* neuron duty cycle for Cases 1-4 determined through experiments and through simulations of the expanded, full model.

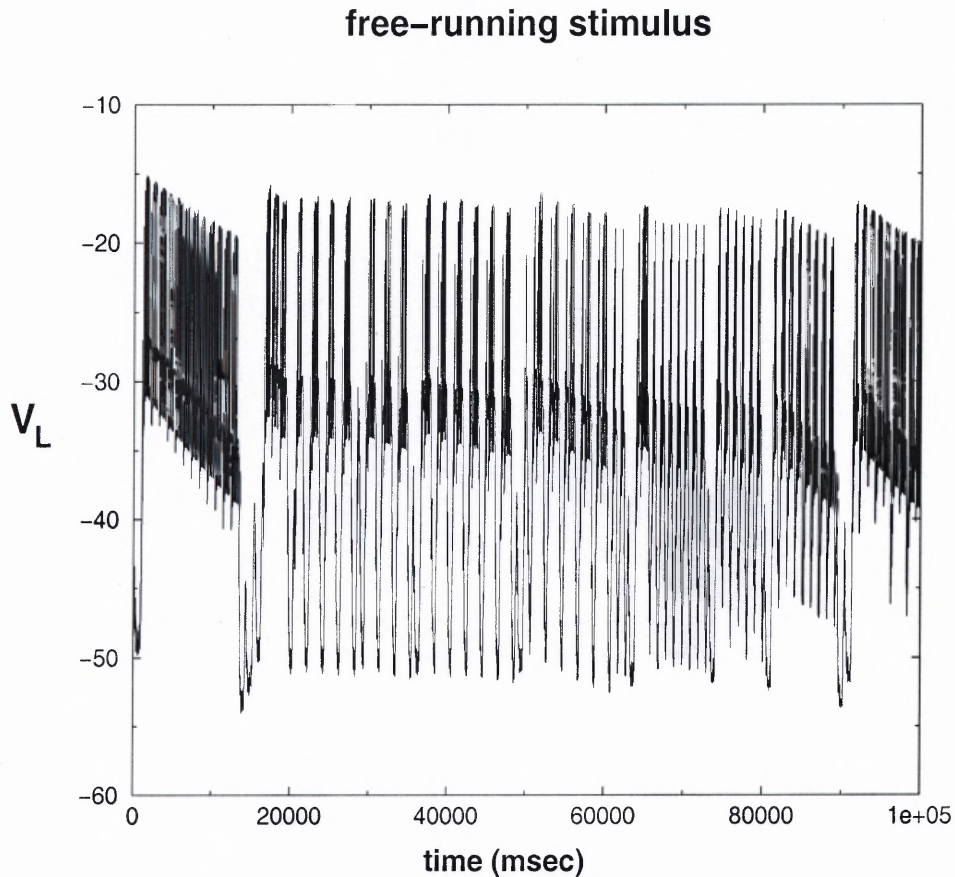


**Figure 5.9** Voltage trace of *LG* when the rhythmic *MCN1* activity is free-running with respect to the pyloric rhythm in the expanded, full model. The regularity of *LG* activity is altered when *MCN1* is free-running.

of the stable fixed point needed to jump from one branch of the nullcline where the neuron  $LG$  is active to the other branch where the neuron  $Int1$  is active to occur at an earlier time than when the input is tonic. Thus, although tonic stimulation of the gastric mill network can generate the gastric mill rhythm, the rhythmicity of the input speeds the frequency of the gastric mill rhythm as in seen by Wood et al. [73].

The effect of the synaptic input from  $AB$  to  $Int1$  in the case when  $MCN1$  is rhythmic, however, is not straight forward. The timing of the jump of the  $V_L$  and  $V_I$  nullclines in response to the  $AB$  input to  $Int1$  and to  $MCN1$  determines how the loss of the stable fixed point on either the left or right branches of the nullclines will be lost. This, in turn, determines the length of the  $LG$  and  $Int1$  interburst and burst durations. When the time mismatch is small, the presence of the  $AB$  input does not further increase the gastric mill rhythm frequency as is seen experimentally by Wood et al. [73]. This is because for no delay or a small delay between the two pyloric inputs, the position of the  $V_L$  nullcline in response to the  $AB$  inhibition of  $MCN1$  prevents the  $AB$  disinhibition of  $LG$  from ending the  $LG$  interburst. Thus, each time  $AB$  disinhibits  $LG$ , the excitation to  $LG$  from  $MCN1$  is removed. Therefore, when  $LG$  is in its interburst phase, it does not feel the effect of the  $AB$  input. Once  $LG$  does enter its burst phase due to the slow build up of  $MCN1$  excitation, the  $AB$  inhibition of  $Int1$  is relatively insignificant because  $Int1$  is already suppressed and, therefore, the  $LG$  burst ends as it does when the  $AB$  input to  $Int1$  is absent. Therefore, for a small time mismatch, the  $AB$  input to  $Int1$  does not alter the times at which  $LG$  enters and exits its burst and it is as if there is only one source of synaptic input to the gastric mill network.

For a larger time mismatch, however, this is not the case. When the time mismatch is chosen appropriately large so that when  $AB$  inhibits  $Int1$  the excitation to  $LG$  from  $MCN1$  is present, then there is a large increase in the firing frequency. The increase in frequency occurs because for this range of delays between the  $AB$

input to  $Int1$  and the  $AB$  input to  $MCN1$ , the position of the nullclines is such that  $LG$  does get disinhibited each time  $AB$  inhibits  $Int1$ . Thus, the interburst phase of  $LG$  is ended at an earlier time than when there is no  $AB$  input to  $Int1$ . This then allows the burst of  $LG$  to end at an earlier time. This is because to end the interburst of  $LG$ , the excitation did not have to build up very high and, as a result, it does not need to decay as long to end the burst of  $LG$ .

The phase-plane analysis also gives us some insight about the conditions that are necessary for the period of the gastric mill rhythm in Case 2 to equal that of Case 4. In order for the periodic solutions to be constructed in the same manner in both Cases 2 and 4, it is necessary for the delay  $m$  to be chosen such that the jump in  $s_2$  from 1 to  $s_{2min}$  does not prevent the loss of the fixed point on the left branches when the  $V_I$  nullcline jumps to its downward position. Thus,  $m$  must be in a neighborhood of  $D_c P_{AB}$ . However, on the right branches of the nullclines, the jump down of the  $V_I$  nullcline when  $AB$  inhibits  $Int1$  must be large enough to prevent the loss of the fixed point when  $s_2$  jumps from 1 to  $s_{2min}$ . For this to occur,  $m$  must be in a neighborhood of 0. Consequently, it will not be possible to find a range of  $m$  over which the periodic solutions are constructed in the same way in Case 2 and Case 4 because on the left branches of the nullclines  $m$  must be in a different range than on the right branches. In addition, the jump down in the right branch of the  $V_I$  nullcline when  $AB$  inhibits  $Int1$  is not significant and, therefore, will not be large enough to prevent the loss of the fixed point when  $AB$  inhibits  $MCN1$ . However, for  $m$  in a neighborhood of 0, the periods of Cases 2 and 4 can be made close because in Case 2 the  $LG$  interburst duration is shortened, allowing for a shorter period of the gastric mill oscillations. And for this same range of  $m$ , the  $LG$  burst duration in Case 4 is shortened, allowing for a shorter period of the gastric mill oscillations. For  $m$  outside of this range, both the  $LG$  burst and interburst durations are greatly shortened and, therefore, the period in Case 4 will be much shorter than the period in Case 2.

This mathematical analysis gives a possible biological mechanism by which the effects of the two simultaneous synaptic inputs can overlap to result in a frequency equivalent to that of having only one of the inputs present or can both work to influence the frequency. We confirmed these results ascertained through phase-plane analysis of the expanded, reduced model by running simulations of the expanded, full model in Network. In the full, biophysical model, the rhythmicity of *MCN1* was considered by suppressing *MCN1* each time *AB* went above threshold. When the rate of rise of the excitation from *MCN1* to *LG* is faster than the rate of decay of the excitation, the frequency of the gastric mill rhythm calculated from the expanded, full model yielded similar results to the expanded, reduced model. For a small delay from the time *AB* inhibits *MCN1* to the time *AB* inhibits *Int1*, the period of the gastric mill rhythm is nearly equal in Cases 3 and 4. As the delay increases, the period of the gastric mill rhythm becomes significantly shorter in Case 4 than in Case 3. This condition on the rates of rise and decay of *MCN1* excitation is necessary because it ensures that the excitation to *LG* builds between times at which *AB* inhibits *MCN1*, thus, allowing *LG* to enter its burst phase. If the rate of decay of excitation is too fast, each time *MCN1* gets inhibited by *AB*, the removal of excitation would drop the voltage of *LG* back to the hyperpolarized potential it was at during the previous *AB* active cycle.

This result shows that the pyloric input can affect the gastric mill frequency through two different mechanisms. The first is a direct input from *AB* to *Int1*. This input can shorten the *LG* interburst phase by periodically disinhibiting *LG*. The second is an indirect pathway through inhibition of *MCN1*. This pathway shortens the *LG* burst by helping to remove the excitation from *MCN1* to *LG* when *LG* is active. Our model shows that the timing between the pyloric and modulatory inputs to the gastric mill network when *MCN1* is rhythmic is key to obtaining the correct frequency and determining if the *AB* input to *Int1* will have an effect on the

*LG* interburst duration. Thus, the timing can be used as a tool to switch between different modes of firing frequency or to simply allow an additional pathway for *AB* to regulate the gastric mill frequency. This may serve as a means by which different chewing patterns are elicited. This reiterates the fact that knowing the circuitry is not enough to understand the complex behavior of a network. It is equally essential to know the fine details such as synaptic strengths, rates of rise and decay of the inputs, and the timing of these inputs with respect to one another in order to understand fully how they may act upon an entire network.

Furthermore, we analyzed the effect of making our reduced model more realistic by considering the conductance of the *MCN1* to *LG* synapse to be voltage dependent and the presence of voltage dependent electrical coupling from *MCN1* to *LG*. For the specific voltage dependency considered, we found that the voltage dependency increases the period of the gastric mill rhythm by increasing the *LG* interburst duration for both *MCN1* tonic and rhythmic. In addition, for *MCN1* rhythmic, the range of delays over which the direct *AB* input to *Int1* does not affect the period of the gastric mill rhythm increases. In the expanded, reduced model, the electrical coupling increases the periods of Cases 1 and 2 by increasing the *LG* burst duration. In Cases 3 and 4, the period does not increase due to the rhythmicity of *MCN1*. These results, however, do not extend to the expanded, full model and, therefore, reveal a limitation of the expanded, reduced model. In the expanded, full model, the voltage dependent electrical coupling increases the period of all four cases. In addition, the electrical coupling does not alter the qualitative behavior of the network oscillations regardless of whether the conductance is voltage dependent or constant.

The biological and mathematical reductions of the full, compartmental model of Nadim et al. [49] implemented by Manor et al. [40] and extended in this work have proven to be instrumental in understanding the frequency regulation of the gastric mill rhythm and intercircuit coordination with the pyloric network. Our reduced model

neglects all intrinsic currents and models the neurons in this network as having only leak currents. Despite the severity of these reductions, the expanded, reduced network is able to accurately model the gastric mill rhythm and its response to the slow, modulatory and fast, pyloric inputs. The expanded, reduced model, also, clarifies the relationship between the synaptic rise and decay times of the *AB* inhibition of *MCN1* in the expanded, full model necessary to obtain the experimentally observed behavior. Furthermore, because the expanded, reduced model of simply passive neurons is able to accurately reproduce the qualitative behavior of the expanded, full model, it is clear that the synaptic currents and their timing with respect to one another are the primary components responsible for the dynamics of the gastric mill rhythm. This is important because the ability to ignore the intrinsic dynamics of each of the neurons results in significantly simpler equations. This makes mathematical manipulation and analysis much more accessible. For example, in this network, we were able to reduce the study of our system to the study of a flow on a 1-dimensional map. This then allowed us to define a Poincare map to prove the existence and stability of periodic orbits which would have been otherwise impossible if working in higher dimensions.

## 6.2 Future Work

The investigation of how the gastric mill rhythm is determined and altered by external inputs does not end here. There are several extensions of this problem that are interesting and useful to consider in understanding the full control of network frequency. One such issue is to investigate the effect of the modulatory input from *MCN1* to *Int1* and to *AB* in the expanded, reduced model. *MCN1* activity has been shown to enhance the pyloric rhythm through an excitatory synapse to *AB*. As a consequence of the pre-synaptic inhibition from *LG* to *MCN1*, the synapse from *MCN1* to *AB* will allow the pyloric network to receive feedback from the gastric mill network. Thus, when *LG* is inactive, *MCN1* excites *AB*. However, when *LG* is active, the

pre-synaptic inhibition of *MCN1* by *LG* prevents *MCN1* from exciting *AB*. In this way, the gastric mill network can regulate the frequency of the pyloric rhythm [6, 56].

Understanding the role of the *MCN1* input to *AB* is a good means of determining how rhythmic oscillations of a pacemaker neuron can be influenced when it receives synaptic input. Additionally, it further explores the means by which two networks of different frequencies interact to control one rhythmic behavior (digestion, in this case). Since the gastric mill rhythm frequency is strongly affected by the pyloric rhythm, the effect of the modulatory input on the frequency of the pyloric rhythm will also translate into an effect on the gastric mill rhythm. The impact of the *MCN1* input to *Int1* and *AB* on the gastric mill frequency can be determined by considering the change in the position of nullclines in phase space as compared to when the input from *MCN1* to *Int1* and to *AB* is not present.

A second issue to consider is the impact of having *MCN1* input to the gastric mill network coactive with a second projection neuron, commissural projection neuron 2 (*CPN2*). There is electrical coupling between *CPN2* and *LG* and *Int1* sends an excitatory synapse to *CPN2*. When the *CPN2* input is present, the input from *AB* to *MCN1* is only active when *LG* is in its interburst. When *LG* is in its burst phase, *MCN1* activity is tonic [7, 53]. Thus, there clearly will be an effect on the frequency of the gastric mill rhythm when *CPN2* input is considered. The change in network frequency generated by coactivation of *MCN1* and *CPN2* compared with just *MCN1* activation is important in understanding how the intact animal can switch between different chewing patterns needed in eating and digesting different types of food.

The biological and mathematical reduction techniques applied in this analysis of the STG can be extended to numerous other models whose intrinsic and synaptic currents act on multiple time scales. The leech heartbeat, for example, is controlled by a network of reciprocally inhibitory neurons that are dependent upon both synaptic

and intrinsic currents. These currents are of both fast and slow dynamics and a biophysically detailed model of this network exists [50, 57]. Although this model was shown to accurately reproduce many of the behaviors of the real network, some properties have not yet been able to be reproduced and the significance of certain currents is not yet clearly understood. Therefore, deriving a reduced version of this model that is more amenable to mathematical investigation in terms of allowing for a reduction to lower dimensions and phase plane analysis is likely to reveal many of the underlying properties responsible for such things as the network oscillations and sensitivity to synaptic and intrinsic inputs.

Furthermore, the presence of electrical coupling throughout the STNS also illustrates the importance of doing more in depth analysis of model networks containing gap junctions. Recent studies have indicated the presence of electrical coupling in regions of the brain such as the hippocampus and brainstem. Electrical coupling is thought to play a significant role in mediating synchronous neuronal oscillations in such regions [9, 20]. The exact means by which electrical coupling affects a particular network, however, is an open question. Some work has been done in this area for strong electrical coupling [39, 45] and weak electrical coupling [38]. Bem et al. [8] recently showed that in a pair of identical, mutually inhibitory pacemaker neurons, the duty cycle of the cells is critical in determining the effect of the electrical coupling. In particular, with a short duty cycle, there is a range of intermediate electrical coupling strengths for which there is bistability between synchronous and anti-phase oscillations. It would be interesting, therefore, to consider a network of non-identical cells with an intermediate strength of electrical coupling in which alternative techniques to reduce the system to a study on lower dimensional manifolds would have to be developed and applied. This issue can be addressed in neurons modeled by Morris-Lecar type equations [48] in which phase plane analysis is possible.

## APPENDIX A

### PARAMETERS OF FULL MODEL

In this Appendix are the parameters for the ionic and synaptic currents used in the expanded, full model<sup>1</sup>.

**Table A.1** Parameters of The Ionic Currents for The Expanded Full Model

Cell	Current	Site	$\bar{g}_{ion}$	$E_{ion}$	State	k	$V_k$	l	$V_L$	$\tau_1$	$\tau_2$
<i>MCN1</i>	$Na^+$	axon	565.47	45	$m^3$	-0.25	-65			0	0
					h	0.24	-64	-0.24	-64	1	5
	$K^+$	axon	565.47	-80	$m^4$	-0.24	-54	0.24	-54	8	20
	Leak	axon terminals	8.976 3.59	-60 -70							
<i>LG</i>	$Na^+$	axon	10.996	45	$m^3$	-0.08	-21			0	0
					h	0.13	-33	-0.12	-62	0	5
	$K^+$	axon	12.566	-80	$m^4$	-0.045	-33	0.065	-5	4	100
		axon	0.0229	-60							
	Leak	soma neurite	0.314 0.0785	-40 -40							
<i>Int1</i>	$Na^+$	axon	10.995	45	$m^3$	-0.08	-26			0	5
					h	0.13	-38	-0.12	-67	0	5
	$K^+$	axon	18.85	-80	$m^4$	-0.045	-25	0.065	-30	4	150
		axon	0.628	-20	$m$	2	-65	2	-65	200	2500
		axon	0.023	-34							
	Leak	soma neurite	0.314 0.0785	-34 -34							

The State parameter determines if the ion channels are in the open state or closed state where  $m$  models the activation of the channel and  $h$  models the inactivation of the channel. The units of  $\bar{g}_{ion}$  are  $nS/cm^2$ . The units of  $E_{ion}$ ,  $V_k$ , and  $V_l$  are  $mV$ . The units of  $k$  and  $l$  are  $mV^{-1}$ . The units of  $\tau_1$  and  $\tau_2$  are  $msec$ .

<sup>1</sup>These parameters values were chosen based on private communication with Farzan Nadim and were adjusted to reproduce the biological output of the network as closely as possible.

**Table A.2** Parameters of The Synaptic Currents for The Expanded Full Model

Synapse	Pre-syn Site	Post-syn Site	$\bar{g}_{syn}$	$E_{syn}$	$\kappa$	$V_\kappa$	$\lambda$	$V_\lambda$	$\tau_3$	$\tau_4$
<i>MCN1</i> → <i>LG</i> (chemical)	axon terminal	neurite	2.2	45	-2	-68	2	68	8000	9000
<i>MCN1</i> → <i>LG</i>	axon	axon	0.07							
<i>MCN1</i> → <i>Int1</i> (electrical)	axon terminal	neurite	.0015	45	-1	-50			30	0
<i>Int1</i> → <i>LG</i>	soma	neurite	1.4	-80	-0.5	-49			100	0
<i>LG</i> → <i>Int1</i>	neurite	soma	0.13	-80	-0.5	-45			50	0
	axon	neurite	1.3	-80	-1	-25	1	-25	3	97
	axon	axon	1.3	-80	-1	-25	1	-25	3	97
<i>LG</i> → <i>MCN1</i>	neurite	axon terminal	150	-80	-2	-35	2	-35	5	270
<i>AB</i> → <i>Int1</i>		neurite	2.0	-70	-1	-55			80	0

The units of  $g_{syn}$  are  $nS/cm^2$ . The units of  $E_{syn}$ ,  $V_\kappa$ , and  $V_\lambda$  are  $mV$ . The units of  $\kappa$  and  $\lambda$  are  $mV^{-1}$ . The units of  $\tau_3$  and  $\tau_4$  are  $msec$ .

## APPENDIX B

### NON-DIMENSIONALIZATION OF THE SYSTEM OF EQUATIONS

In this Appendix, we begin with the dimensional, modeling set of equations and then non-dimensionalize this system. The non-dimensionalization reveals the presence of a small parameter,  $\epsilon$ , in some but not all of the equations. Thus, geometric singular perturbation theory can be used to reduce the system to a study on lower dimensional slow manifolds and the fast transitions between them.

The dimensional set of equations that model the gastric mill rhythm are

$$C \frac{dV_L}{dt} = -g_{leak,L1}[V_L - E_{leak,L1}] - \bar{g}_{I \rightarrow L1} n_{\infty 1}(V_I)[V_L - E_{I \rightarrow L1}] \quad (\text{B.1})$$

$$- g_{s1}(V_L)s(t)[V_L - E_{excl}] - g_{elec1}(V_L)[V_L - V_M],$$

$$C \frac{dV_I}{dt} = -g_{leak,I1}[V_I - E_{leak,I1}] - \bar{g}_{L \rightarrow I1} n_{\infty 1}(V_L)[V_I - E_{L \rightarrow I1}] \quad (\text{B.2})$$

$$- \bar{g}_{AB \rightarrow I1} s_{AB \rightarrow I}(t)[V_I - E_{AB \rightarrow I1}],$$

$$C \frac{dV_M}{dt} = -g_{leak,M1}[V_M - E_{leak,M1}] - \bar{g}_{AB \rightarrow M1} s_{AB \rightarrow M}(t)[V_M - E_{AB \rightarrow M1}], \quad (\text{B.3})$$

$$\frac{ds_1}{dt} = \begin{cases} [1 - s_1]/\tau_r & V_L \leq V_{T1}, \\ -s_1/\tau_f & V_L > V_{T1}, \end{cases} \quad (\text{B.4})$$

$$\frac{ds_2}{dt} = \begin{cases} [1 - s_2]/\tau_{rm} & V_M \geq V_{Th(M1)}, \\ [s_{2min} - s_2]/\tau_{fm} & V_M < V_{Th(M1)}, \end{cases} \quad (\text{B.5})$$

$$\frac{ds_{AB \rightarrow M}}{dt} = \begin{cases} [1 - s_{AB \rightarrow M}]/\tau_{M1} & V_{AB} \geq V_{Th(AB)}, \\ [-s_{AB \rightarrow M}]/\tau_{AB} & V_{AB} < V_{Th(AB)}, \end{cases} \quad (\text{B.6})$$

where

$$n_{\infty 1}(V_x) = \left(1 + \exp \frac{v_x - V_x}{k_x}\right)^{-1}. \quad (\text{B.7})$$

The units of  $V_L$ ,  $V_I$ ,  $V_M$ ,  $E_{ion}$ , and  $E_{syn}$  are  $mV$ . The units of  $g_{ion}$  and  $g_{syn}$  are  $mS/cm^2$ . The units of  $C$  are  $\mu F/cm^2$  and the units for  $t$ ,  $\tau_r$ ,  $\tau_f$ ,  $\tau_{rm}$ ,  $\tau_{fm}$ ,  $\tau_{M1}$ , and  $\tau_{AB}$  are  $msec$ .  $s_1$ ,  $s_2$  and  $s_{AB \rightarrow M}$  are dimensionless quantities. We note that  $\tau_{rm}$ ,  $\tau_{fm}$ , and  $\tau_{M1}$  are of the same order of magnitude. In addition,  $\tau_r$ ,  $\tau_f$ , and  $\tau_{AB}$  are of the same order of magnitude but are small compared with  $\tau_{rm}$ ,  $\tau_{fm}$ , and  $\tau_{M1}$ .

To non-dimensionalize the equations, we begin by letting  $\tau = CR_m$  and  $\hat{t} = t/\tau$  where  $R_m$  is the specific membrane resistance of the cell *MCN1* and  $\tau$  is the membrane time constant of the cell *MCN1* and is measured in  $msec$ . Therefore,  $\hat{t}$  is dimensionless. Note that  $\tau$  is the same order of magnitude as  $\tau_{rm}$ ,  $\tau_{fm}$ , and  $\tau_{M1}$ .

Next, we let  $\epsilon = \frac{\tau}{\tau_{AB}}$ . Thus,  $\epsilon$  is a dimensionless parameter and  $\epsilon \ll 1$  since  $\tau_{AB}$  is large compared with  $\tau$ . We also let  $\frac{1}{\tau_{r1}} = \frac{\tau_{AB}}{\tau_r}$ ,  $\frac{1}{\tau_{f1}} = \frac{\tau_{AB}}{\tau_f}$ ,  $\frac{1}{\tau_{r2}} = \frac{\tau}{\tau_{rm}}$ ,  $\frac{1}{\tau_{f2}} = \frac{\tau}{\tau_{fm}}$ , and  $\frac{1}{\tau_M} = \frac{\tau}{\tau_{M1}}$ . Note that  $\frac{1}{\tau_{r1}}$ ,  $\frac{1}{\tau_{f1}}$ ,  $\frac{1}{\tau_{r2}}$ ,  $\frac{1}{\tau_{f2}}$ , and  $\frac{1}{\tau_M}$  are all dimensionless and are order 1 quantities. We also define the dimensionless variables  $\hat{V}_L = V_L/E_{leak,M1}$ ,  $\hat{V}_I = V_I/E_{leak,M1}$ , and  $\hat{V}_M = V_M/E_{leak,M1}$  which are also order 1 quantities.

In the next step of the non-dimensionalization, we define the new parameters:

$$\frac{\tau g_{leak,L1}}{C} = g_{leak,L}, \quad \frac{\tau \bar{g}_{I \rightarrow L1}}{C} = \bar{g}_{I \rightarrow L}, \quad \frac{\tau g_{s1}}{C} = g_s, \quad \frac{\tau g_{leak,I1}}{C} = g_{leak,I}, \quad \frac{\tau \bar{g}_{L \rightarrow I1}}{C} = \bar{g}_{L \rightarrow I},$$

$\frac{\tau\bar{g}_{AB\rightarrow I1}}{C} = \bar{g}_{AB\rightarrow I}$ ,  $\frac{\tau\bar{g}_{leak,M1}}{C} = g_{leak,M}$ ,  $\frac{\tau\bar{g}_{AB\rightarrow M1}}{C} = \bar{g}_{AB\rightarrow M}$ . It is important to point out that  $\tau/C = R_m$  and, therefore,  $g_{leak,L}$ ,  $\bar{g}_{I\rightarrow L}$ ,  $g_s$ ,  $g_{leak,I}$ ,  $\bar{g}_{L\rightarrow I}$ ,  $\bar{g}_{AB\rightarrow I}$ ,  $g_{leak,M}$ ,  $\bar{g}_{AB\rightarrow M}$  are all dimensionless and are also order 1 in magnitude. Finally, we define the dimensionless reversal potentials in the system of equations. As a consequence of rescaling  $V_L$ ,  $V_I$ , and  $V_M$  by  $E_{leak,M1}$ , the natural rescaling of the reversal potentials emerges as:  $\frac{E_{leak,L1}}{E_{leak,M1}} = E_{leak,L}$ ,  $\frac{E_{I\rightarrow L1}}{E_{leak,M1}} = E_{I\rightarrow L}$ ,  $\frac{E_{exc1}}{E_{leak,M1}} = E_{exc}$ ,  $\frac{E_{leak,I1}}{E_{leak,M1}} = E_{leak,I}$ ,  $\frac{E_{L\rightarrow I1}}{E_{leak,M1}} = E_{L\rightarrow I}$ ,  $\frac{E_{AB\rightarrow I1}}{E_{leak,M1}} = E_{AB\rightarrow I}$ ,  $\frac{E_{leak,M1}}{E_{leak,M1}} = E_{leak,M} = 1$ ,  $\frac{E_{AB\rightarrow M1}}{E_{leak,M1}} = E_{AB\rightarrow M}$ ,  $V_{T1}/E_{leak,M1} = V_T$ , and  $V_{Th(M1)}/E_{leak,M1} = V_{Th(M)}$ . These dimensionless parameters are also order 1 quantities. For simplicity, we rename  $n_{\infty 1}(\hat{V}_x E_{leak,M1}) = n_{\infty}(\hat{V}_x)$  and  $g_{elec1}(\hat{V}_L E_{leak,M1}) = g_{elec}(\hat{V}_L)$ .

Thus, introducing these dimensionless quantities into (B.1)-(B.7) yields the non-dimensional set of equations

$$\begin{aligned} \frac{d\hat{V}_L}{d\hat{t}} = & -g_{leak,L}[\hat{V}_L - E_{leak,L}] - \bar{g}_{I\rightarrow L}n_{\infty}(\hat{V}_I)[\hat{V}_L - E_{I\rightarrow L}] \\ & -g_s(\hat{V}_L)s(\hat{t})[\hat{V}_L - E_{exc}] - g_{elec}(\hat{V}_L)[\hat{V}_L - \hat{V}_M], \end{aligned} \quad (\text{B.8})$$

$$\begin{aligned} \frac{d\hat{V}_I}{d\hat{t}} = & -g_{leak,I}[\hat{V}_I - E_{leak,I}] - \bar{g}_{L\rightarrow I}n_{\infty}(\hat{V}_L)[\hat{V}_I - E_{L\rightarrow I}] \\ & -\bar{g}_{AB\rightarrow I}s_{AB\rightarrow I}(\hat{t})[\hat{V}_I - E_{AB\rightarrow I}], \end{aligned} \quad (\text{B.9})$$

$$\frac{d\hat{V}_M}{d\hat{t}} = -g_{leak,M}[\hat{V}_M - E_{leak,M}] - \bar{g}_{AB\rightarrow M}s_{AB\rightarrow M}(\hat{t})[\hat{V}_M - E_{AB\rightarrow M}], \quad (\text{B.10})$$

$$\frac{ds_1}{d\hat{t}} = \begin{cases} \epsilon[1 - s_1]/\tau_{r1} & \hat{V}_L \leq V_T, \\ \epsilon[-s_1]/\tau_{f1} & \hat{V}_L > V_T, \end{cases} \quad (\text{B.11})$$

$$\frac{ds_2}{d\hat{t}} = \begin{cases} [1 - s_2]/\tau_{r2} & \hat{V}_M \geq V_{Th(M)}, \\ [s_{2min} - s_2]/\tau_{f2} & \hat{V}_M < V_{Th(M)}, \end{cases} \quad (\text{B.12})$$

$$\frac{ds_{AB \rightarrow M}}{d\hat{t}} = \begin{cases} [1 - s_{AB \rightarrow M}]/\tau_M & V_{AB} \geq V_{Th(AB)}, \\ \epsilon[-s_{AB \rightarrow M}]/\tau_{AB} & V_{AB} < V_{Th(AB)}. \end{cases} \quad (\text{B.13})$$

This set of equations describes the evolution of the system on the time scale of the membrane time constant,  $\tau$ . We can also consider the evolution of the system on a slower time scale by letting  $\xi = \epsilon\hat{t}$ . This gives us the equations in the form used in Chapters 3, 4, and 5.

## APPENDIX C

### CALCULATION OF THE STABILITY OF FIXED POINTS

In this Appendix, we determine the stability of the fixed points of Equations (3.22)-(3.23). To do this, we calculate the Jacobian matrix of the system (3.22)-(3.23) and then calculate the eigenvalues at a fixed point  $(V_L^*, V_I^*)$ . The Jacobian matrix of the system as a function of  $s$  is

$$\begin{pmatrix} \frac{\partial F(V_L, V_I, s)}{\partial V_L} & \frac{\partial F(V_L, V_I, s)}{\partial V_I} \\ \frac{\partial G(V_L, V_I)}{\partial V_L} & \frac{\partial G(V_L, V_I)}{\partial V_I} \end{pmatrix}$$

where  $F(V_L, V_I, s)$  and  $G(V_L, V_I)$  are the right-hand sides of Equations (3.22) and (3.23), respectively. The eigenvalues of this matrix can be determined by solving the following equation for  $\lambda$ :

$$\begin{aligned} \lambda^2 - \left( \frac{\partial F(V_L, V_I, s)}{\partial V_L} + \frac{\partial G(V_L, V_I)}{\partial V_I} \right) \lambda + \frac{\partial F(V_L, V_I, s)}{\partial V_L} \frac{\partial G(V_L, V_I)}{\partial V_I} \\ - \frac{\partial G(V_L, V_I)}{\partial V_L} \frac{\partial F(V_L, V_I, s)}{\partial V_I} = 0. \end{aligned} \quad (\text{C.1})$$

Using the quadratic formula, we find that

$$\lambda = \frac{(a + d) \pm \sqrt{(a + d)^2 - 4(ad - bc)}}{2} \quad (\text{C.2})$$

where

$$\begin{aligned} a &= \frac{\partial F(V_L, V_I, s)}{\partial V_L} \Big|_{(V_L^*, V_I^*)} = -g_{leak, L} - \bar{g}_{I \rightarrow L} n_\infty(V_I) - \bar{g}_s s \Big|_{(V_L^*, V_I^*)} \\ b &= \frac{\partial F(V_L, V_I, s)}{\partial V_I} \Big|_{(V_L^*, V_I^*)} = -g_{I \rightarrow L} (V_L - E_{I \rightarrow L}) \frac{dn_\infty(V_I)}{dV_I} \Big|_{(V_L^*, V_I^*)} \\ c &= \frac{\partial G(V_L, V_I)}{\partial V_L} \Big|_{(V_L^*, V_I^*)} = -g_{L \rightarrow I} (V_I - E_{L \rightarrow I}) \frac{dn_\infty(V_L)}{dV_L} \Big|_{(V_L^*, V_I^*)}, \end{aligned}$$

$$d = \frac{\partial G(V_L, V_I)}{\partial V_I} \Big|_{(V_L^*, V_I^*)} = -g_{leak, I} - \bar{g}_{L \rightarrow I} n_\infty(V_L) - \bar{g}_{AB \rightarrow I} s_{AB \rightarrow I} \Big|_{(V_L^*, V_I^*)}.$$

From Equations (3.22) and (3.23), it can easily be seen that  $a + d$  is always negative. Thus,  $\lambda$  will be negative and, therefore, the fixed point,  $(V_L^*, V_I^*)$ , will be stable if

$$ad - bc > 0. \quad (\text{C.3})$$

$\lambda$  will be positive and, therefore, the fixed point will be unstable if

$$ad - bc < 0. \quad (\text{C.4})$$

$a$  and  $d$  are both negative for all values of  $V_L^*$  and  $V_I^*$ . Therefore, the product  $ad$  is always positive. Furthermore,  $\bar{g}_{I \rightarrow L}(V_L - E_{I \rightarrow L})$ ,  $\bar{g}_{L \rightarrow I}(V_I - E_{L \rightarrow I})$ ,  $\frac{dn_\infty(V_I)}{dV_I}$ , and  $\frac{dn_\infty(V_L)}{dV_L}$  are all positive quantities. Consequently, for  $ad - bc$  to be negative,  $bc$  must be sufficiently small. The size of  $b$  and  $c$  depends upon the size of  $\frac{dn_\infty(V_I)}{dV_I}$  and  $\frac{dn_\infty(V_L)}{dV_L}$ , respectively.  $n_\infty(V)$  is a sigmoidal function that increases from 0 to 1 and has the exact form  $n_\infty(V) = (1 + \exp(v_x - V)/k_x)^{-1}$  and  $\frac{dn_\infty(V_x)}{dV_x} = \frac{1}{k_x} (1 + \exp(v_x - V))^{-2} \exp\frac{v_x - V_x}{k_x}$  where  $k_x$  determines the steepness of  $n_\infty(V_x)$  at  $v_x$ . Fixing  $k_x$  to be small,  $\frac{dn_\infty(V_x)}{dV_x}$  can be made arbitrarily small for  $V_x$  away from  $v_x$ . As a result, the product  $bc$  can be made arbitrarily small and, therefore,  $ad - bc > 0$ . Therefore, on the left and right branches of the nullclines, the fixed point is stable since  $V_x$  is away from  $v_x$ . Alternatively, when  $V_x \approx v_x$  and  $k_x$  is small,  $\frac{dn_\infty(V_x)}{dV_x}$  can be large. Thus  $bc$  can be large and, as a result, the quantity  $ad - bc$  can be negative. Therefore, on the middle branches of the nullclines, where  $V_x$  is close to  $v_x$ , the fixed point is unstable.

We can also numerically determine the sign of  $(ad - bc)$  for a particular fixed point by first choosing  $V_L^*$ . Once  $V_L^*$  is chosen, we can determine  $V_I^*$  by substituting  $V_L^*$  into Equation (3.44). We can then find  $s^*$ , the value of  $s$  when  $V_L$  and  $V_I$  are at

the fixed point  $(V_L^*, V_I^*)$ , by solving Equation (3.43) for  $s$ . We then plug  $s^*$ ,  $V_L^*$ , and  $V_I^*$  into  $(ad - bc)$  to determine if this quantity is positive or negative.

We find that on the left branches of the  $V_L$  and  $V_I$  nullclines both of the eigenvalues are negative. Therefore, the fixed point on the left branches of the nullclines is stable. Once  $s$  increases to the point where at the fixed point on the left branches, the nullclines intersect tangentially, the fixed point undergoes a saddle-node bifurcation. We denote this fixed point by  $(V_L^{snl}, V_I^{snl})$ . Similarly, when the fixed point occurs on the right branches of the nullclines, the eigenvalues are negative and, therefore, the fixed point is stable. Once  $s$  decreases to the point where at the fixed point on the right branches, the nullclines intersect tangentially, the fixed point again undergoes a saddle-node bifurcation. We denote this fixed point by  $(V_L^{snr}, V_I^{snr})$ . For values of  $V_L^*$  between  $V_L^{snl}$  and  $V_L^{snr}$ , one eigenvalue is positive and one eigenvalue is negative. Thus, the fixed point is an unstable saddle. We say that the fixed point lies on the middle branch of the  $V_L$  and  $V_I$  nullclines when  $V_L^*$  lies between  $V_L^{snl}$  and  $V_L^{snr}$ .

## APPENDIX D

### CALCULATION OF $S_L^{ON}$ , $S_L^{OFF}$ , $S_R^{ON}$ , AND $S_R^{OFF}$

This Appendix describes how to analytically calculate the values of  $s$  for which the saddle-node bifurcation on the left and right branches of the  $V_L$  and  $V_I$  nullclines occurs. This is done for the case when  $s_{AB \rightarrow I}(t) = 0$  and the case when  $s_{AB \rightarrow I}(t) = 1$ .

When the fixed point occurs at the point where the two nullclines intersect tangentially on the left branches for  $s_{AB \rightarrow I}(t) = 0$ ,  $s = s_L^{off}$ . Similarly,  $s = s_R^{off}$  when  $s_{AB \rightarrow I}(t) = 1$  and the fixed point occurs at the point where the two nullclines again intersect tangentially on the right branches. Thus, to calculate  $s_L^{off}$  and  $s_R^{off}$ , we use the equations for the  $V_L$  and  $V_I$  nullclines:

$$V_L = F(V_I, s) = \frac{g_{leak,L} E_{leak,L} + \bar{g}_{I \rightarrow L} n_\infty(V_I) E_{I \rightarrow L} + \bar{g}_s s E_{exc}}{g_{leak,L} + \bar{g}_{L \rightarrow I} n_\infty(V_I) + \bar{g}_s s} \quad (\text{D.1})$$

and

$$V_I = G(V_L, s_{AB \rightarrow I}) = \frac{g_{leak,I} E_{leak,I} + \bar{g}_{L \rightarrow I} n_\infty(V_L) E_{L \rightarrow I} + \bar{g}_{AB \rightarrow I} s_{AB \rightarrow I}(t) E_{AB \rightarrow I}}{g_{leak,I} + \bar{g}_{L \rightarrow I} n_\infty(V_L) + \bar{g}_{AB \rightarrow I} s_{AB \rightarrow I}(t)} \quad (\text{D.2})$$

We first rewrite (D.2) as

$$\begin{aligned} V_L &= -k_L l n \left[ -1 + \frac{\bar{g}_{L \rightarrow I} (V_I - E_{L \rightarrow I})}{-g_{leak,I} (V_I - E_{leak,I}) - \bar{g}_{AB \rightarrow I} s_{AB \rightarrow I}(t) (V_I - E_{AB \rightarrow I})} \right] + v_L \\ &\doteq \tilde{G}(V_I, s_{AB \rightarrow I}) \end{aligned} \quad (\text{D.3})$$

We then find the equation for the tangent point by calculating

$$\begin{aligned}
\frac{dF(V_I, s)}{dV_I} = & [(g_{leak,L} + \bar{g}_{L \rightarrow I} n_\infty(V_I) + \bar{g}_s s) (\bar{g}_{I \rightarrow L} E_{I \rightarrow L} \frac{dn_\infty(V_I)}{dV_I}) - \\
& (g_{leak,L} E_{leak,L} + \bar{g}_{I \rightarrow L} n_\infty(V_I) E_{I \rightarrow L} + \bar{g}_s s E_{exc}) (\bar{g}_{L \rightarrow I} \frac{dn_\infty(V_I)}{dV_I})] \\
& / (g_{leak,L} + \bar{g}_{L \rightarrow I} n_\infty(V_I) + \bar{g}_s s)^2
\end{aligned} \tag{D.4}$$

and

$$\begin{aligned}
\frac{d\tilde{G}(V_I, s_{AB \rightarrow I})}{dV_I} = & \\
= -k_L \left[ \frac{-g_{leak,I}(V_I - E_{leak,I}) - \bar{g}_{AB \rightarrow I} s_{AB \rightarrow I}(t)(V_I - E_{AB \rightarrow I})}{\bar{g}_{L \rightarrow I}(V_I - E_{I \rightarrow L}) + g_{leak,I}(V_I - E_{leak,I}) + \bar{g}_{AB \rightarrow I} s_{AB \rightarrow I}(t)(V_I - E_{AB \rightarrow I})} \right] \\
& [(-g_{leak,I}(V_I - E_{leak,I}) - \bar{g}_{AB \rightarrow I} s_{AB \rightarrow I}(t)(V_I - E_{AB \rightarrow I})) (\bar{g}_{L \rightarrow I} + g_{leak,I} + \\
& \bar{g}_{AB \rightarrow I} s_{AB \rightarrow I}(t)) - (\bar{g}_{L \rightarrow I}(V_I - E_{I \rightarrow L}) + g_{leak,I}(V_I - E_{leak,I}) + \\
& \bar{g}_{AB \rightarrow I} s_{AB \rightarrow I}(t)(V_I - E_{AB \rightarrow I})) (-g_{leak,I} - \bar{g}_{AB \rightarrow I} s_{AB \rightarrow I}(t))] / \\
& (-g_{leak,I}(V_I - E_{leak,I}) - \bar{g}_{AB \rightarrow I} s_{AB \rightarrow I}(t)(V_I - E_{AB \rightarrow I}))^2,
\end{aligned} \tag{D.5}$$

and then setting

$$\frac{dF(V_I, s)}{dV_I} = \frac{d\tilde{G}(V_I, s_{AB \rightarrow I})}{dV_I}. \tag{D.6}$$

From (D.6), we obtain a quadratic equation for  $s$

$$\begin{aligned}
\bar{g}_s^2 s^2 + s \left[ 2\bar{g}_s [g_{leak,L} + \bar{g}_{I \rightarrow L} n_\infty(V_I)] - \bar{g}_{I \rightarrow L} E_{I \rightarrow L} \frac{dn_\infty(V_I)}{dV_I} g_s \frac{dV_I}{d\tilde{G}} \right. \\
+ \left. \bar{g}_{I \rightarrow L} \frac{dn_\infty(V_I)}{dV_I} \bar{g}_s E_{exc} \frac{dV_I}{d\tilde{G}} \right] + [g_{leak,L} + \bar{g}_{I \rightarrow L} n_\infty(V_I)]^2 \\
- \frac{dV_I}{d\tilde{G}} \left[ g_{leak,L} \bar{g}_{I \rightarrow L} E_{I \rightarrow L} \frac{dn_\infty(V_I)}{dV_I} - \bar{g}_{I \rightarrow L} \frac{dn_\infty(V_I)}{dV_I} [g_{leak,L} E_{leak,L} \right. \\
+ \left. \bar{g}_{I \rightarrow L} n_\infty(V_I) E_{I \rightarrow L}] \right] = 0.
\end{aligned} \tag{D.7}$$

Next, we use the restriction that the tangency of the nullclines must occur at a fixed point. Therefore, we use the equations for the  $V_L$  and  $V_I$  nullclines to determine the fixed points for different values of  $s$ . We rewrite (D.1) as

$$s = (-g_{leak,L}(V_L - E_{leak,L}) - \bar{g}_{I \rightarrow L} n_\infty(V_I)(V_L - E_{I \rightarrow L})) / g_s(V_L)(V_L - E_{exc}). \quad (D.8)$$

We then plug (D.3) into (D.8) to obtain an equation for  $s = S(V_I)$ . We find that

$$\begin{aligned} s &= \\ &= (-g_{leak,L}(-k_L \ln \left[ -1 + \frac{\bar{g}_{L \rightarrow I}(V_I - E_{L \rightarrow I})}{-g_{leak,I}(V_I - E_{leak,I}) - \bar{g}_{AB \rightarrow I} s_{AB \rightarrow I}(t)(V_I - E_{AB \rightarrow I})} \right] \\ &+ v_L - E_{leak,L}) - \bar{g}_{I \rightarrow L} n_\infty(V_I) \\ &(-k_L \ln \left[ -1 + \frac{\bar{g}_{L \rightarrow I}(V_I - E_{L \rightarrow I})}{-g_{leak,I}(V_I - E_{leak,I}) - \bar{g}_{AB \rightarrow I} s_{AB \rightarrow I}(t)(V_I - E_{AB \rightarrow I})} \right] + v_L - E_{I \rightarrow L})) \\ &/ g_s(-k_L \ln \left[ -1 + \frac{\bar{g}_{L \rightarrow I}(V_I - E_{L \rightarrow I})}{-g_{leak,I}(V_I - E_{leak,I}) - \bar{g}_{AB \rightarrow I} s_{AB \rightarrow I}(t)(V_I - E_{AB \rightarrow I})} \right] + v_L) \quad (D.9) \\ &(-k_L \ln \left[ -1 + \frac{\bar{g}_{L \rightarrow I}(V_I - E_{L \rightarrow I})}{-g_{leak,I}(V_I - E_{leak,I}) - \bar{g}_{AB \rightarrow I} s_{AB \rightarrow I}(t)(V_I - E_{AB \rightarrow I})} \right] + v_L - E_{exc}) = \\ &= S(V_I) \end{aligned}$$

This equation says that for each value of  $V_I$ , there exists a unique value of  $s$  which will cause the nullclines to intersect. We then check to see if this value of  $s$  also satisfies the quadratic Equation (D.7). If it does, we have found a bifurcation point of the fast subsystem. There are two values of  $s$  which satisfy both of the Equations (D.7) and (D.9) above. The smaller value of  $s$  corresponds to  $s_L^{off}$ , the larger corresponds to  $s_R^{off}$ . To calculate  $s_L^{on}$  and  $s_R^{on}$ , we follow the same steps as above but with  $s_{AB \rightarrow I}(t) = 1$  in (D.2).

In Case 2, we assume that  $s_{max} = s_L^{on}$  and  $s_{min}$  is the average of  $s_R^{off}$  and  $s_R^{on}$ . In Case 3, we assume the maximum value that  $s$  takes is  $s_L^{off}$  while  $s_2 = 1$  which

implies that  $s_{max} = s_L^{off}$  and the minimum value  $s$  assumes is  $s_R^{off}$  when  $s_2 = s_{2min}$ . Therefore,  $s_{min}$  is  $\frac{s_R^{off}}{s_{2min}}$ . In Case 4, the values of  $s_{max}$  and  $s_{min}$  depend on  $m$ . For  $m$  near 0, for example,  $s_{max}$  and  $s_{min}$  are calculated as in Case 3.

These calculations are clearly complicated and time consuming. Therefore, to obtain the values of  $s_L^{off}$ ,  $s_L^{on}$ ,  $s_R^{off}$ , and  $s_R^{on}$  needed to calculate the gastric mill rhythm frequency in Table 4.2, a numerical algorithm written in Fortran was used to calculate the values of  $s$  satisfying both (D.7) and (D.9).

## REFERENCES

- [1] S. Aiken, F. Kuenzi, and N. Dale. Xenopus embryonic spinal neurons recorded in situ with patch-clamp electrodes - conditional oscillator after all? *European Journal of Neuroscience*, 18(2):333-343, 2003.
- [2] C. Ambrosio, A. Bose, and F. Nadim. The effect of modulatory neuronal input on gastric mill frequency. *Neurocomputing*, 65-66C:623-631, 2005.
- [3] C. Ambrosio, F. Nadim, and A. Bose. The effects of varying the timing of inputs on a conditional oscillator. *Submitted to SIAM Journal on Applied Dynamical Systems*.
- [4] T. Apostol. *Mathematical Analysis*. Addison-Wesley Publishing Company, Inc, Philippines, second edition, 1974.
- [5] M. Bartos, Y. Manor, F. Nadim, E. Marder, and M. Nusbaum. Coordination of fast and slow rhythmic neuronal circuits. *The Journal of Neuroscience*, 19(15):6650-6660, 1999.
- [6] M. Bartos and M. Nusbaum. Intercircuit control of motor pattern modulation by presynaptic inhibition. *The Journal of Neuroscience*, 17(7):2247-2256, 1997.
- [7] M. Beenhakker and M Nusbaum. Mechanosensory activation of a motor circuit by coactivation of two projection neurons. *The Journal of Neuroscience*, 24(30):6741-6750, 2004.
- [8] T. Bem and J. Rinzel. Short duty cycle destabilizes a half-center oscillator, but gap junctions can restabilize the anti-phase pattern. *Journal of Neurophysiology*, 91:693-703, 2004.
- [9] C. Bou-Flores and A. Berger. Gap junctions and inhibitory synapses modulate inspiratory motoneuron synchronization. *Journal of Neurophysiology*, 85:1543-1551, 2001.
- [10] M. Bourque and A. Kolta. Properties and interconnections of trigeminal interneurons of the lateral pontine reticular formation in the rat. *Journal of Neurophysiology*, 86(5):2583-2596, 2001.
- [11] W. Boyce and R. DiPrima. *Elementary Differential Equations and Boundary Value Problems*. John Wiley and Sons, New York, seventh edition, 2001.
- [12] R. Calabrese. Oscillations in motor pattern-generating networks. *Current Opinion Neurobiology*, 5:816-823, 1995.
- [13] R. Calabrese. Neural coordination: Taking the lead from a model. *Current Biology*, 9(18):R680-R683, 1999.

- [14] R. Calabrese, F. Nadim, and O. Olsen. Heartbeat control in the medicinal leech: A model system for understanding the origin, coordination, and modulation of rhythmic motor patterns. *Journal of Neurobiology*, 27(3):390-402, 1995.
- [15] A. Cohen, S. Rossignol, and S. Grillner. *Neural Control of Rhythmic Movements in Vertebrates*. Wiley, New York, 1988.
- [16] M. Coleman, P. Meyrand, and M. Nusbaum. A switch between two modes of synaptic transmission mediated by presynaptic inhibition. *Nature*, 378:502-505, 1995.
- [17] M. Coleman and M. Nusbaum. Functional consequences of compartmentalization of synaptic input. *The Journal of Neuroscience*, 14(11):6544-6552, 1994.
- [18] S. Coombes and G. Lord. Desynchronization of pulse-coupled integrate-and-fire neurons. *Physical Review E*, 55(3):2104-2107, 1997.
- [19] M. Corio, R. Palisses, and D. Viala. Origin of the central entrainment of respiration by locomotion facilitated by mk 801 in the decerebrate rabbit. *Experimental Brain Research*, 95:84-90, 1993.
- [20] A. Draguhn, R. Traub, D. Schmitz, and J. Jefferys. Electrical coupling underlies high-frequency oscillations in the hippocampus in vitro. *Nature*, 394:189-192, 1998.
- [21] J. Einum and J. Buchanan. Reticulospinal neurons receive direct spinobulbar inputs during locomotor activity in lamprey. *Journal of Neurophysiology*, 92(3):1384-1390, 2004.
- [22] B. Ermentrout. *Simulating, Analyzing, and Animating Dynamical Systems: A Guide to XPPAUT for Researchers and Students*. SIAM, 2002.
- [23] R. FitzHugh. Impulses and physiological states in theoretical models of nerve membrane. *Biophysical Journal*, 1:445-466, 1961.
- [24] T. Fukuda and T. Kosaka. Gap junctions linking the dendritic network of gabaergic interneurons in the hippocampus. *The Journal of Neuroscience*, 20(4):1519-1528, 2000.
- [25] R. Gauss and R. Seifert. Pacemaker oscillations in heart and brain: A key role for hyperpolarization-activated cation channels. *Chronobiology International*, 17(4):453-469, 2000.
- [26] J. Gibson, M. Beierlein, and Connors B. Two networks of electrically coupled inhibitory neurons in neocortex. *Nature*, 402:75-79, 1999.
- [27] C. Gray. Synchronous oscillations in neuronal systems: Mechanism and functions. *Journal of Computational Neuroscience*, 1:11-38, 1995.

- [28] H. Heinzel, J. Weimann, and E. Marder. The behavioral repertoire of the gastric mill in the crab, *cancer pagurus*: An in situ endoscopic and electrophysiological examination. *Journal of Neuroscience*, 13(4):1793-1803, 1993.
- [29] A. Hodgkin and A. Huxley. The components of membrane conductance in the giant axon of loligo. *Journal of Physiology*, 116:473-496, 1952.
- [30] A. Hodgkin and A. Huxley. Currents carried by sodium and potassium ions through the membrane of the giant axon of loligo. *Journal of Physiology*, 116:449-472, 1952.
- [31] A. Hodgkin and A. Huxley. The dual effect of membrane potential on sodium conductance in the giant axon of loligo. *Journal of Physiology*, 116:497-506, 1952.
- [32] A. Hodgkin and A. Huxley. A qualitative description of membrane current and its application to conduction and excitation in nerve. *Journal of Physiology*, 117:500-544, 1952.
- [33] S. Hooper and R. DiCaprio. Crustacean motor pattern generator networks. *Neurosignals*, 13:50-69, 2004.
- [34] S. Hooper, M. O'Neil, R. Wagner, J. Ewer, J. Golowasch, and E. Marder. The innervation of the pyloric region of the crab, *cancer borealis*: Homologous muscles in decapod species are differently innervated. *Journal of Comparative Physiology A*, 159:227-240, 1986.
- [35] D. Johnston and S. Wu. *Foundations of Cellular Neurophysiology*. MIT Press, Massachusetts, first edition, 1996.
- [36] E. Kandel, J. Schwartz, and T. Jessell. *Principles of Neural Science*. Appleton and Lange, Connecticut, third edition, 1991.
- [37] C. Koch. *Biophysics of Computation*. Oxford University Press, New York, first edition, 1999.
- [38] E. Kopell and B. Ermentrout. Chemical and electrical synapses perform complementary roles in the synchronization of interneuronal networks. *Proceedings of the National Academy of Sciences*, 101(43):15482-15487, 2004.
- [39] T. Lewis and J. Rinzel. Self-organized synchronous oscillations in a network of excitable cells coupled by gap junctions. *Network: Computation in Neural Systems*, 11:299-320, 2000.
- [40] Y. Manor, F. Nadim, S. Epstein, J. Ritt, E. Marder, and N. Kopell. Network oscillations generated by balancing graded asymmetric reciprocal inhibition in passive neurons. *The Journal of Neuroscience*, 19(7):2765-2779, 1999.

- [41] E. Marder. Non-mammalian models for studying neural development and function. *Nature*, 417:318-320, 2002.
- [42] E. Marder and D. Bucher. Central pattern generators and the control of rhythmic movements. *Current Biology*, 11:R986-996, 2001.
- [43] E. Marder and R. Calabrese. Principles of rhythmic motor pattern generation. *Physiological Reviews*, 76(3):687-717, 1996.
- [44] D. McFarland and J. Lund. An investigation of the coupling between respiration, mastication, and swallowing in the awake rabbit. *Journal of Neurophysiology*, 69(1):95-108, 1993.
- [45] G. Medvedev and J. Cisternas. Multimodal regimes in a compartmental model of the dopamine neuron. *Physica D*, 194(3-4):333-356, 2004.
- [46] J. Miller and A. Selverston. Mechanisms underlying pattern generation in lobster stomatogastric ganglion as determined by selective inactivation of identified neurons. iv. network properties of pyloric system. *Journal of Neurophysiology*, 48(6):1416-1432, 1982.
- [47] E. Mishchenko and N. Rozov. *Differential Equations with a Small Parameter and Relaxation Oscillations*. Plenum Press, New York, 1980.
- [48] C. Morris and H. Lecar. Voltage oscillations in the barnacle giant muscle fiber. *Biophysical Journal*, 35(1):193-213, 1981.
- [49] F. Nadim, Y. Manor, M. Nusbaum, and E. Marder. Frequency regulation of a slow rhythm by a fast periodic input. *The Journal of Neuroscience*, 18(13):5053-5067, 1998.
- [50] F. Nadim, O. Olsen, E. De Schutter, and R. Calabrese. Modeling the leech heartbeat elemental oscillator I. interactions of intrinsic and synaptic currents. *Journal of Computational Neuroscience*, 2:215-235, 1995.
- [51] J. Nagumo, S. Arimoto, and S. Yoshizawa. An active pulse transmission line simulating nerve axon. *Proceedings of The IRE*, 50:2061-2070, 1962.
- [52] J. Nicholls, A. Martin, B. Wallace, and P. Fuchs. *From Neuron to Brain*. Sinauer Associates, Massachusetts, fourth edition, 2001.
- [53] B. Norris, M. Coleman, and M. Nusbaum. Recruitment of a projection neuron determines gastric mill motor pattern selection in the stomatogastric nervous system of the crab, *cancer borealis*. *Journal of Neurophysiology*, 72(4):1451-1463, 1994.
- [54] M. Nusbaum. Regulating peptidergic modulation of rhythmically active neural circuits. *Brain, Behavior and Evolution*, 60:378-387, 2002.

- [55] M. Nusbaum and M. Beenhakker. A small-systems approach to motor pattern generation. *Nature*, 417:343-350, 2002.
- [56] M. Nusbaum, J. Weimann, J. Golowasch, and E. Marder. Presynaptic control of modulatory fibers by their neural network targets. *The Journal of Neuroscience*, 12(7):2706-2714, 1992.
- [57] O. Olsen, F. Nadim, and R. Calabrese. Modeling the leech heartbeat elemental oscillator II. exploring the parameter space. *Journal of Computational Neuroscience*, 2:237-257, 1995.
- [58] L. Perko. *Differential Equations and Dynamical Systems*. Springer-Verlag, New York, third edition, 2001.
- [59] J. Rash. Mixed synapses discovered and mapped throughout mammalian spinal cord. *Proceedings of The National Academy of Sciences USA*, 93:4235-4239, 1996.
- [60] R. Satterlie. Reciprocal inhibition and postinhibitory rebound produce reverberation in a locomotor pattern generator. *Science*, 229:402-404, 1985.
- [61] H. Schwan, editor. *Biological Engineering*. McGraw Hill, New York, 1969. Mathematical Models for Excitation and Propagation in Nerve: written by FitzHugh R.
- [62] A. Selverston and M. Moulins, editors. *The Crustacean Stomatogastric System*. Springer-Verlag, Berlin, 1987. Chapter 1: written by Claiborne, B. and Ayers, J.
- [63] A. Selverston and M. Moulins, editors. *The Crustacean Stomatogastric System*. Springer-Verlag, Berlin, 1987. Chapter 3: written by Mulloney B.
- [64] A. Selverston and M. Moulins, editors. *The Crustacean Stomatogastric System*. Springer-Verlag, Berlin, 1987. Chapter 5: written by Miller, J.
- [65] A. Selverston and M. Moulins, editors. *The Crustacean Stomatogastric System*. Springer-Verlag, Berlin, 1987. Chapter 9: written by Marder, E.
- [66] A. Sharp, M. O'Neil, L. Abbott, and E. Marder. Dynamic clamp: Artificial conductances in biological neurons. *Trends in Neuroscience*, 16:389-394, 1993.
- [67] P. Skiebe. Neuropeptides are ubiquitous chemical mediators: Using the stomatogastric nervous system as a model system. *The Journal of Experimental Biology*, 204:2035-2048, 2001.
- [68] P. Stein, S. Grillner, A. Selverston, and D. Stuart, editors. *Neurons, Networks, and Motor Behavior*. MIT Press, Massachusetts, 1997.
- [69] G. Taga, Y. Yamaguchi, and H. Shimizu. Self-organized control of bipedal locomotion by neural oscillators in unpredictable environment. *Biological Cybernetics*, 65:147-159, 1991.

- [70] J. Thuma, L. Morris, A. Weaver, and S. Hooper. Lobster (*panulirus interruptus*) pyloric muscles express the motor patterns of three neural networks, only one of which innervates the muscles. *The Journal of Neuroscience*, 23(26):8911-8920, 2003.
- [71] J. Weeks. Neuronal basis of leech swimming: Separation of swim initiation, pattern generation, and intersegmental coordination by selective lesions. *Journal of Neurophysiology*, 45(4):698-723, 1981.
- [72] J. Weimann, P. Meyrand, and E. Marder. Neurons that form multiple pattern generators: Identification and multiple activity patterns of gastric/pyloric neurons in the crab stomatogastric system. *Journal of Neurophysiology*, 65(1):111-122, 1991.
- [73] D. Wood, Y. Manor, F. Nadim, and M. Nusbaum. Intercircuit control via rhythmic regulation of projection neuron activity. *The Journal of Neuroscience*, 24(34):7455-7463, 2004.
- [74] D. Wood, W. Stein, and M. Nusbaum. Projection neurons with shared cotransmitters elicit different motor patterns from the same neural circuit. *The Journal of Neuroscience*, 20(23):8943-8953, 2000.